Preparation of colloidal chains and studies of their structure and dynamics

Thesis Submitted to AcSIR for the Award of the Degree of

DOCTOR OF PHILOSOPHY

In Physical Sciences

By

Bipul Biswas

Registration Number: 10PP14J26027

Under the guidance of

Dr. Guruswamy Kumaraswamy

Polymer Science and Engineering Division

CSIR-National Chemical Laboratory, Pune 411008

सीएसआयआर–राष्ट्रीय रासायनिक प्रयोगशाला
(वैज्ञानिक तथा औद्योगिक अनुसंधान परिषद)
डॉ. होमी भाभा मार्ग, पुणे – 411 008. भारत
CSIR-NATIONAL CHEMICAL LABORATORY
(Council of Scientific & Industrial Research)
Dr. Homi Bhabha Road, Pune - 411008. India

CERTIFICATE

This is to certify that the work incorporated in this Ph.D. thesis entitled "**Preparation of colloidal chains and studies of their structure and dynamics**" submitted by **Mr. Bipul Biswas** to Academy of Scientific and Innovative Research (AcSIR) in fulfilment of the requirements for the award of the Degree of **Doctor of Philosophy**, embodies original research work under my guidance. I further certify that this work has not been submitted to any other University or Institution in part or full for the award of any degree or diploma. Research material obtained from other sources has been duly acknowledged in the thesis. Any text, illustration, table etc., used in the thesis from other sources, have been duly cited and acknowledged.

It is also certified that this work is done by the student (Bipul Biswas), under my supervision, is plagiarism-free.

Student

Bipul Biswas

Supervisor

Dr. Guruswamy Kumaraswamy

☎ FAX WEBSITE
Communications Channels
NCL Level DID : 2590
NCL Board No. : +91-20-25902000
Four PRI Lines : +91-20-25902000
Director's Office : +91-20-25902601
COA's Office : +91-20-25902660
SPO's Office : +91 20 25902664
www.ncl-india.org

DECLARATION BY RESEARCH SCHOLAR

I hereby declare that the thesis entitled "**Preparation of colloidal chains and studies of their structure and dynamics**" submitted by me for the Degree of Doctor of Philosophy to Academy of Scientific & Innovative Research (AcSIR) is the record of work carried out by me at Polymer Science & Engineering Division (PSE), CSIR- National Chemical Laboratory, Pune-411008, India, under the guidance of Dr. Guruswamy Kumaraswamy. The work is original and has not formed the basis for the award of any degree, diploma, associateship and fellowship titles in this or any other university or other institutes of higher learning. I further declare that the materials obtained from resources have been duly acknowledged in the thesis.

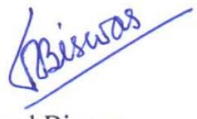

Bipul Biswas September-2019

Polymer Science & Engineering Division
CSIR- National Chemical Laboratory
Dr. Homi Bhabha Road, Pashan
Pune-411008
Maharashtra, India

DEDICATED TO MAA....

ACKNOWLEDGEMENT

It's a matter of pride and pleasure to present my research work as a Ph.D. thesis. I would like to express my gratitude and appreciation to all who helped me directly or indirectly to accomplish this ultimate academic goal.

First and foremost, I express my sincere gratitude to my supervisor Dr. Guruswamy Kumaraswamy for introducing me to this exciting research area (soft matter physics). Dr. Guruswamy is truly a knowledgeable and passionate scientist. His positive attitude toward science always inspires me. My earnest and deepest thanks to him for his rigorous training which helps me to become a researcher. He helped me to think out of the box, how to tackle a scientific problem, how to design an experiment and where to start the experiments. He helped me to analyse the data critically and how to write scientific papers and he trained me how to present the research work to general and specific audiences. I thank him for his support, help, encouragements and constructive criticisms during my Ph.D. work. His classes on small angle x-ray scattering, transport phenomenon and polymer physics were the foundation to build my basics in the field of my research. I would like to say that working under his guidance was a wonderful opportunity in my life.

I would like to sincerely thank my doctoral advisory committee members, Dr. Sayam Sen Gupta (now at IISER Kolkata), Dr. SK Bhat, Dr. BLV Prasad, Dr. PA Joy for their constant support and suggestions throughout my Ph.D.

I express my special thanks to Dr. Shankar Ghosh (TIFR- Mumbai) who is the 1st person, who helped me to design my experimental set-up and helped me to understand why I am doing all these experiments. I thank him for allowing me to work in his enriched lab for a month. I would like to thank Prof. Shalini Gupta (IIT-Delhi) for allowing me to spend a week in her lab and for scientific discussion with her. I extend my sincere thanks to Prof. Sanat Kumar (Columbia University, New York), it was a wonderful month for me there in New York, I learnt many things from his lab.

My thesis work would have been incomplete without the help of our collaborators. I sincerely thank to all our collaborators, Prof. Ronojoy Adhikari (The Institute of Mathematical Sciences-Chennai), Prof. PB Sunil Kumar (IIT-Madras), Prof. Apratim Chatterji (IISER Pune) and Prof.

Sanat Kumar (Columbia University, New York). I would also like to thank Dr. Chandan Kumar Choudhury, Dr. Raj Kumar Manna, Dr. Abhrajit Laskar and Dr. Mayank Misra and KP Fayis for the collaborative work. I also acknowledge Kamdi and KC for helping me to write Matlab code.

I acknowledge DST-INSPIRE for the fellowship to pursue Ph.D. in NCL and Academy of Scientific and Innovative Research (AcSIR) for allowing me to present my work in the form of a thesis. I would like to acknowledge IUSSTF for funding me to travel the US for collaborative work at Columbia University, New York, and a kick-off meeting held in Los Angeles.

I like to express my warm thanks to all my lab mates (Soumyajyoti, Manoj, Karthika, Sudhakar, Aakash, Saurabh, Anees, Subrajeet, Aniket, Kamdi) roommates (Ujjwal Nandi and Manoj Nandi), juniors, friends, and seniors in NCL. I also want to thank Shuklaji for his help. My association with all of them has made my stay on this campus pleasant. I also like to thank to my friend with whom I spent hours to discuss some important or silly things over the phone, the conversation made me joyful.

I express my respect and gratitude to all my teachers who have played an important role in my life. Special thanks to my school teacher Arun Kumar Dubey for inspiring me to do science for the betterment of society.

Finally, I would like to pay my deepest respect and gratitude to my parents for their love, support and sacrifice. I deeply acknowledge my elder brother (Dada), sister in law (Boudi) and sister (Didi) for their constant support and their selfless love. Last but not least, I want to express my respect and thanks to uncle (Kaka), Dinesh Roy who single-handedly solved all my problems. I deeply acknowledge him for his support and love.

Bipul Biswas
September-2019

TABLE OF CONTENTS

LIST OF FIGURES

LIST OF TABLES

ABSTRACT OF THE THESIS

Micron sized colloidal particles are Brownian, and can be conveniently visualized using optical microscopy. This thesis focuses on the preparation of colloidal assemblies comprising micron-sized colloidal particles linked through flexible linkers. Specifically, colloids linked in a linear fashion to form string-like objects are investigated.

In the first part of the thesis, we investigate ice templating of aqueous colloidal dispersions as a route to the preparation of colloidal assemblies. Highly dilute dispersions of polymer coated colloids are ice templated by freezing either isotropically or in a directional manner, and the polymeric shell is cross-linked to form assemblies. The dispersions are at concentrations that are far below that required to form percolated monoliths. There are three different types of assembled structures that form during ice templating: linear chains, two particle-wide tapes and extended sheets. We observe that, with increase in particle concentration from about ~10^6 to ~10^8 particles/ml, there is a transition from isolated single particles to increasingly larger clusters. In this concentration range, most of the colloidal clusters are linear or sheet like particle aggregates. Remarkably, the fractional probability for formation of a cluster of n particles, P_n ($n > 2$, up to n ~ 30 particles) scales as n^{-2}, independent of particle concentration for isotropic ice templating (over a 100-fold variation in concentration). Results from our experiments compare well with kinetic simulations performed by our collaborator. These simulations do not consider hydrodynamics or, instabilities at the growing ice front due to particle concentration gradients. Thus, clustering of colloidal particles by ice templating dilute dispersions appears to be governed only by particle exclusion by the growing ice crystals that leads to their accumulation at ice crystal boundaries.

In contrast to the isotropic freezing experiments, for directional freezing, P_n strongly depends on the concentration of particles. The distribution function (P_n) obeys a power law $P_n \sim n^{-\eta}$, where η varies from 2.27 (for particle concentration ~10^9 particles/mL) to 3.19 (for 10^7 particles/mL). To understand the differences between isotropic and directional ice templating, we compare our experimental results with simulations performed by our collaborators. Their lattice simulations ignore hydrodynamic interactions and instabilities at the growing ice front. These simplified simulations capture the experimental results and reveal

that the differences in scaling of (P_n) arise from differences in how the ice crystals close up on themselves as the freezing front propagates.

We investigate the dynamics of colloidal chains using the linear colloidal constructs obtained from isotropic ice templating.

We study both passive and "active" colloidal chains. Active colloids are those that are not constrained by equilibrium: ballistic propulsion, superdiffusive behavior, or enhanced diffusivities have been reported for active Janus particles. At high concentrations, interactions between active colloids give rise to complex emergent behavior. Their collective dynamics result in the formation of several hundred particle-strong flocks or swarms. We demonstrate significant diffusivity enhancement for colloidal objects that neither have a Janus architecture nor are at high concentrations. We employ uniformly catalyst-coated, viz. chemo-mechanically, isotropic colloids linked into a chain to enforce proximity. Activity arises from hydrodynamic interactions between enchained colloidal beads due to reaction-induced phoretic flows catalyzed by platinum nanoparticles on the colloid surface. This results in diffusivity enhancements of up to 60% for individual chains in dilute solution. Chains with increasing flexibility exhibit higher diffusivities. Simulations (performed by our collaborators), that account for hydrodynamic interactions between enchained colloids due to active phoretic flows accurately capture the experimental diffusivity. These simulations reveal that the enhancement in diffusivity can be attributed to the interplay between chain conformational fluctuations and activity. Our results show that activity can be used to systematically modulate the mobility of soft slender bodies.

Finally, we prepare thermos-responsive colloidal chains and investigate thermally induced reversible collapse transitions in such chains. Micron size polystyrene colloidal beads are coated with thermos-responsive copolymer microgels of PNIPAM and allylamine and are assembled into chains by application of an AC field. The combination of long range electrostatic repulsion between colloids and external AC field-induced dipolar interactions result in linear assemblies of the particles. The colloidal monomers that line up are crosslinked through the amine groups in the microgels, so that the particles remain enchained even after removal of the external electric field. We control the flexibility of the colloidal chain by varying crosslinking time. We vary the suspension temperature from 25^{o}C to 55^{o}C, viz. from below to above the LCST of the PNIPAM microgels. We change the temperature slowly and stepwise

to ensure that chains are in equilibrium when we characterize them. All the chains show a decrease in size on heating. For rigid chains, the decrease in modest and is not accompanied by a change in shape. Flexible chains form relatively compact structures, resulting in a large increase in the local monomer number density. For chains with intermediate flexibility, the balance between chain rigidity and inter-particle attraction results in the formation of helix-like structures. The fraction of monomers that form helix-like structure increases with temperature and plateaus above the collapse transition temperature of the microgel particles.

In the final chapter of the thesis, we present a brief description of interesting problems that could be addressed using the colloidal polymer chains developed in our work.

Chapter-1

Introduction

1.1 INTRODUCTION

Spherical colloidal particles have been used as model systems for gaining insights into different phenomena in condensed matter, such as crystallization, the isotropic-nematic transition and the glass transition.[1–3] Recently, there is growing interest in colloidal particles with more complex shapes and interactions; this interest is fuelled by the use of such colloids in advanced functional materials, by their use in fundamental studies of self-assembly and as a way of mimicking the geometric shape of molecules.[4–6] There are several examples of such colloidal assemblies: regular clusters,[7] chiral chains,[8] rod-like particles,[9] patchy particles and "polymerized" inorganic rod-like nanoparticles have all been recently reported. Assembly of "monomeric" colloidal particles into polymer-like chains would represent a significant step forward in designing a colloidal analogue of polymeric molecules.[10–12]

Several researchers have reported that the assembly of spherical colloidal particles mimics that of atomic condensed matter phases.[13–15] Self-assembly of colloids with short-range[16] or with long-range interactions has been well studied.[17] Recently the ability to control the interaction between colloids has been exploited extensively in experimental soft matter physics.[18,19] A phase transition from liquid to crystal phase as a function of density has been observed.[20] The dynamics of crystallization,[21,22] melting,[23,24] crystal-crystal martensitic transitions,[25] and crystal-gas transitions[15,26] have been investigated in recent developments.

There are several interactions that determine the assembly of colloids, such as the excluded volume interaction,[27] long range electrostatic interactions[28] and short range van der Waals interaction.[29] Further, drag forces in solvents, and capillary forces[30,31] can affect the assembly.[32] A convenient way to control the assembly of colloidal particles is by applying electric or magnetic fields. In a DC field, directional motion of charged colloidal particles has been used to assemble the particles.[33,34] Colloidal assembly can also be efficiently manipulated by imposing an AC field.[34–36] Dipolar interactions between dielectric particles can be tuned by varying the strength and frequency of the field. By changing the field strength and frequency, colloids at a particular volume fraction can be assembled into different structures such as bcc, fcc, string-like phases and so on.[10,37–40] The assembly of colloidal particles in the presence of electric or magnetic fields,[11,41] is typically reversible, viz. the particles re-disperse into the solvent on removing the field. Linking the assembled colloidal "monomers" by, for example, sintering at above their glass transition temperature or by chemical crosslinking, renders the assembled structure permanent so that the monomers stay connected even after removing the field.[10,11]

It has been suggested that linear assemblies of colloids could be considered as models for polymers.[11] Polymers are characterized by topological connectivity with monomers enchained to form a covalently connected polymer.[42] Several static and dynamic properties, such as the size of a polymer chain, or polymer viscosity[43] exhibit remarkably universal scaling with the molecular weight, independent of the chemistry of the polymer. Thus, forming a connected assembly represents an important starting point for the development of a colloidal model for polymers. Polymer dynamics is a function of the chain length and the local stiffness of the polymer chain. Fundamentally, these models will address the role of topological connectivity on the static and dynamics properties of the linearly connected objects.

1.2 COLLOIDS AS BIG ATOMS

It has been seen in experiments as well as computer simulations that colloidal hard spheres[13,44] remain dispersed in a "liquid" phase at volume fraction, $\phi < 0.49$. For $0.49 < \phi < 0.54$, the hard sphere colloid system exhibits liquid-solid co-existence and above $\phi = 0.58$, it transitions to a metastable amorphous glassy phase.[45,46] A similar progression in phase behaviour has been observed for atomic systems when they are cooled from a high temperature fluid state. Note that for atomic systems, inverse of temperature 1/T, plays same role as the volume fraction (ϕ) of colloidal suspensions (Figure 1-1). These big colloidal "atoms" are sufficiently large and

their Brownian motion is sufficiently slow to allow visualization using optical microscopy. The trajectories of colloidal particles can be tracked using image processing[47] - therefore colloids represent a convenient model system to investigate a variety of physical phenomena in atomic and molecular materials.[1] Colloids are known as "designer atoms" since these can be tailored in terms of their interactions, size and shape.[48] Using confocal microscopy, fluorescently labelled colloidal particles in density and refractive indexed matched solvents can be visualized in 3D.[49] In contrast, electron microscopy is required to visualize atoms in bulk atomic systems – however, there are several experimental limitations to electron microscopy. For example, it is not straightforward to use electron microscopy to visualize dynamics in atomic solids.

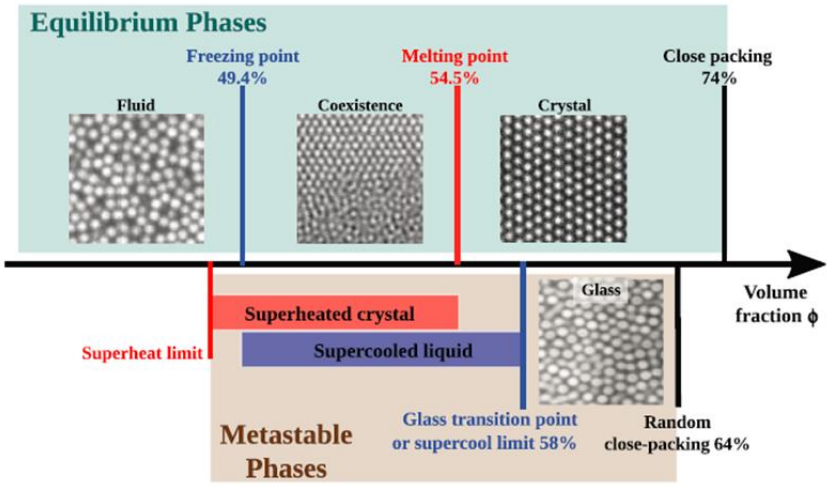

Figure 1-1: (Equilibrium phases) Phase diagram of hard sphere colloids. Freezing points starts at ϕ=49.4% and melting point at ϕ=54.5% and in-between, there is liquid/solid phase coexistence. (Metastable) glassy phase is observed between ϕ=58% and ϕ=64%. Random closed packing is observed above ϕ=64%. All these phases are observed in analogy to atomic systems when the parameter varied is temperature instead of the volume fraction. (Reprinted with permission from ref (20), Copyright ©2016 WILEY-VCH Verlag GmbH & Co. KGaA, Weinheim).

For monodisperse spheres, hexagonal close packing (hcp)[50] represents the densest configuration. Therefore, hcp assembly represents the thermodynamically stable state (lowest energy) for monodisperse hard spheres. There are several ways to assemble colloids into hcp ordered structures. Nagayama investigated[51] assembly from colloidal suspensions by drop casting on a plane glass substrate. They claimed that attractive capillary interactions and convective transport of colloids are the main factors that dominate the self-assembly process and that the degree of order in the packed arrays is determined by the evaporation rate of the

solvent. Centimetre size mono-layer colloidal crystals are formed by controlling the evaporation rate of solvent and the withdrawal velocity of the substrate.[52] An alternative method to prepare hcp colloidal crystals is spin coating. At the time of spin coating, the liquid/solvent flows due to the centrifugal force across a wettable substrate at high shear rate and the colloidal particles rapidly form a densely packed hcp structure on the substrate/glass plate. The resulting crystal quality depends mainly on the spinning speed, rheology of the suspension, the wettability of the substrate, concentration of the colloids and surface charge of the substrate and the charge of the colloidal particles.[53]

For colloidal particles with bi-disperse size distribution, and with opposite charges on particles of different sizes, it has been observed that varying the colloidal particle size ratio yields structures similar to ionic crystals.[54,55] Bartlett *et al.*[55] reported that the binary crystal structure may be switched between fcc, cesium chloride (CsCl) and sodium chloride (NaCl) by simply varying the magnitude of the charge on nearly equal-sized spherical particles. Leunissen et al. reported that the LS-type and LS_6- type ionic crystals (where L and S refers to large and small) were observed by varying the ratio of size between the positive and negatively charged spheres.[54] Figure 1-2a and Figure 1-2b are confocal micrographs of CsCl and LS type crystal. The phase behaviour of charged colloidal suspensions has been studied extensively[56,57] and has been modelled by a pure Yukawa or a hard-sphere-plus-Yukawa potential.[58,59] Yethiraj *et al.* reported the disorder-order phase diagram as a function of softness (*k*R, where 1/*k* is the inverse Debye screening length) and volume fraction (ϕ).[19]

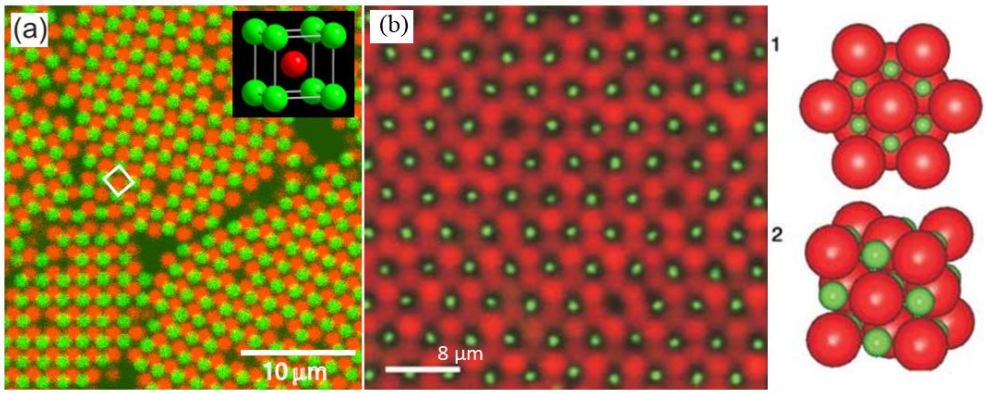

Figure 1-2: (a) Ionic colloidal crystal with oppositely charged colloidal particle with different particle size ratio (CsCl-type crystal), (Reprinted with permission from ref (55), Copyright (2005) by American physical Society). (b) Confocal micrographs of LS-type ionic crystal where L and S refers to large and small. (1) & (2) are the schematics of unit cells in an

hexagonal and cubic representations (Reprinted with permission from ref (54), Copyright (2005) Springer Nature).

van Blaaderen et al. investigated the epitaxial growth of colloidal crystals in 3D formed by slow sedimentation of colloidal particles on a templated surface.[60] It is known that thermodynamically, the free energy of fcc and hcp structures are nearly the same.[61] However a pure fcc crystal is formed when colloids are sedimented on a substrate patterned with the 100 plane of a fcc crystal. Using this epitaxial growth technique, a single crystal as large as the size of the patterned area was formed by sedimentation. Ganapathy et al. showed that island formation of colloids on patterned substrates obeys the same two dimensional nucleation and growth law observed in atomic systems.[62]

Though crystal nucleation has been studied extensively, quantitatively predicting the rate of crystal nucleation remains challenging. The total free energy cost to form a spherical phase of radius *R* is given by classical nucleation theory as[18]

$$\Delta G = -\frac{4}{3}\pi R^3 n_s|\Delta\mu| + 4\pi R^2\gamma \quad (1)$$

where γ is the interfacial free-energy, $|\Delta\mu|$ is the chemical potential difference between the phases and n_s is the number of monomers in the nucleus. According to classical nucleation theory, the nucleation rate per unit volume is given by[18]

$$J = J_0 \exp\left(\frac{-16\pi\gamma^3}{3\,(n_s|\Delta\mu|)^2 k_B T}\right) \quad (2)$$

For hard sphere suspensions, the surface tension, $\gamma = \frac{k_B T}{a^2}$, where a is the radius of the colloidal sphere. Computer simulations[63,64] have been performed to investigate the shape and height of the nucleation barrier, J_0 allowing for quantitative comparison between experiment and theory.

Both classical nucleation theory and simulations are premised on the assumption of homogeneous nucleation of crystals. However, conditions that eliminate heterogeneous nucleation are rarely obtained in experiments. Theoretically, despite the limitations of classical nucleation theory, this remains the starting point to explain phase transitions – though there are attempts to develop alternate frameworks.[65] Often, colloidal systems are prepared, then shear melted and the nucleation process is studied as they recrystallize from the melt. Therefore, we cannot completely rule out the existence of tiny crystals that might alter the nucleation kinetics significantly. Due to these difficulties, large discrepancies are observed experimentally, even

for very simple hard sphere systems. The rate of nucleation depends on the polydispersity of colloids and weak electrostatic interactions between particles.[66] It has been shown that below the melting volume fraction (ϕ=0.545) of hard sphere-like colloidal suspensions, crystallization is well matched with classical nucleation theory. However, at higher volume fractions, crystal growth is suppressed by high nucleation rates.[21] For the case of charged colloids that are experimentally more accessible but that represent theoretical challenges, the kinetics of crystallization has been extensively studied.[67,68]

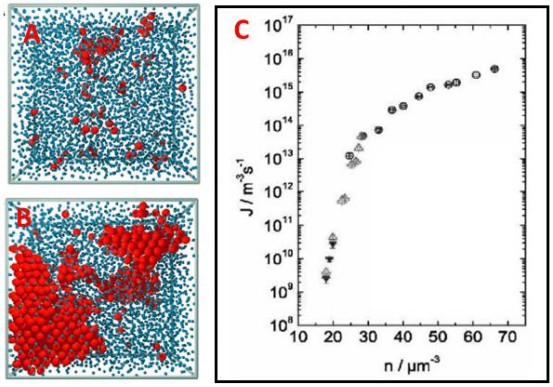

Figure 1-3: (A) & (B) are snapshots during crystallization at a volume fraction ϕ = 0.45. The red spheres represent crystal-like particle and the blue spheres represent the metastable liquid state. (Reprinted with permission from ref (22), Copyright © 2001, The American Association for the Advancement of Science) (C) Nucleation rate as a function of number density. The nucleation rate from time resolved static light scattering data for charged colloids is consistent with classical nucleation theory. (Reprinted with permission from ref (69), Copyright (2005) Rights managed by AIP Publishing).

Colloidal systems have also been used as models to investigate atomic or molecular phenomena other than crystallization. For example, the equivalent of thermal capillary waves have been observed at the interface between colloidal liquid and gas phases. The interface between vapour and liquid appears to be smooth at rest but thermal motion produces statistical fluctuations locally at the interface leading to interfacial roughness. This phenomenon is known as thermally excited capillary waves. These capillary waves play an important role in developing modern theories of interfaces and have been studied using x-ray scattering and light scattering techniques. Aarts *et al.*[70] demonstrated that colloid-polymer dispersions exhibit equilibrium between low and high density disordered phases (analogous to the gas/liquid coexistence). This system was observed to show a fluctuating interface at the colloidal liquid/colloidal gas boundary. These analogues for capillary waves can be directly visualized using real time using

microscopy. Thus, colloidal systems have been shown to exhibit phenomena that are closely analogous to those in atomic/molecular systems (Figure 1-4).

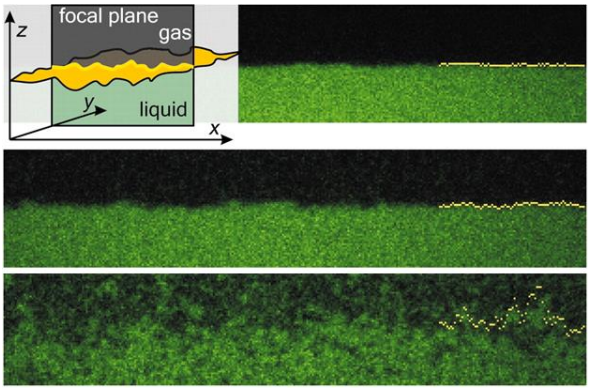

Figure 1-4 : Capillary waves at vapour-liquid interface of a colloidal system. This is imaged using laser scanning confocal microscopy (LSM) at three different state points during the approach towards the critical point (Reprinted with permission from ref(70), copyright (2004) AAAS).

1.3 COLLOIDAL MOLECULES

Low co-ordination number assemblies and complex structures are common in Nature for atomic and molecular systems but are challenging to create in a controllable manner using colloidal particles. Researchers have designed protocols to synthesize a variety of unusual colloidal structures such as dimpled particles,[71] cubic assemblies and clusters of spheres.[7] The geometry of colloidal particles plays an important role in their self-assembly.[72] Only simple high symmetry and high density crystals with fcc and bcc packing can be formed using monodisperse spherical colloids. Complex open structures such as diamond-like packing with four fold coordination are very difficult to realize using spherical colloids. Low coordination states are unstable without bonding (linking) or strong directional interactions between their constituent colloids. Assembly of atoms to form molecules is controlled by its valency. For example, the valence orbitals of carbon adopt sp^3 hybridization to form CH_4 molecules. To create colloidal analogues of CH_4, it is necessary to create colloidal analogues of atoms with directional interactions, for example, through chemically distinct surface patches that mimic the hybridized atomic orbitals. If carbon-analogous colloidal particles have four tetrahedrally coordinated patches, then the hydrogen particles must each have one complementary patch. Assembling such particles through attractive patch-patch interactions has been shown to result in tetrahedral assemblies with the geometry of CH_4 molecules.[73] Similarly by controlling the

number and placement of attractive patches, colloidal assemblies that resemble CH_3, CH_2, CH molecular structures have also been formed (Figure 1-5,A).[73] Sacanna *et al.* reported the self-assembly of colloids with lock and key colloids using depletion interactions (Figure 1-5,B).[74]

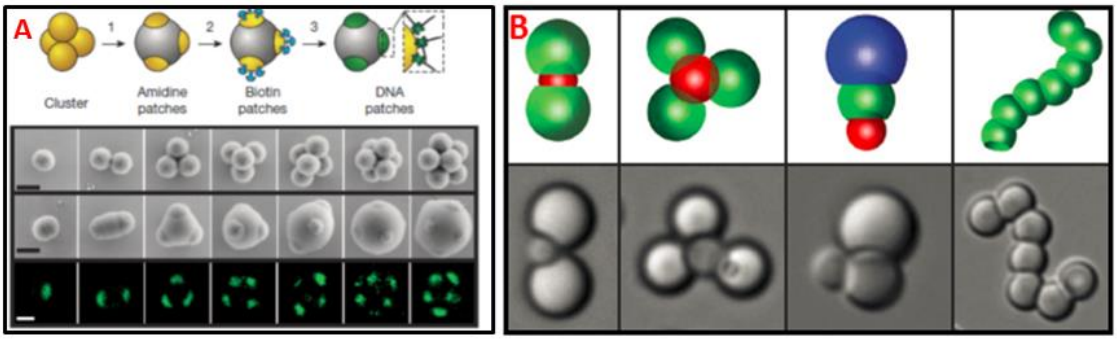

Figure 1-5: DNA patchy particle fabrication. (1st row, A) Well defined symmetric four patche colloidal particles are shown. (1) Cluster of four amidinated PS particles is swollen with styrene such that extremities of cluster protrude from the styrene droplet then styrene is polymerized and the protrusions from the original cluster form patches. (2) Biotin is specifically functionalized on the patches. (3) Biotinylated DNA oligomers are introduced and bind to the patches via biotin-streptavidin-biotin linkages. (2nd row, A) Electron micrographs of amidinated colloidal clusters. (3rd row, A) Electron micrograph of colloids with patches. (4th row, A) Confocal microscopy images of patchy particles. The fluorescent patches corresponding to the dye labelled streptavidin are observed (Reprinted with permission from ref (73), Copyright © 2012, Springer Nature). (B) Self-assembly of colloids with lock and key interactions based on depletion interactions. (Reprinted with permission from ref (74), Copyright © 2010, Springer Nature).

1.4 POLYMER-LIKE LINEAR ASSEMBLY OF COLLOIDAL PARTICLES

We now discuss the assembly of colloids into linear polymer-like assemblies.

1.4.1 BY AC ELECTRIC FIELD

Colloidal particles have, in general, a different dielectric constant from the solvent that they are dispersed in. In a suspension, colloidal particles form different structures in the presence of an AC field,[75,76] where the field strength is 0.1-1 $kV(mm)^{-1}$, for frequencies that range from few tens of KHz to MHz. Under these conditions, colloidal particles show dipolar interactions, with their axis along the electric field direction and assemble into different structures.[10,38–40] If the frequency of the field is a few hundreds of kHz then the particle sees an average field and

small molecule ion migration is minimized. The induced dipole formed by the colloids in the applied field E, is not affected by the presence of neighbouring particles when the inter-particle distance is much larger than the particle radius. The dipolar interaction U(R) between two particles separated by a distance R is given by[18] the equation

$$U(R,\theta) = -\frac{4\pi\varepsilon_0\varepsilon_f\beta^2 a^6 E_0^2}{R^3}\left(\frac{3COS^2\theta-1}{2}\right) \quad (3)$$

Where ε_0 is particle dielectric constant and ε_f is the fluid dielectric constant, a is the particle radius, E_0 is the applied electric field and θ is the angle between the dipolar orientation of the two particles.

It has been shown that for a specific range of particle volume fraction and imposed electric field, particles assemble into linear structures. However, on removing the electric field, the colloidal particles re-disperse into the solvent. To make the linear assembly permanent even after removal of the field, one must induce physical or chemical bonding between two colloids, for example as described by the work of van Blaaderen and co-workers, detailed below.[10] van Blaaderen and co-workers describe the assembly of PMMA colloidal beads in cyclohexyl bromide (CHB), when taken in a thin channel between ITO coated glass plates that act as electrodes (Figure 1-6A). At low field strength, the colloidal particles form linear structures along the electric field direction. Once the linear structure is formed, the cell is heated with hot air (70°-80°C) to elevate the temperature above the glass transition temperature of PMMA for about 3-4 minutes. After removing the AC field it was observed that ≈95% of beads in linear assemblies formed permanent chains with a broad distribution of chain lengths. It was shown that the PHSA-PMMA comb-graft stabilizer present on the particle surface is redistributed in such a way that the colloidal particles become permanently linked together at this elevated temperature.

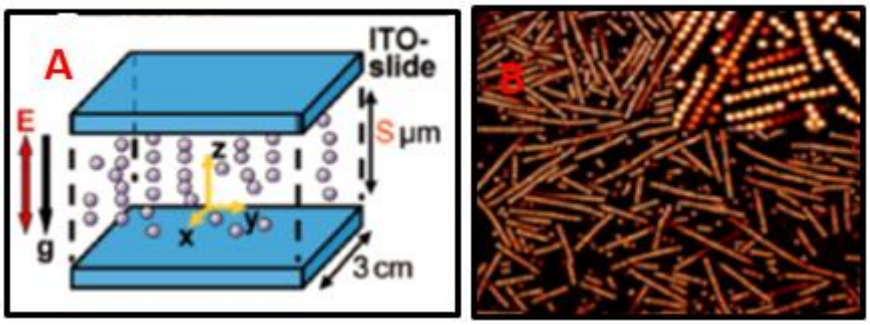

Figure 1-6: (A) Schematic of the cell for imposition of electric field that aligns dielectric spherical colloidal particles. (B) Confocal micro-graphs of permanent colloidal chains of

PMMA particles. Chain length is controlled by varying the distance between the electrodes. A magnified view of the chains is shown in the inset (Reprinted with permission from ref (10), Copyright © 2012 WILEY-VCH Verlag GmbH & Co. KGaA, Weinheim).

1.4.2 BY MAGNETIC FIELD

Magnetic colloidal particles interact via their dipole moment to form chains in an applied magnetic field. The magnetic dipole moment of colloids in magnetic field is given by $m = \frac{4}{3}\pi a^3 \xi H$, where ξ is the magnetic susceptibility of the particles, H is the applied magnetic field and, a is the radius of the particle.[77] The interaction energy between two particles in a magnetic field is given by[77]

$$U_{i,j}(R,\beta) = \frac{m_i m_j}{4\pi \mu_0 R^3}(1 - 3\cos^2\beta) \quad (4)$$

where i, j are the particle indices, R is the magnitude of the position vector between the two particles and β is the angle between the position vector and the applied magnetic field and μ_0 is the permeability of the solvent medium. Thus, it is energetically favourable for the magnetic dipole particles to align in head to tail fashion to form a linear chain, along the direction of magnetic field. It has been observed that magnetic particles assemble linearly within few seconds of imposing a magnetic field. Magnetic particles coated with streptavidin can be linked through biotinylated DNA linkers that bridge neighbouring particles to bind them. This linking allows the colloidal chain to stay permanently connected, even after removing the magnetic field. The flexibility of the colloidal chains can be tuned by varying the density of linker chains between two particles. If the cross-linking density is high, rigid chains are observed to form and while flexible chains form at lower linker density. The particle to particle distance can be controlled by the magnetic field strength. If the particle to particle distance $r > \ell N^{\frac{1}{2}}$, the chain is flexible and for $r < \ell N^{\frac{1}{2}}$, the chains are rigid (where ℓ is the polymer segment length and N is the number of segments in DNA).[77]

1.5 OBJECTIVE OF THE THESIS

While several articles explore the synthesis of colloidal linear chains,[10–12] to the best of our knowledge, only a few papers[10,11] discuss the structure and dynamics of so-formed linearly connected objects. This thesis focuses on the preparation of linear chains and on studies of their

structure, dynamics and phase transitions. In this thesis, we present novel techniques based on ice templating, to assemble colloidal particles.[78] We investigate both isotropic and directional ice templating methods to assemble colloids. The distribution of colloidal assemblies formed through the ice-templating protocol is characterized in great detail. We also prepare chains by crosslinking colloids organized in an AC electric field. A novel aspect of this work is to render the colloidal chains active, viz. out of equilibrium, by adsorbing catalytic platinum nanoparticles on their surface and by conducting reactions catalysed by the nanoparticles. Another novel aspect is to render the colloidal chains thermoresponsive by adhering poly N-isopropyl acrylamide microgel particles[79,80] on the colloidal surface.

1.6 OUTLINE OF THE THESIS

Chapter-1: In the 1st chapter, the relevant background literature is surveyed to motivate our investigation of the assembly of colloidal particles and our studies of their structure and dynamics.

Chapter-2: We have investigated isotropic ice templating of aqueous dispersions of polymer coated colloids and cross-linker at particle concentrations far below that required to form percolated monoliths. In this process, colloidal particles assemble into three different structures, linear chains, two particle-wide tapes and sheets. We have found that the fractional probability P_n (n>2) [n is the number of particles in a cluster] of particles that are in a cluster is independent of particle concentration for isotropic ice templating (over a 100-fold variation in concentration from 10^6 *to* 10^8 particles/ mL). In this concentration range, the cluster size distribution exhibits a power law, $P_n \sim n^{-2}$, for clusters containing less than ~ 30 particles.

Chapter-3: In this work, we describe particle assembly through directional ice templating. Here too, particles assemble into linear chains, two particle-wide tape and sheets. We found that the fractional probability P_n(n>2) of particles in a cluster in a strong function of concentrations and the cluster size distribution exhibit power law $P_n \sim n^{-\eta}$, where η varies from 2.27 (for higher particle concentrations ~10^9 particles /mL) to 3.19 (for low particle concentrations of the order of 10^7 particles /mL).

Chapter-4: We present centre of mass diffusion data for passive and active colloidal chains. We found that the experimentally measured diffusion coefficient (D) is consistent with Zimm's treatment ($D_N \sim N^{-0.58}$, N is the number monomers in a linear chain) for the dynamics of

semi-flexible chains. We control the flexibility of assembled structures by controlling the linking density between beads. We have demonstrated that the diffusion of passive Brownian chains does not depend on chain flexibility whereas the diffusion of "active" colloidal chains is a function of their flexibility. This is the first experimental demonstration of the link between diffusivity and flexibility.

Chapter-5: We study the temperature-driven phase transition of PNIPAM micro-gel grafted thermo-responsive colloidal chain. Above the LCST of PNIPAM, these chains behave like they are in a bad solvent and exhibit strong monomer-monomer attractive interactions. There is a decrease in the size of the chains, as measured by the end-to-end distance. Rigid chains show a modest decrease in size but exhibit no qualitative change in their shape. Relatively flexible chains form compact structures as they collapse, resulting a large increase in the local monomer number density within the chain. Chains with intermediate flexibility show the formation of helix-like structures on heating.

Chapter-6: In this chapter, we provide a summary of the key findings of this thesis and we present a brief description of potential problems that could be addressed using the colloidal polymer chains developed in our work.

1.7 REFERENCES

1. Anderson, V. J. & Lekkerkerker, H. N. W. Insights into phase transition kinetics from colloid science. *Nature* **416**, 811 (2002).

2. Kegel, W. K. & van Blaaderen, A. Direct observation of dynamical heterogeneities in colloidal hard-sphere suspensions. *Science* **287**, 290–293 (2000).

3. Pham, K. N. *et al.* Multiple glassy states in a simple model system. *Science* **296**, 104–106 (2002).

4. Glotzer, S. C. & Solomon, M. J. Anisotropy of building blocks and their assembly into complex structures. *Nat. Mater.* **6**, 557–562 (2007).

5. van Blaaderen, A. Chemistry: Colloidal molecules and beyond. *Science* **301**, 470–471 (2003).

6. Yang, S. M., Kim, S. H., Lim, J. M. & Yi, G. R. Synthesis and assembly of structured colloidal particles. *J. Mater. Chem.* **18**, 2177–2190 (2008).

7. Manoharan, V. N., Elsesser, M. T. & Pine, D. J. Dense packing and symmetry in small clusters of microspheres. *Science* **301**, 483–487 (2003).

8. Zerrouki, D., Baudry, J., Pine, D., Chaikin, P. & Bibette, J. Chiral colloidal clusters. *Nature* **455**, 380–382 (2008).

9. Vroege, G. J. & Lekkerkerker, H. N. W. Phase transitions in lyotropic colloidal and polymer liquid crystals. *Reports Prog. Phys.* **55**, 1241 (1992).

10. Vutukuri, H. R. *et al.* Colloidal analogues of charged and uncharged polymer chains with tunable stiffness. *Angew. Chemie - Int. Ed.* **51**, 11249–11253 (2012).

11. Byrom, J., Han, P., Savory, M. & Biswal, S. L. Directing assembly of DNA-coated colloids with magnetic fields to generate rigid, semiflexible, and flexible chains. *Langmuir* **30**, 9045–9052 (2014).

12. Bannwarth, M. B. *et al.* Colloidal polymers with controlled sequence and branching constructed from magnetic field assembled nanoparticles. *ACS Nano* **9**, 2720–2728 (2015).

13. Pusey, P. N. & Van Megen, W. Phase behaviour of concentrated suspensions of nearly hard colloidal spheres. *Nature* **320**, 340–342 (1986).

14. Pieranski, P. Two-dimensional interfacial colloidal crystals. *Phys. Rev. Lett.* **45**, 569–572 (1980).

15. Li, B., Zhou, D. & Han, Y. Assembly and phase transitions of colloidal crystals. *Nat. Rev. Mater.* **1**, (2016).

16. Pham, K. N., Egelhaaf, S. U., Pusey, P. N. & Poon, W. C. K. Glasses in hard spheres with short-range attraction. *Phys. Rev. E* **69**, 11503 (2004).

17. Sciortino, F., Mossa, S., Zaccarelli, E. & Tartaglia, P. Equilibrium cluster phases and low-density arrested disordered states: the role of short-range attraction and long-range repulsion. *Phys. Rev. Lett.* **93**, 55701 (2004).

18. Yethiraj, A. Tunable colloids: control of colloidal phase transitions with tunable interactions. *Soft Matter* **3**, 1099 (2007).

19. Yethiraj, A. & van Blaaderen, A. A colloidal model system with an interaction tunable

from hard sphere to soft and dipolar. *Nature* **421**, 513–517 (2003).

20. Wang, F., Zhou, D. & Han, Y. Melting of Colloidal Crystals. *Adv. Funct. Mater.* **26**, 8903–8919 (2016).

21. Harland, J. L. & Van Megen, W. Crystallization kinetics of suspensions of hard colloidal spheres. *Phys. Rev. E* **55**, 3054 (1997).

22. Gasser, U., Weeks, E. R., Schofield, A., Pusey, P. N. & Weitz, D. A. Real-space imaging of nucleation and growth in colloidal crystallization. *Science* **292**, 258–262 (2001).

23. Li, B. *et al.* Modes of surface premelting in colloidal crystals composed of attractive particles. *Nature* **531**, 485–488 (2016).

24. Wang, Z., Wang, F., Peng, Y. & Han, Y. Direct observation of liquid nucleus growth in homogeneous melting of colloidal crystals. *Nat. Commun.* **6**, 6942 (2015).

25. Weiss, J. A., Oxtoby, D. W., Grier, D. G. & Murray, C. A. Martensitic transition in a confined colloidal suspension. *J. Chem. Phys.* **103**, 1180 (1995).

26. Savage, J. R., Blair, D. W., Levine, A. J., Guyer, R. A. & Dinsmore, A. D. Imaging the sublimation dynamics of colloidal crystallites. *Science* **314**, 795–798 (2006).

27. Baranov, D. *et al.* Assembly of colloidal semiconductor nanorods in solution by depletion attraction. *Nano Lett.* **10**, 743–749 (2010).

28. Aizenberg, J., Braun, P. V & Wiltzius, P. Patterned colloidal deposition controlled by electrostatic and capillary forces. *Phys. Rev. Lett.* **84**, 2997 (2000).

29. Rance, G. A., Marsh, D. H., Bourne, S. J., Reade, T. J. & Khlobystov, A. N. Van der waals interactions between nanotubes and nanoparticles for controlled assembly of composite nanostructures. *ACS Nano* **4**, 4920–4928 (2010).

30. Kralchevsky, P. A. & Denkov, N. D. Capillary forces and structuring in layers of colloid particles. *Curr. Opin. Colloid Interface Sci.* **6**, 383–401 (2001).

31. Cong, H. & Cao, W. Colloidal crystallization induced by capillary force. *Langmuir* **19**, 8177–8181 (2003).

32. Kitaev, V. & Ozin, G. A. Self-Assembled Surface Patterns of Binary Colloidal Crystals. *Adv. Mater.* **15**, 75–78 (2003).

33. Ganapathy, R., Buckley, M. R., Gerbode, S. J. & Cohen, I. Direct measurements of island growth and step-edge barriers in colloidal epitaxy. *Science* **327**, 445–448 (2010).

34. Trau, M., Saville, D. A. & Aksay, I. A. Field-Induced Layering of Colloidal Crystals. *Science* **272**, 706–709 (1996).

35. Trau, M., Saville, D. A. & Aksay, I. A. Assembly of colloidal crystals at electrode interfaces. *Langmuir* **13**, 6375–6381 (1997).

36. Velev, O. D. & Kaler, E. W. In situ assembly of colloidal particles into miniaturised biosensors. *Langmuir* **15**, 3696–3698 (1999).

37. Leunissen, M. E., Vutukuri, H. R. & Van Blaaderen, A. Directing colloidal self-assembly with biaxial electric fields. *Adv. Mater.* **21**, 3116–3120 (2009).

38. Schmidle, H., Jäger, S., Hall, C. K., Velev, O. D. & Klapp, S. H. L. Two-dimensional colloidal networks induced by a uni-axial external field. *Soft Matter* **9**, 2518–2524 (2013).

39. Rutkowski, D. M., Velev, O. D., Klapp, S. H. L. & Hall, C. K. Simulation study on the structural properties of colloidal particles with offset dipoles. *Soft Matter* **13**, 3134–3146 (2017).

40. Halsey, T. C. & Toor, W. Structure of electrorheological fluids. *Phys. Rev. Lett.* **65**, 2820–2823 (1990).

41. Erb, R. M., Son, H. S., Samanta, B., Rotello, V. M. & Yellen, B. B. Magnetic assembly of colloidal superstructures with multipole symmetry. *Nature* **457**, 999–1002 (2009).

42. de Gennes, P. G. *Scaling Concepts in Polymer Physics*. (Cornell University Press, 1980).

43. Schreiber, H. P., Bagley, E. B. & West, D. C. Viscosity/Molecular weight relation in bulk polymers—I. *Polymer (Guildf).* **4**, 355–364 (1963).

44. Brambilla, G. *et al.* Probing the equilibrium dynamics of colloidal hard spheres above the mode-coupling glass transition. *Phys. Rev. Lett.* **102**, 85703 (2009).

45. Alder, B. J., Hoover, W. G. & Young, D. A. Studies in Molecular Dynamics. V. High-Density Equation of State and Entropy for Hard Disks and Spheres. *J. Chem. Phys.* **49**, 3688–3696 (1968).

46. Kirkwood, J. G. Molecular distribution in liquids. *J. Chem. Phys.* **7**, 919–925 (1939).

47. Crocker, J. C. & Grier, D. G. Methods of digital video microscopy for colloidal studies. *J. Colloid Interface Sci.* **179**, 298–310 (1996).

48. Frenkel, D. Playing tricks with designer" atoms". *Science* **296**, 65–66 (2002).

49. Weeks, E. R., Crocker, J. C., Levitt, A. C., Schofield, A. & Weitz, D. A. Three-dimensional direct imaging of structural relaxation near the colloidal glass transition. *Science* **287**, 627–631 (2000).

50. Sun, Z. & Yang, B. Fabricating colloidal crystals and construction of ordered nanostructures. *Nanoscale Res. Lett.* **1**, 46–56 (2006).

51. Dushkin, C. D., Nagayama, K., Miwa, T. & Kralchevsky, P. A. Colored multilayers from transparent submicrometer spheres. *Langmuir* **9**, 3695–3701 (1993).

52. Nagayama, K. Two-dimensional self-assembly of colloids in thin liquid films. *Colloids Surfaces A Physicochem. Eng. Asp.* **109**, 363–374 (1996).

53. Ye, X. & Qi, L. Two-dimensionally patterned nanostructures based on monolayer colloidal crystals: controllable fabrication, assembly, and applications. *Nano Today* **6**, 608–631 (2011).

54. Leunissen, M. E. *et al.* Ionic colloidal crystals of oppositely charged particles. *Nature* **437**, 235–240 (2005).

55. Bartlett, P. & Campbell, A. I. Three-dimensional binary superlattices of oppositely charged colloids. *Phys. Rev. Lett.* **95**, 128302 (2005).

56. Monovoukas, Y. & Gast, A. P. The experimental phase diagram of charged colloidal suspensions. *J. Colloid Interface Sci.* **128**, 533–548 (1989).

57. Sirota, E. B. *et al.* Complete phase diagram of a charged colloidal system: A synchrotron x-ray scattering study. *Phys. Rev. Lett.* **62**, 1524–1527 (1989).

58. Robbins, M. O., Kremer, K. & Grest, G. S. Phase diagram and dynamics of Yukawa systems. *J. Chem. Phys.* **88**, 3286–3312 (1988).

59. El Azhar, F., Baus, M., Ryckaert, J. P. & Meijer, E. J. Line of triple points for the hard-core Yukawa model: A computer simulation study. *J. Chem. Phys.* **112**, 5121–5126

(2000).

60. A. V. Blaaderen, R. Ruel & P. Wiltzius. letters to nature Template-directed crystallization colloidal. *Nature* **385**, 321 (1997).

61. Frenkel, D. & Ladd, A. J. C. New Monte Carlo method to compute the free energy of arbitrary solids. Application to the fcc and hcp phases of hard spheres. *J. Chem. Phys.* **81**, 3188–3193 (1984).

62. Ganapathy, R., Buckley, M. R., Gerbode, S. J. & Cohen, L. Direct measurements of Island growth and step-edge barriers in colloidal epitaxy. *Science* **327**, 445–448 (2010).

63. Auer, S. & Frenkel, D. Prediction of absolute crystal-nucleation rate in hard-sphere colloids. *Nature* **409**, 1020 (2001).

64. Auer, S. & Frenkel, D. Crystallization of weakly charged colloidal spheres: a numerical study. *J. Phys. Condens. Matter* **14**, 7667 (2002).

65. Dixit, N. M. & Zukoski, C. F. Kinetics of crystallization in hard-sphere colloidal suspensions. *Phys. Rev. E* **64**, 41604 (2001).

66. Auer, S. & Frenkel, D. Suppression of crystal nucleation in polydisperse colloids due to increase of the surface free energy. *Nature* **413**, 711 (2001).

67. Meijer, E. J. & Frenkel, D. Melting line of Yukawa system by computer simulation. *J. Chem. Phys.* **94**, 2269–2271 (1991).

68. Palberg, T. Crystallization kinetics of repulsive colloidal spheres. *J. Phys. Condens. Matter* **11**, R323 (1999).

69. Wette, P., Schöpe, H. J. & Palberg, T. Microscopic investigations of homogeneous nucleation in charged sphere suspensions. *J. Chem. Phys.* **123**, (2005).

70. Aarts, D. G. A. L. Direct Visual Observation of Thermal Capillary Waves. *Science* **304**, 847–850 (2004).

71. Sacanna, S., Irvine, W. T. M., Chaikin, P. M. & Pine, D. J. Lock and key colloids. *Nature* **464**, 575–578 (2010).

72. Manoharan, V. N. Colloidal matter: Packing, geometry, and entropy. *Science* **349**, 1253751–1253751 (2015).

73. Wang, Y. *et al.* Colloids with valence and specific directional bonding. *Nature* **491**, 51–55 (2012).

74. Sacanna, S., Irvine, W. T. M., Chaikin, P. M. & Pine, D. J. Lock and key colloids. *Nature* **464**, 575–578 (2010).

75. Bharti, B., Findenegg, G. H. & Velev, O. D. Co-assembly of oppositely charged particles into linear clusters and chains of controllable length. *Sci. Rep.* **2**, 1–5 (2012).

76. Yanai, N., Sindoro, M., Yan, J. & Granick, S. Electric field-induced assembly of monodisperse polyhedral metal–organic framework crystals. *J. Am. Chem. Soc.* **135**, 34–37 (2012).

77. Byrom, J., Han, P., Savory, M. & Biswal, S. L. Directing assembly of DNA-coated colloids with magnetic fields to generate rigid, semiflexible, and flexible chains. *Langmuir* **30**, 9045–9052 (2014).

78. Deville, S. Ice-templating, freeze casting: Beyond materials processing. *J. Mater. Res.* **28**, 2202–2219 (2013).

79. Li, Y. & Tanaka, T. Phase transitions of gels. *Annu. Rev. Mater. Sci.* **22**, 243–277 (1992).

80. Hirokawa, Y. & Tanaka, T. Volume phase transition in a nonionic gel. *J. Chem. Phys.* **81**, 6379–6380 (1984).

Chapter-2

Colloidal Assembly by Isotropic Ice Templating

The simulations presented in this Chapter are performed by Dr. Chandan Kumar Choudhury (CSIR-NCL). Simulation results are presented for completeness.

2.1 INTRODUCTION

When an aqueous solution or dispersion is frozen, the ice crystals that form, exclude solutes and dispersed particles. These solutes or dispersed particles are spatially localized in the interstitial regions between ice crystals that form as water freezes. Subsequent removal of the ice, typically by freeze drying, results in formation of a porous material as a negative replica of the ice crystals. The process, called ice templating or, ice segregation-induced self-assembly (ISISA) has emerged as a powerful technique for the production of macro-porous materials.[1–3] There are several advantages to ice templating: it uses water as a solvent and, is therefore, environmentally friendly and, economical. Further, the processing equipment required to practise ice templating are widely accessible since they are relatively inexpensive.

Ice templating is not a new technique: reports of usage of synthetic cryo-gels in the biomedical literature go back several decades.[4,5] Ice templating has been used to prepare porous monoliths from rubber latex,[6] from thermoset resorcinol-formaldehyde,[7] as well as from a wide variety of biocompatible polymers, including, collagen, polylactic acid, polyglycolic acid, gelatin,

etc.[8–12] Freeze-drying induced partial crystallization of polymers, such as poly(vinyl alcohol) has also been used to generate porous structures.[13] Ice templating of ceramic slurries has been employed to freeze cast a variety of near net shape porous products. Recently, there has been tremendous interest in combining ice templating with directional freezing to produce oriented structures. This was pioneered by researchers from DuPont[14] who demonstrated that directional freezing of an aqueous solution of silicic acid and, its subsequent polymerization resulted in the formation of oriented silica wires. In the last decade, researchers have extended directional ice templating to produce aligned titania fibers[15] and macro-porous aligned honeycomb monoliths of silica or combinations of alumina and silica.[16,17] Aligned 1-D and 2-D structures comprising polymer or polymer-inorganic composites have also been produced by directional templating followed by freeze drying.[18] Nacre-like tough layered composites have been produced in a two-step process by forming alumina sheets through directional ice templating, followed by in-filling with either epoxy or metal[19,20] or even a glassy phase.[21] Oriented anisotropic polymer nanocomposite hybrids have also been reported by other researchers,[22–24] attesting to the versatility of directional ice templating.

Control over the properties of ice-templated materials requires a thorough understanding of the development of structure as solutes or dispersed particles are organized by growing ice crystals. Apart from porous materials synthesis, this understanding has implications for waste water treatment[25] and geophysical phenomena such as freezing of wet soil.[26] The interaction between dispersed particles and a solid-liquid interface was examined by Uhlmann and co-workers.[27] By balancing the hydrodynamic lubrication forces experienced by a suspended particle as it is approached by a growing solid interface, with the attractive interaction between the particle and the interface, they determined a critical velocity for the interface, above which the particles are overgrown by the solid medium and trapped within it. At velocities lower than the critical velocity of ice front, particles are unable to penetrate the growing solid front and are aggregated at the liquid-solid interface. Experimental studies[28] suggested that this critical velocity for particle trapping as water was frozen, was higher in ice grain boundary grooves. The presence of a gradient of temperature or solute concentration at the ice-water interface can also influence ice growth. The ice front can become unstable as a consequence of such gradients and break up into cellular structures, characterized by a wavelength, l_c, that is predicted by the linear Mullins-Sekerka theory.[29–31] The presence of particles at the ice growth front also results in constitutional undercooling and, depresses the freezing point of the water – similar to the case

of atomic or molecular systems. Further, as particles accumulate at the ice front, the transport properties change in a highly nonlinear manner – unlike the case of atomic or molecular systems. By carefully accounting for these, significant progress has recently been made in understanding ice structure formation during freezing of aqueous colloidal dispersions and theoretical estimates of the conditions for the onset of growth instabilities are now available.[32-33] Following this approach, the group of Deville[34–37] has determined an experimental "phase diagram" for instabilities in ice growth in colloidal dispersions. Specifically, they have identified regions where particles are rejected by the ice and are concentrated at the ice-water interface, as well as metastable and unstable regions, where transverse ice lenses are likely to form. We note that, based on their observations, particles up to a micron in size are always rejected by the growing ice front for ice growth velocities of ~O(0.1 – 1 μm/s).

Thus, while experimental implementation of ice templating is simple, a detailed understanding of the effects of solute and colloids on solidification is important for controlling the structure of the porous aggregate formed. Our understanding of structure development during freezing of aqueous systems containing both dispersed colloid and dissolved polymers is incomplete. For example, Zhang and co-workers[18] note that the presence of a small fraction of polymer, poly (vinyl alcohol) critically influences the shape of the ice-templated structures formed by directional ice-templating of silica colloidal dispersions. Plate like objects are formed in the absence of the polymer while aligned porous structures resulted while ice-templating polymer/colloid hybrids. Similarly, Shi and co-workers[24] have noted that the presence of a polymeric "mortar" (in their case, poly-N-isopropylacrylamide) was essential for the formation of anisotropic rod morphologies by direction ice templating of silica particle dispersions. The reasons that underly these observations are not fully understood at this time.

It has been demonstrated[38] by our group that the formation of porous hybrid structures by ice templating an aqueous dispersion containing rigid colloidal particles, polymer and cross-linker, followed by crosslinking of the hybrid structure in the frozen state. This process does not require freeze drying since the hybrid structure is covalently crosslinked. Thus, the ice can simply be thawed to recover a porous monolith. Remarkably, it is been observed that these monoliths are elastic and can be reversibly compressed to about 10% of their original size – even when the inorganic content exceeds 90% by weight. This behaviour was observed for porous materials prepared using various colloids (silica particles, polystyrene latex and hydroxyapatite particles), for different polymers (polyethyleneimine and gelatin) and for

different crosslinking chemistries. It was concluded[38] that the mechanical response observed was a consequence of a unique microstructure in the particle-polymer hybrid that was created by crosslinking during ice templating.

In most of the previous investigations, the focus was on the synthesis of macroscopic assemblies or monoliths. Therefore, these studies used colloidal dispersions containing a relatively large volume fraction of colloids. Here, we investigate the formation of colloidal aggregates by ice templating extremely dilute colloidal dispersions and, by crosslinking the assemblies of polymer coated colloids in the frozen state. The dispersion concentrations used here are far below that required for a transition to percolated porous monoliths. We demonstrate that the colloidal assemblies exhibit a progression of shapes from linear assemblies to tape-like structures to 2D aggregates. Simulations that rely on a simple kinetic model of particles being expelled by growing ice crystals are able to capture the qualitative features of the particle clusters formed.

2.2 MATERIALS AND METHODS

2.2.1 MATERIALS

Poly(ethylene imine), PEI (50% w/v solution; molecular weight specified by supplier, M_w= 750 kg/mol) and polyethylene-glycol di-epoxide (PEG-di-epoxide, supplier specified M_n = 500 g/mol) were obtained from Sigma-Aldrich and, were used as received. Fluorescent polystyrene (PS) latex particles, 1.08 µm in size with a polydispersity of 4% were used as received from Microparticle GmbH, Germany. These particles were negatively charged with sulphonic acid groups on their surface and, were supplied as 2.5% w/v aqueous dispersions. DI water was used from a Millipore system (pH = 7, resistivity = 18.2 MΩcm).

2.2.2 SAMPLE PREPARATION

1µL of PS latex dispersion (~ 4.8×10^7 particles) was added to 100 µL DI water. This was sonicated for one minute, followed by a minute of vortexing to prepare a uniform colloidal dispersion. 1.5µL of a stock solution of PEI (prepared by adding 100 mg of as received PEI in 1ml of DI water) was diluted by adding to 100µL DI water and vortexing for 2 minutes. While the PEI solution is vortexed, the latex dispersion is added slowly. After addition of the latex, the sample is centrifuged at 3000 rpm for 8 minutes. The supernatant (corresponding to about 75% of the solution) is carefully removed using a micropipette. We note that there is almost no

loss of particles in the washing step since only about 75% of the supernatant is removed and, since care is taken to pipette it out gently. 200µL DI water is added to the sedimented latex particles and they were re-dispersed by ultra-sonication for two minutes and vortexing for one minute. Subsequently, the dispersion is further diluted by addition of 280µL DI water. This washing step, viz. centrifugation and re-dispersion was performed one more time. 3µL PEG-diepoxide is diluted in 100µL of water and vortexed for a minute. To this, the latex dispersion is added while continuously vortexing. After addition of the latex dispersion, the sample is transferred to a freezer maintained at -18^{o}C and, is stored for 12 hours, during which time the water freezes, and, crosslinking proceeds. Subsequently, the sample is thawed at room temperature for 30-40 minutes and is loaded in a microscope cavity slide and sealed. Particles and particle clusters in the sealed sample are allowed to settle over an hour before the sample is imaged. Similarly, we prepare samples at different particle concentrations: 2.96 × 10^8 particles/ml 5.41 × 10^7 particles/ml, 7.39 × 10^7 particles/ml, 3.39 ×10^6 particles/ml and 8.46 ×10^5 particles/ml.

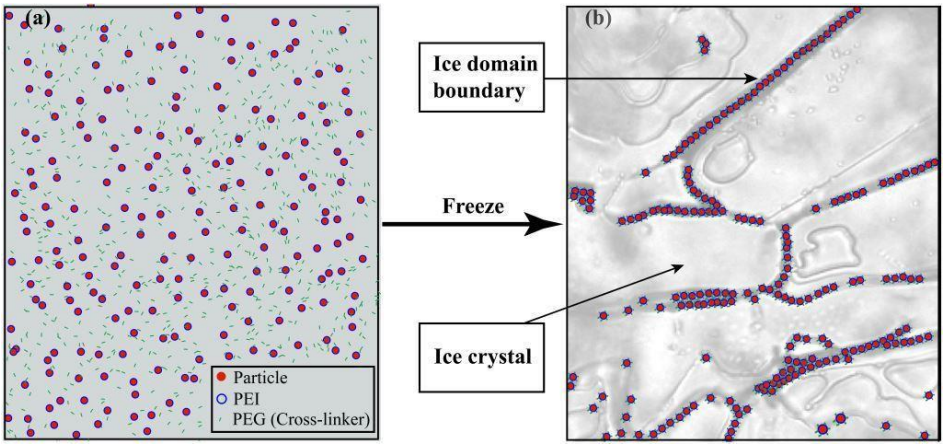

Figure 2-1: Schematic of the isotropic ice templating process. On freezing a dilute dispersion, latex particles (in red), polymer (PEI, in blue) and cross-linker (in green), segregate to the boundaries of ice crystals and are crosslinked to form clustered aggregates.

2.2.3 EXPERIMENTAL METHODS AND IMAGE ANYALYSIS

Laser Scanning Fluorescence Microscopy was performed using a Carl Zeiss Axio Observer Z1 with a 40X objective (NA = 0.75 and working distance = 0.71 mm). Laser light (wavelength = 543 nm) was used to excite the fluorescent PS particles and images were collected using a 610 nm emission filter. We collected over 200 images at each concentration and analysed these to characterize particle clustering. At the lowest

particle concentration (8.46×10^5 particles/ml), images containing nearly 7500 particles were analysed while at the highest concentration (2.96×10^8 particles/ml), there were nearly 140,000 particles in the images analysed.

Image analysis was performed using ImageJ software. After subtraction of a constant background, the images were thresholded and converted into binary. We then employed the inbuilt particle analysis option in Image J to obtain the area and perimeter of each cluster in the image.

2.2.4 DETERMINE THE PORE SIZE (NEGATIVE REPLICA OF ICE CRYSTAL)

To measure the pore size we make scaffold with high volume fraction of polymers (PEI and cross linkers). We thaw it to melt the ice crystal and now the pore is the negative replica of the ice crystal. SEM images indicate the pores are not strictly spherical. We analyse the SEM images using ImageJ and use edge-detection to identify the pores and obtain their size as the largest length scale of the pore. This are the apparent pore size.

2.3 COMPUTATIONAL DETAILS

In the simulation scheme to investigate aggregate formation during ice templating, Brownian dynamics is used to model the motion of individual colloids. It is anticipated, based on our experiments, that colloid aggregation is essentially a kinetic phenomenon, driven by particle expulsion at the water-ice interface. Thus, a minimal simulation scheme is implemented, where hydrodynamic interactions are neglected between colloids. Colloidal particles are modelled as hard spheres, with a diffusion coefficient ($D = 0.2235\ \mu m^2 s^{-1}$) that is estimated from the Stokes Einstein relation for 1 μm colloids diffusing in water at a temperature, T = 273.15K. Thus,

$$D = (k_B\ T)/(6\ \pi\ \eta\ a) \qquad (1)$$

Where, k_B is the Boltzmann constant, η is the viscosity of water at 273.15 K, and a (= 0.5 μm) is the radius of the colloidal particles.

An updated equation (2) for the position of particles(x) is implemented in the simulation

$$x = x + \sqrt{2Ddt}\ r \qquad (2)$$

Where r is a random number drawn from a normal distribution with mean = 0 and standard deviation = 1 and, dt represents the simulation time step. The time step was set to 0.5 ms. The size of the colloidal particles was taken as unity. The colloidal particles are allowed to translate in three dimensions according to Equation 2. Simulations are carried out for dilute dispersions of the colloidal particles, in the absence of ice crystals and confirmed that the mean square displacement is linear in time and, has a diffusion constant (obtained from the slope) of 0.22 $\mu m^2 s^{-1}$.

The isotropic ice templating simulations by placing colloidal particles and ice nuclei, with their centers randomly located in the simulation box. At the start of the simulation, the ice nuclei were treated as point particles with a size of 10^{-3} times that of the colloidal particles. We do not have direct evidence that the growth of ice crystals is uniform for isotropically frozen samples. This is one of the assumptions that we use to simplify our simulations. In this scheme, all the ice crystals nucleate at t = 0 and grow isotropically with a growth rate of 100 nm s^{-1} (viz. 0.1 units/s). The value of the growth rate is based on experimental estimates for ice growth in our experiments (see Results section). The number density of ice nuclei is chosen to correspond with the average number density of ice crystals in our experiments.

As the ice crystals grow, the motion of the colloidal particles is restricted since the volume available to the particles decreases. The following rules are implemented to dictate particle motion:

(a) If a particle overlaps with another particle during a move, then the move is rejected.

(b) If a particle overlaps with an ice crystal, the motion is reflected. Thus, if a move such that: $x_p = x_p + \delta x$, results in overlap of the particle position with ice, then we implement: $x_p = x_p - \delta x$ (where x_p is the position of the colloid and δx ($=\sqrt{2Ddt}\ r$) is its translation, determined by Equation 2). If the particle overlaps with an ice particle even after the move is mirrored, the move is rejected. Initially all systems were equilibrated for 2500 steps. This equilibrated coordinates were used to investigate the effect of ice growth on the aggregation of colloidal particles. The simulations were stopped when we visually observed aggregation of the colloidal particles, resulting in a cessation of their Brownian motion. The trajectory was written after every 500 ms (= 1000 steps). Aggregation time was observed to vary with particle concentration. All simulations were carried out in triplicate using three sets of initial coordinates.

Systems with particle concentrations of 10^6, 10^7, 10^8, and 10^9 colloidal particles per ml are investigated. The number of particles, ice nuclei and box dimensions corresponding to these concentrations are tabulated in Figure 2-1. Periodic boundary conditions are applied in all three directions and used minimum image convention.[39]

Concentration of colloidal particles per ml	No. of colloidal particles in simulation box	No. of ice nuclei in simulation box	Total no. of particles in simulation box	Box dimensions (μm)
10^6	1000	5000	6000	1000.0×1000.0×1000.0
10^7	1000	500	1500	464.1 × 464.1 × 464.1
10^8	950	50	1000	215.0 × 215.0 × 215.0
10^9	995	5	1000	100.0 × 100.0 × 100.0

Table 2-1: Simulation details for isotropic cooling.

2.4 RESULTS AND DISCUSSIONS

The PS colloids used in these experiments are negatively charged and therefore, PEI chains adsorb on their surface. The characterization of the adsorption of PEI on these latices using zeta potential measurements has been demonstrated previously.[40] In this work, a dilute aqueous dispersion of PEI coated PS colloids is frozen, by storing at $-18^{o}C$. As the water forms ice crystals, particles, PEI and cross-linker are expelled at the water-ice boundary, schematics of the isotropic ice templating process is provided in Figure 2-1. The preparation of macro-porous colloid/crosslinked PEI hybrid materials by ice-templating of particle dispersions (at particle concentrations that are significantly higher than in this work) has been reported.[38] These macro-porous monoliths were characterized by approximately isotropic pores. Also, while the pores were not monodisperse, most pores were within a factor of 1.5 from the mean size (see section 2.2.4). As the pores are templated by ice crystals, these observations suggest that our freezing protocol results in the formation of ice crystals that are approximately uniform in size and that are nucleated in a spatially random manner. We anticipate that this will also hold for ice crystals in the experiments reported here. In accordance with this expectation, optical microscopy on thin (~40-100 μm) samples of dilute latex dispersions, frozen in a cold stage, showed the formation of randomly nucleated ice crystals that had a mono-modal size distribution. Microscopic observations also indicate that the colloidal particles are accumulated at the growing ice-water front. This is consistent with recent calculations[33] and with reported experimental "phase diagram".[34] As the water freezes, both the PEI coated colloids and the di-epoxide cross-linker are concentrated at the boundaries of the ice crystals. We use an excess of

di-epoxide cross-linker to ensure that PEI coated particles that are in contact, are covalently crosslinked. Covalent crosslinking of the PEI proceeds in the frozen state, resulting in the formation of a polymeric mesh around the particles.[41] In the ice templating experiment we do, ice growth velocities are significantly lower than the critical velocity for engulfment[34] of particles. Thus, colloids that are forced into proximity by the ice crystals form bound aggregates, connected by a crosslinked PEI shell. We allow crosslinking to proceed for 12 hours and subsequently, the sample is thawed. If the system is thawed shortly after crystallization (viz. <6 h after ice formation), there is insufficient time for crosslinking and permanent colloidal assemblies do not form. Stable assemblies form only after completion of crosslinking. Formation of the colloidal assemblies is reversible when the freeze-thaw cycles are conducted before the crosslinking proceeds. It is not clear how assemblies organize on repeated thaw–freeze cycles once crosslinked aggregates are formed.

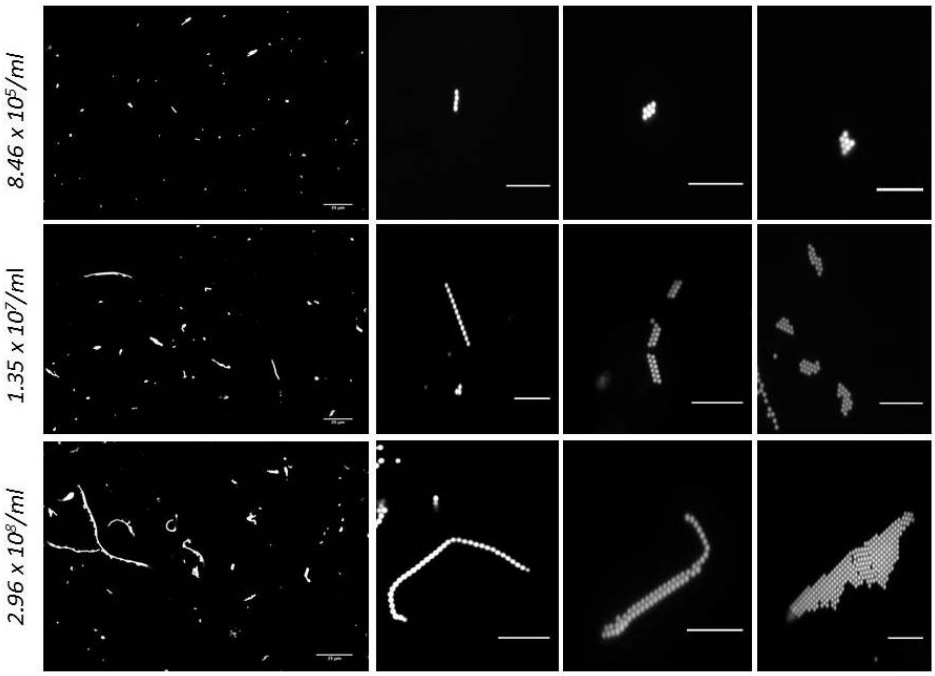

Figure 2-2: Microscopic images of particle aggregates obtained by isotropic ice templating dispersions at particle concentrations of (top horizontal row) 8.46×10^5 particles/ml; (middle horizontal row) 1.35×10^7 particles/ml and (bottom horizontal row) 2.96×10^8 particles/ml. The scale bar for images in the left column is 20 µm and for all other in images, the scale bar is 10 µm.

At the lowest particle concentration (8.46×10^5particles/ml), we observe a large number of "monomers", viz. isolated particles and dimers as well as a few short (~ 4 to 5 particle long)

linear strands and planar aggregates (Figure 2-2, top row). As the concentration increases to 1.35×10^7 particles/ml (Figure 2-2, middle row) and to the highest concentration investigated here, 2.96×10^8 particles/ml (Figure 2-2, last row), we observe the formation of longer linear strands, going up to over 40 particles long as well as elongated planar structures that are 2 particles wide (that we term "tapes") and larger planar structures. Interestingly, for the planar structures, we observe that the mono-dispersity of the colloids drives the formation of locally crystalline structures. Crystalline order has been observed when monodisperse colloidal dispersions undergo gravity-induced sedimentation characterized by small Peclet number ~ O(0.1).[42,43] We estimate the Peclet number (Pe) in our experiments based on the growth rate of ice crystals, v. Thus, Pe = vR/D = 0.23, where R is the colloid size and D is the diffusion coefficient of the colloids, consistent with the observation of colloidal crystals. At all concentrations, we observe the formation of only a small fraction of three dimensional aggregates. The majority of the clusters are organized into planar assemblies. We did not systematically study the influence of particle size on ordering – however, the Peclet number arguments would suggest that less ordered assemblies would result for larger crystal growth rates or larger particle sizes (viz. lower diffusivities).

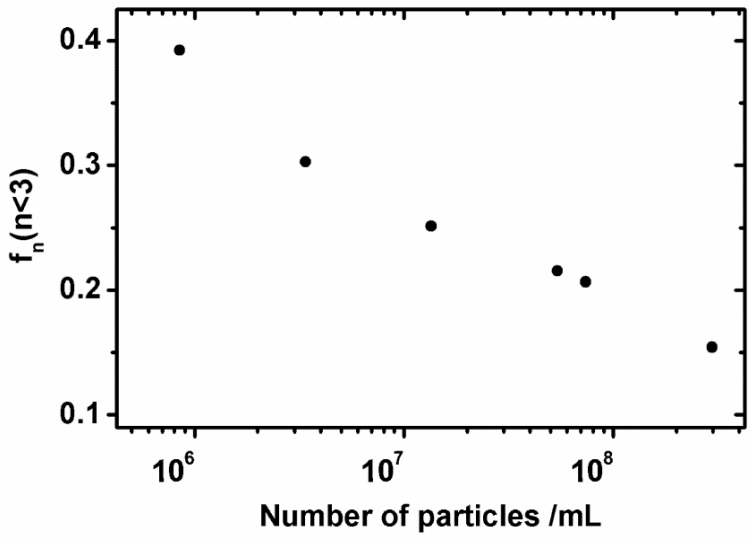

Figure 2-3: Fraction of particles existing as monomers or dimers after isotropic ice templating.

The fraction of particles that form monomers or dimers, $f_n(n < 3)$, is about 0.4 for the lowest concentration (8.46×10^5 particles/ml) and this decreases approximately logarithmically with concentration to about 0.15 at 2.96×10^8particles/ml (Figure 2-3). We term particle aggregates that comprise with n >2 particles as clusters and analyse the cluster size distribution

as a function of the particle concentration in the ice-templated aqueous dispersions. We define P_n as the number fraction of particles in clusters. We observe that at the lowest concentration, ice templating does not result in the formation of clusters larger than about 15 particles (Figure 2-4). However, with increase in concentration, a few clusters larger than 100 particles are observed to form. We note that all the experiments reported here are at concentrations that are significantly below that required for the particles to organize into a percolated network. We observe that, for all the particle concentrations investigated, $P_n \sim n^{-2}$, for clusters comprising $P_n < 30$ particles (Figure 2-4). For larger n, P_n deviates from $P_n \sim n^{-2}$, to exhibit a tail that stretches to increasingly higher n with increase in particle concentration (Figure 2-4), it happens due to the poor statistics.

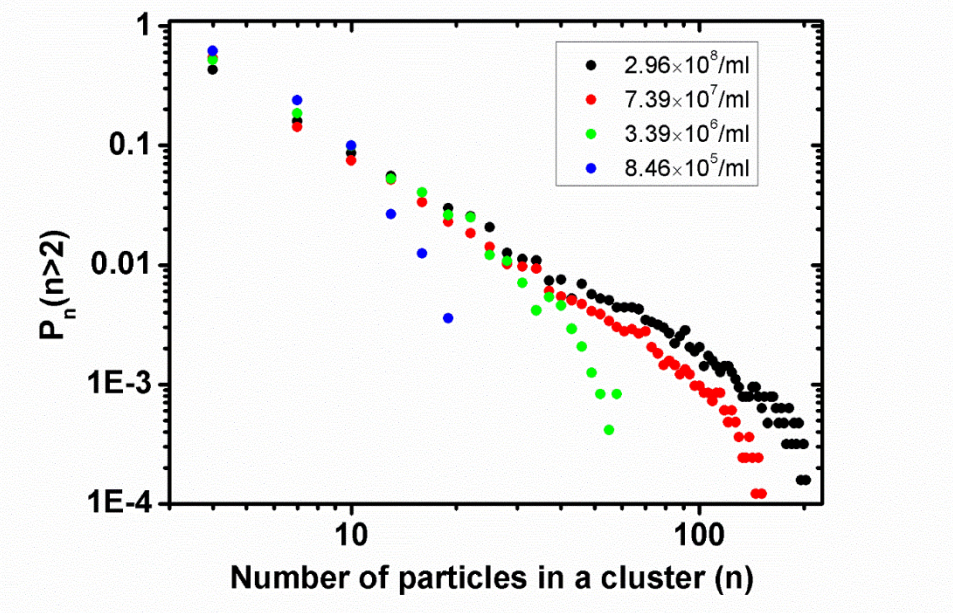

Figure 2-4: Fractional probability of particles forming clusters obtained from isotropic templating. In this process, the distributions is independent with particles concentrations from $3.39 10^6$/mL to $2.96 10^8$mL.

Of particular interest are clusters that are organized as connected linear strings of colloidal particles. Such systems represent colloidal analogues of linear polymers and represent promising models for studying fundamental problems in polymer physics. Therefore, there has been significant interest in realizing such linear architectures.[47-57] We plot the number fraction of particles in linear chains as a function of their size (P_N= number of particles in linear chains of size N/ total number of particles in linear chains). We observe that 99% of the linear chains have a chain length less than 20 and that the number fraction of particles decreases to less than

10^{-3} as N approaches 40 (Figure 2-5). We also observe P_N does not appear to be a very strong function of the colloid concentration in the range of 3.39×10^6 to 2.96×10^8particles/ml.

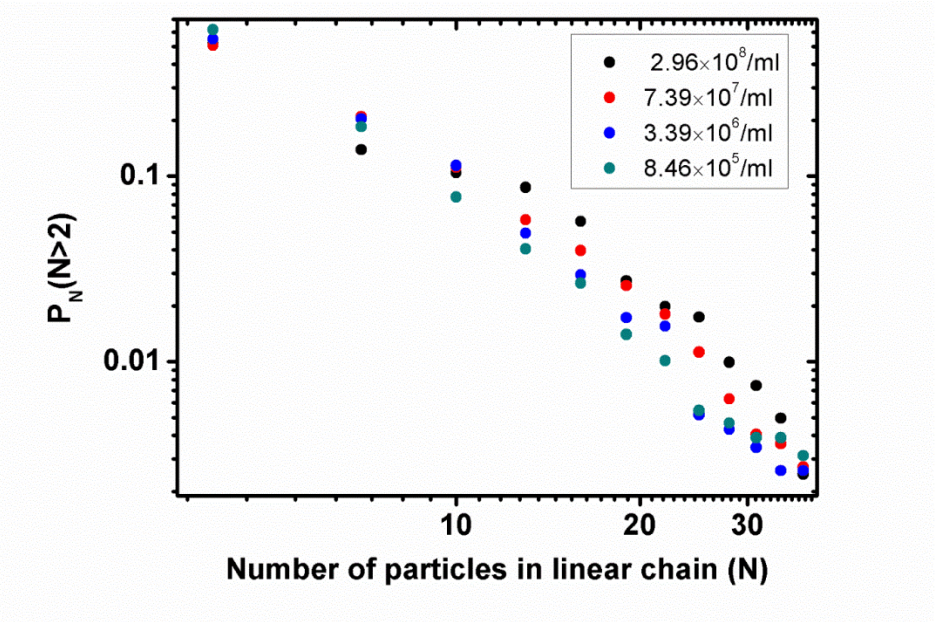

Figure 2-5: probability distribution of particles obtained from linear aggregates (colloidal chains) obtained from isotropic ice templating.

Finally, we examine the effect of particle concentration on the shape of the colloidal clusters, focusing on planar assemblies that comprise the majority of the clusters formed. We define a connectivity parameter for a cluster, C as the ratio of the cluster area to the square of the perimeter, viz. C = Area/(Perimeter)^2 (See section 2.2.3 for the calculation of area and perimeter). An increase in C represents a transition in cluster shape from a linear aggregate towards a circular shape. We calculate the average C at each cluster size, n, for ice templated clusters at various dispersion concentrations (Figure 2-6). It is difficult to attribute much significance to the variation in C with n. For example, it is easy to visualize that the difference in C between a linear chain and an isotropic planar cluster is small for n = 5, relative to that for larger n, say, n = 50. However, at a fixed cluster size, n, it is possible to comment on the relative values of C for clusters prepared starting from different particle concentrations. We note that there is a systematic increase in C with particle concentration for n > 10 (Figure 2-6). This indicates that with increase in concentration from 1.35×10^7 to 7.39×10^7 to 2.96×10^8particles/ml, there is a transition from linear chains to tapes to planar clusters.

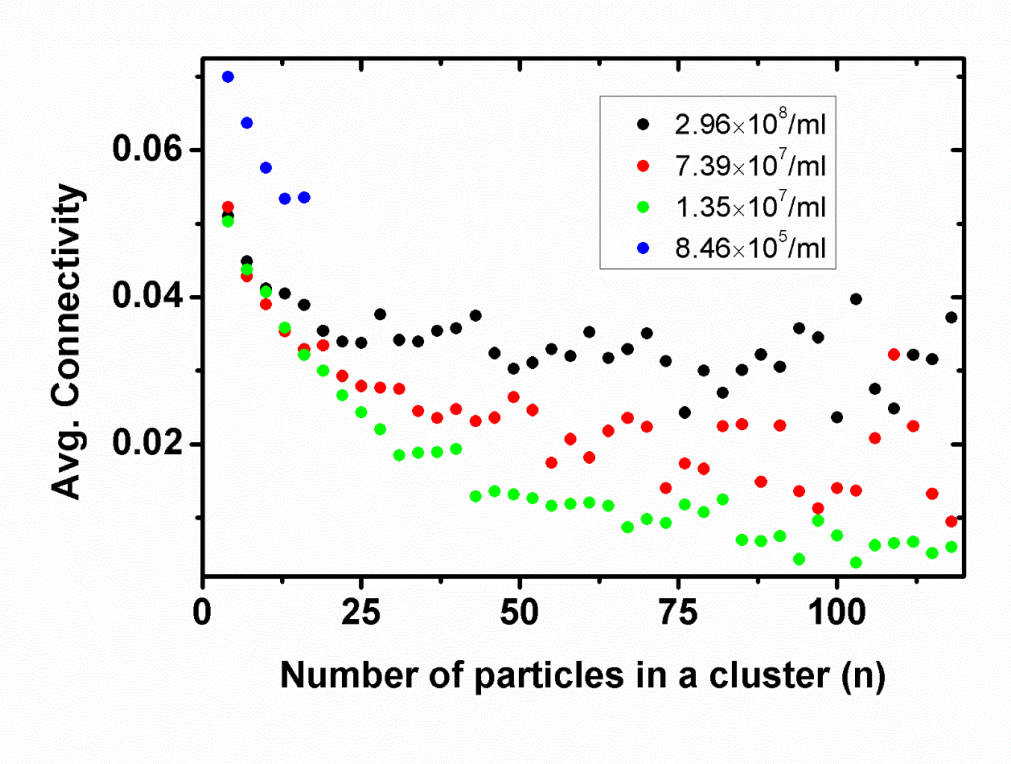

Figure 2-6: Variation in the average connectivity parameter with cluster size for isotropic ice templated systems at different particle concentrations.

It has been reported that elongated anisotropic particles orient parallel to the edge of the templating domain.[55] However, for flexible chains such as those prepared in our current work, it is not clear if alignment of the anisotropic structures will proceed in the same manner. As the ice crystals impinge, colloidal particles are confined to the spaces between the crystals. Therefore, the shape of the colloidal clusters reflect the geometry of the regions where the particles are confined. However, we do not observe confinement effects such as those observed when, say, a polymer chain is confined to a thin film. We note that we obtain qualitatively similar data for the cluster size distribution and the evolution of cluster shape when a dispersion of 1µm silica particles are ice-templated using the same experimental protocol. As the specific gravity for the silica particles (~2) is significantly higher than that for the polystyrene latex (~ 1.05), this indicates that gravitational settling during the freezing process is unimportant in these experiments.

Brownian dynamics simulations are performed to obtain insights into the mechanism of cluster formation in our experiments. A minimal simulation scheme is employed, neglecting hydrodynamic interactions between colloids. Colloidal particles were modelled as hard

spheres, with a diffusion coefficient estimated from the Stokes–Einstein relation for 1 μm colloids diffusing in water. Colloidal particles were allowed to diffuse in all three dimensions. Ice templating simulations are started by placing colloidal particles and ice nuclei, with their centers randomly located in the simulation box. At the start of the simulation, the ice nuclei were treated as point particles with a size of 10^{-3} times that of the colloidal particles. All the ice crystals nucleate at zero time and grow isotropically with a growth rate of 100 nm/s, based on experimental estimates for ice growth in the experiments. The number density of the ice nuclei is chosen to correspond with the average number density of ice crystals in the experiments. During the simulation, if a particle overlaps with another particle during a move, then the move is rejected. In moves where a particle overlaps with an ice crystal, the particle is reflected. If the particle overlaps with an ice particle even after the move is mirrored, the move is rejected. Simulations are stopped when the colloids aggregate, resulting in cessation of Brownian motion.

These simulations incorporate several severe assumptions. Firstly, hydrodynamics is completely neglected in modelling the particle motions. Particles are modelled as hard sphere Brownian colloids with no hydrodynamic interactions. Also, all ice crystals are assumed to nucleate at the initial time with nuclei fixed in space and the ice grows as isotropic, spherical crystals until they spatially overlap. Further, it is assumed that, at the low dispersion concentrations employed in the experiments, growth instabilities of the propagating ice front can be ignored. Finally, it is assumed that the particles experience repulsion when they encounter the growing ice crystals. The simulation is terminated when particles are confined at ice crystal boundaries and when their motions cease. Thus, the simulations model a situation where the only physics that governs particle clustering is their exclusion from growing isotropic ice crystals that are randomly nucleated in space.

Snapshots are presented from the late stages of the simulations, where particle motion has ceased due to the particles being trapped between ice crystals (Figure 2-7). The ice crystals are not shown in these images, so that the particle clusters can be easily visualized. At low particle concentration (10^6particles/ml), most colloids exist as isolated monomeric objects. With increase in particle concentration, small particle clusters emerge (at 10^7 particles/ml) that transition to larger clusters (at 10^8 particles/ml) and finally, several three dimensional structures form at 10^9 particles/ml (Figure 2-7d). Visually, there is a transition from isolated colloids to short linear structures to more isotropic planar aggregates and finally to large three-

dimensional clusters with increase in particle concentration, in qualitative accord with our experimental observations. As in our experiments, local crystalline ordering is observed in the planar aggregates (Figure 2-7). The number of particles that exist as monomers and dimers decreases, approximately logarithmically, with the dispersion concentration, in qualitative accord with our experimental results (Figure 2-3). However, the agreement with experiments is not quantitative, probably due to the large number of simplifying assumptions in the simulations.

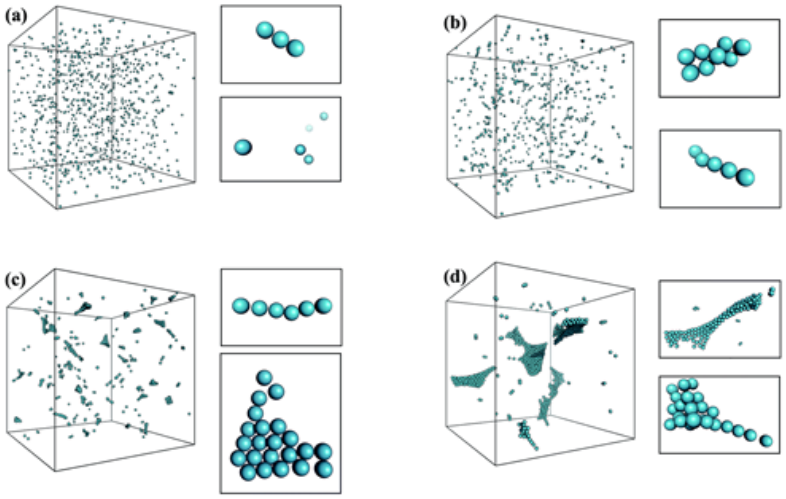

Figure 2-7: Snapshots of the final particle configurations from simulations of isotropic ice templated dispersions at particle concentrations of (a) 10^6particles/ml; (b) 10^7 particles/ml; (c) 10^8 particles/ml and (d) 10^9 particles/ml. Ice crystals are not shown for ease of visualization of the particle clusters. Magnified images of some of the clusters formed are shown on the right.

The distributions (P_n) are obtained for ice template aggregates as a function of number of particles in clusters for different dispersion concentrations. The simulations sample a smaller number of clusters relative to our experiments. Therefore, while we observe the formation of a very small fraction of large colloidal aggregates in our experiments (Figure2-4), these are not observed in the simulations. Remarkably, the simulations show that for small n (< ~20), $P_n \sim n^{-2}$, independent of ice-templated dispersion concentration from 10^7 to 10^9 particles/ml (Figure 2-8). Beyond this power law region, there is a dispersion concentration-dependent deviation in P_n.

Cluster size distributions have been reported to follow a power law in several aggregation processes. When large clusters form by diffusion limited aggregation of clusters, the time dependent cluster size distribution has been observed[56] to follow, $P_n \sim t^{-w} n^{\tau} f(n/t^z)$, where t is the aggregation time and f is a function that asymptotes to 1 at long times. In such diffusion limited cluster aggregation, the power law exponent, $\tau \approx -0.75$. Molecular dynamics (MD) simulations of clustering of Lennard-Jones fluids below the percolation threshold has been reported[57] to give $P_n \sim n^{-2.1\pm0.1}$. For fluids with short range attractive and long range repulsive interactions, the cluster size distribution has been shown[58] to follow a power law distribution similar to that for random percolation, viz. $P_n \sim n^{-2.2}$. Glotzer[59] has reported that the distribution of non-percolated clusters of mobile particles scales as $P_n \sim n^{-1.9}$ as a glass forming Lennard-Jones fluid is cooled. A similar power law exponent ($P_n \sim n^{-1.7}$) has been reported[60] for distribution of crystalline clusters formed in a concentrated dispersion of monodisperse hard spheres. Thus, cluster size distributions that follow a power law, with a power law exponent close to -2 have been observed for a wide variety of particle aggregation processes. It is interesting that a similar behaviour is observed when particles aggregate during ice templating, and that this scaling is independent of concentration over a wide concentration range.

The work of van Dongen and Ernst[61] uses the Smoluchowski coagulation equation to estimate the cluster size distribution for a wide variety of gelling and non-gelling systems. They provide the cluster size distribution in terms of the mean cluster size, s, as $P_n \sim s^{-2} f(\frac{k}{s})$. This does not imply that $P_n \sim n^{-2}$ in all cases. In computer experiments[62] of aggregation of diffusing clusters of particles, it was observed that $P_n \sim t^{-w} n^{-\tau} f(n/t^z)$. This can be written in the alternate form: $P_n \sim n^{-2} g(n/t^z)$. In finite size systems, all the particles aggregate at long times to form one cluster. Therefore, this expression is valid only for an infinitely large system. However, in our experiments, the cluster size distribution is "frozen" when the ice crystals impinge. Therefore, there is no change in cluster size distribution after that time. In the work[62] of Vicsek and Family, $g(x) << 1$ when $x >> 1$, viz. at long times, and $P_n \sim g(x) n^{-2}$. For $x << 1$, $P_n \sim t^{-1.75} n^{-0.75}$, unlike what we observe in our experiments. Therefore, it does not appear that simulations of cluster formation by aggregation of randomly diffusing clusters capture the phenomenology of ice templating. In ice templating, the space available for diffusion of particles shrinks as the ice crystals grow. Brownian dynamics simulations of particle assembly during ice templating suggest that clustering happens only at the late stages of the experiment, when the ice crystals

are close to impinging. Therefore, it is not surprising that these models of aggregation by random diffusion are unable to capture the physics in the ice templating experiments.

The similarity in the trends in P_n obtained from simulations with those from experiments is striking. Similarly, the size distribution of linear colloidal chain P_N, obtained from the simulations is independent of dispersion concentration between 10^6 and 10^9 particles/ml (Figure 2-9), in qualitative accord with our experimental data (compare with Figure 2-5).

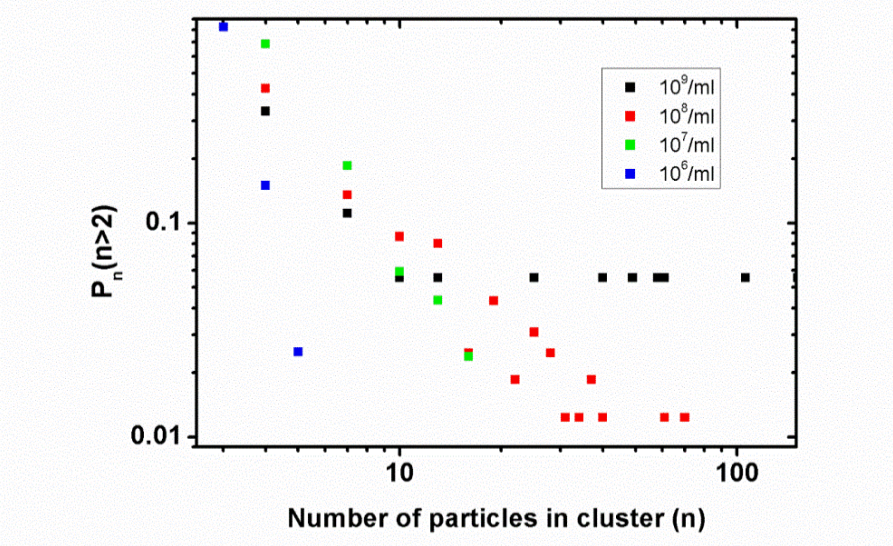

Figure 2-8: Cluster size distribution obtained from isotropic ice templating (simulations).

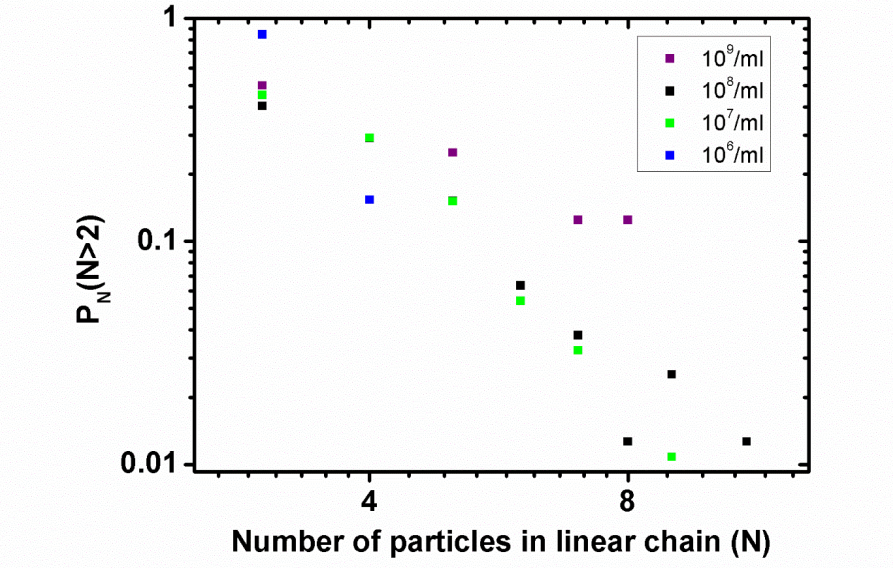

Figure 2-9: Size distribution of linear aggregates obtained from isotropic ice templating (simulations).

Therefore, despite the numerous simplifying assumptions, the simulations are able to accurately capture qualitative trends in the size and shape distribution of particle clusters formed during ice templating. This suggests that, at low concentrations, particle clustering during ice templating is purely kinetic in origin.

2.5 CONCLUSIONS

Ice templating of a very dilute colloidal dispersions (containing ~ 10^6 to ~ 10^8 particles/ml) results in the formation of clusters. At the low concentrations that we use in this work, we do not observe any influence of particle concentration on the nucleation and growth of ice crystal. Therefore, the distribution of cluster sizes and of linear chains reflect how particles are assembled by the (same) underlying ice crystal structure, independent of the particle concentration of the ice templated dispersion. With increase in particle concentration in the ice templated dispersion, the average cluster size increases and there is a transition from linear clusters to two-particle wide "tapes" to more isotropic two-dimensional shapes. We observe relatively few large three-dimensional clusters in this range of particle concentration. In this concentration range, the cluster size distribution exhibits a power law, $P_n \sim n^{-2}$, for clusters containing less than ~ 30 particles, independent of the dispersion concentration. The distribution of linear colloidal clusters is also only weakly dependent on dispersion concentration. Simulations that ignore hydrodynamic interactions between colloidal particles and that model exclusion of particles by randomly nucleated, isotropically growing ice crystals capture the essential features of our experimental observations. This suggests that, for low colloidal concentrations, clustering during ice-templating is purely kinetic in origin.

2.6 REFERENCES

1. Gutiérrez, M. C., Ferrer, M. L. & del Monte, F. Ice-Templated Materials: Sophisticated Structures Exhibiting Enhanced Functionalities Obtained after Unidirectional Freezing and Ice-Segregation-Induced Self-Assembly. *Chem. Mater.* **20**, 634–648 (2008).

2. Deville, S. Freeze-Casting of Porous Ceramics: A Review of Current Achievements and Issues. *Adv. Eng. Mater.* **10**, 155–169 (2008).

3. Li, W. L., Lu, K. & Walz, J. Y. Freeze casting of porous materials: review of critical factors in microstructure evolution. *Int. Mater. Rev.* **57**, 37–60 (2012).

4. Ross, D. N. Homograft replacement of the aortic valve. *lancet* **2**, 487 (1962).

5. Freyman, T., Yannas, I., Science, L. G. P. Cellular materials as porous scaffolds for tissue engineering. *Prog. Mater. Sci.* **46**, 273 (2001).

6. JA Talalay - US Patent 2, 432, 353 & 1947, U. Method of producing reticulated structures. *US Patents* **2**, 432 (1947).

7. Mukai, S., Nishihara, H., Yoshida, T., Carbon, K. T. Morphology of resorcinol–formaldehyde gels obtained through ice-templating. *Carbon* **43**, 1563 (2005).

8. O'Brien, F. J., Harley, B. A., Yannas, I. V. & Gibson, L. Influence of freezing rate on pore structure in freeze-dried collagen-GAG scaffolds. *Biomaterials* **25**, 1077–1086 (2004).

9. Dagalakis, N., Flink, J., Stasikelis, P., Burke, J. F. & Yannas, I. V. Design of an artificial skin. Part III. Control of pore structure. *J. Biomed. Mater. Res.* **14**, 511–528 (1980).

10. Chen, G., Ushida, T. & Tateishi, T. Preparation of poly(l-lactic acid) and poly(dl-lactic-co-glycolic acid) foams by use of ice microparticulates. *Biomaterials* **22**, 2563–2567 (2001).

11. Ho, M. H. *et al.* Preparation of porous scaffolds by using freeze-extraction and freeze-gelation methods. *Biomaterials* **25**, 129–138 (2004).

12. Hsieh, C. Y. *et al.* Analysis of freeze-gelation and cross-linking processes for preparing porous chitosan scaffolds. *Carbohydr. Polym.* **67**, 124–132 (2007).

13. Ricciardi, R., Auriemma, F. & De Rosa, C. Structure and Properties of Poly(vinyl alcohol) Hydrogels Obtained by Freeze/Thaw Techniques. *Macromol. Symp.* **222**, 49–64 (2005).

14. Mahler, W. & Bechtold, M. F. Freeze-formed silica fibres. *Nature* **285**, 27–28 (1980).

15. Mukai, S. R., Nishihara, H., Shichi, S. & Tamon, H. Preparation of Porous TiO_2 Cryogel Fibers through Unidirectional Freezing of Hydrogel Followed by Freeze-Drying. *Chem. Mater.* **16**, 4987–4991 (2004).

16. Nishihara, H. *et al.* Preparation of monolithic SiO_2 - Al_2O_3 cryogels with inter-connected

macropores through ice templating. *J. Mater. Chem.* **16**, 3231–3236 (2006).

17. Mukai, S. R., Nishihara, H. & Tamon, H. Formation of monolithic silica gel microhoneycombs (SMHs) using pseudosteady state growth of microstructural ice crystals. *Chem. Commun.* **7**, 874-875 (2004).

18. Zhang, H. *et al.* Aligned two- and three-dimensional structures by directional freezing of polymers and nanoparticles. *Nat. Mater.* **4**, 787–793 (2005).

19. Munch, E. *et al.* Tough, bio-inspired hybrid materials. *Science* **322**, 1516–20 (2008).

20. Deville, S., Saiz, E., Nalla, R. K. & Tomsia, A. P. Freezing as a path to build complex composites. *Science* **311**, 515–8 (2006).

21. Bouville, F. *et al.* Strong, tough and stiff bioinspired ceramics from brittle constituents. *Nat. Mater.* **13**, 508–514 (2014).

22. Vickery, J. L., Patil, A. J. & Mann, S. Fabrication of Graphene-Polymer Nanocomposites With Higher-Order Three-Dimensional Architectures. *Adv. Mater.* **21**, 2180–2184 (2009).

23. Colard, C. A. L., Cave, R. A., Grossiord, N., Covington, J. A. & Bon, S. A. F. Conducting Nanocomposite Polymer Foams from Ice-Crystal-Templated Assembly of Mixtures of Colloids. *Adv. Mater.* **21**, 2894–2898 (2009).

24. Shi, Q. *et al.* Ice-Templating of Core/Shell Microgel Fibers through 'Bricks-and-Mortar' Assembly. *Adv. Mater.* **19**, 4539–4543 (2007).

25. Vesilind, P. A. & Martel, C. J. Freezing of Water and Wastewater Sludges. *J. Environ. Eng.* **116**, 854–862 (1990).

26. Jackson, K. A. & Chalmers, B. Freezing of Liquids in Porous Media with Special Reference to Frost Heave in Soils. *J. Appl. Phys.* **29**, 1178–1181 (1958).

27. Uhlmann, D. R., Chalmers, B. & Jackson, K. A. Interaction Between Particles and a Solid-Liquid Interface. *J. Appl. Phys.* **35**, 2986–2993 (1964).

28. Cissé, J. & Bolling, G. F. A study of the trapping and rejection of insoluble particles during the freezing of water. *J. Cryst. Growth* **10**, 67–76 (1971).

29. Langer, J. S. Instabilities and pattern formation in crystal growth. *Rev. Mod. Phys.* **52**, 1–28 (1980).

30. Mullins, W. W. & Sekerka, R. F. Stability of a Planar Interface During Solidification of a Dilute Binary Alloy. *J. Appl. Phys.* **35**, 444–451 (1964).

31. Butler, M. F. Instability Formation and Directional Dendritic Growth of Ice Studied by Optical Interferometry. *Cryst. Growth Des.* **1**, 213–223 (2001).

32. Peppin, S. S. L., Elliot, J. A. W. & Woreter, M. G. Solidification of colloidal suspensions. *J. Fluid Mech.* **554**, 147 (2006).

33. Peppin, S. S. L., Wettlaufer, J. S. & Worster, M. G. Experimental Verification of Morphological Instability in Freezing Aqueous Colloidal Suspensions. *Phys. Rev. Lett.* **100**, 238-301 (2008).

34. Deville, S. *et al.* Metastable and unstable cellular solidification of colloidal suspensions. *Nat. Mater.* **8**, 966–972 (2009).

35. Deville, S. *et al.* Influence of Particle Size on Ice Nucleation and Growth During the Ice-Templating Process. *J. Am. Ceram. Soc.* **93**, 2507–2510 (2010).

36. Lasalle, A., Guizard, C., Maire, E., Adrien, J. & Deville, S. Particle redistribution and structural defect development during ice templating. *Acta Mater.* **60**, 4594–4603 (2012).

37. Deville, S., Adrien, J., Maire, E., Scheel, M. & Di Michiel, M. Time-lapse, three-dimensional in situ imaging of ice crystal growth in a colloidal silica suspension. *Acta Mater.* **61**, 2077–2086 (2013).

38. Rajamanickam, R. *et al.* Soft Colloidal Scaffolds Capable of Elastic Recovery after Large Compressive Strains. *Chem. Mater.* **26**, 5161–5168 (2014).

39. Frenkel, D. & Smit, B. *Understanding molecular simulation: from algorithms to applications*. *Elsevier*, **1**, (2001).

40. Sharma, K. P., Ganai, A. K., Gupta, S. Sen & Kumaraswamy, G. Self-Standing Three-Dimensional Networks of Nanoparticles With Controllable Morphology by Dynamic Templating of Surfactant Hexagonal Domains. *Chem. Mater.* **23**, 1448–1455 (2011).

41. Rajamanickam, R. *et al.* Soft Colloidal Scaffolds Capable of Elastic Recovery after Large Compressive Strains. *Chem. Mater.* **26**, 5161–5168 (2014).

42. Holgado, M. *et al.* Electrophoretic Deposition To Control Artificial Opal Growth. *Langmuir* **15**, 4701–4704 (1999).

43. Hoogenboom, J. P., Derks, D., Vergeer, P. & van Blaaderen, A. Stacking faults in colloidal crystals grown by sedimentation. *J. Chem. Phys.* **117**, 11320–11328 (2002).

44. Furst, E. M., Suzuki, C., Fermigier, M. & Gast, A. P. Permanently Linked Monodisperse Paramagnetic Chains. *Langmuir* **14**, 7334–7336 (1998).

45. Hiddessen, A. L., Rodgers, S. D., Weitz, D. A. & Hammer, D. A. Assembly of Binary Colloidal Structures via Specific Biological Adhesion. *Langmuir* **16**, 9744–9753 (2000).

46. Biswal, S. L. & Gast, A. P. Micromixing with Linked Chains of Paramagnetic Particles. *Anal. Chem.* **76**, 6448–6455 (2004).

47. Nie, Z. *et al.* Self-assembly of metal–polymer analogues of amphiphilic triblock copolymers. *Nat. Mater.* **6**, 609–614 (2007).

48. Liu, K. *et al.* Step-Growth Polymerization of Inorganic Nanoparticles. *Science* **329**, 197–200 (2010).

49. Sacanna, S., Irvine, W. T. M., Chaikin, P. M. & Pine, D. J. Lock and key colloids. *Nature* **464**, 575–578 (2010).

50. Li, D., Banon, S. & Biswal, S. L. Bending dynamics of DNA-linked colloidal particle chains. *Soft Matter* **6**, 4197 (2010).

51. Wang, Y. *et al.* Colloids with valence and specific directional bonding. *Nature* **491**, 51–55 (2012).

52. Vutukuri, H. R. *et al.* Colloidal Analogues of Charged and Uncharged Polymer Chains with Tunable Stiffness. *Angew. Chemie Int. Ed.* **51**, 11249–11253 (2012).

53. Bharti, B., Findenegg, G. H. & Velev, O. D. Co-Assembly of Oppositely Charged Particles into Linear Clusters and Chains of Controllable Length. *Sci. Rep.* **2**, 1004 (2012).

54. Bannwarth, M. B. *et al.* Colloidal Polymers with Controlled Sequence and Branching Constructed from Magnetic Field Assembled Nanoparticles. *ACS Nano* **9**, 2720–2728 (2015).

55. Sharma, K. P., Ganai, A. K., Sen, D., Prasad, B. L. V. & Kumaraswamy, G. Exclusion from Hexagonal Mesophase Surfactant Domains Drives End-to-End Enchainment of Rod-Like Particles. *J. Phys. Chem. B* **117**, 12661–12668 (2013).

56. Vicsek, T. & Family, F. Dynamic Scaling for Aggregation of Clusters. *Phys. Rev. Lett.* **52**, 1669–1672 (1984).

57. Heyes, D. M. & Melrose, J. R. Percolation cluster statistics of Lennard-Jones fluids. *Mol. Phys.* **66**, 1057–1074 (1989).

58. Toledano, J. C. F., Sciortino, F. & Zaccarelli, E. Colloidal systems with competing interactions: from an arrested repulsive cluster phase to a gel. *Soft Matter* **5**, 2390 (2009).

59. Glotzer, S. C. Spatially heterogeneous dynamics in liquids: insights from simulation. *J. Non. Cryst. Solids* **274**, 342–355 (2000).

60. Valeriani, C. *et al.* From compact to fractal crystalline clusters in concentrated systems of monodisperse hard spheres. *Soft Matter* **8**, 4960 (2012).

61. van Dongen, P. G. J. & Ernst, M. H. Dynamic Scaling in the Kinetics of Clustering. *Phys. Rev. Lett.* **54**, 1396–1399 (1985).

62. Vicsek, T. & Family, F. Dynamic Scaling for Aggregation of Clusters. *Phys. Rev. Lett.* **52**, 1669–1672 (1984).

Chapter-3

Colloidal Assembly by Directional Ice Templating

The simulations presented in this Chapter were performed by Dr. Mayank Misra and were supervised by Prof. Sanat K. Kumar (Columbia University, New York). Simulation results are presented in this chapter for the sake of completeness.

I also acknowledge Anil Singh Bisht, a summer trainee, who performed some of the experiments in this Chapter, under my supervision.

3.1 INTRODUCTION

Understanding colloidal aggregation is an important problem in the field of colloidal physics, and has been extensively investigated over the last four decades.[1,2] Experimentally it has been reported that colloidal particles can assemble into various structures such as regular clusters,[3] chiral colloidal structures[4] and as well as fractal structures.[5,6] There are numerous routes to assembling colloidal particles,[7–11] and newer techniques for controlling colloidal assembly are under investigation currently. The rich literature on colloidal aggregation has motivated many new experiments, computer simulations, and theories. Often, it is observed that the cluster size distribution during colloidal aggregation follows a power law, with the power law exponent determined by the route to aggregation.[12] The use of scaling concepts[13] has provided deep insights into the aggregation process, specifically, the kinetics of aggregation and into the

structure of the colloidal aggregates that are formed. Two distinct regimes of colloidal aggregation (diffusion limited colloidal aggregation and reaction limited colloidal aggregation) have been studied experimentally, theoretically and by simulations. [6,14,15]

Ice-templating or ice segregation-induced self-assembly (ISISA) is a technique that relies on the solidification of water in a well dispersed particle suspension or slurry.[16,17] In this process, an aqueous solution or dispersion is frozen so that ice crystals expel the solutes or dispersed particles that are then localized between the ice crystals. Thus, the growth of ice crystals in the suspension spatially redistributes the suspended particles. After complete freezing/solidification, removal of ice (typically by freeze drying) results in the formation of porous materials[18,19] where the pores are the negative replica of the ice crystals. Typically, the size of the pores varies from 10-100 μm. Thus, the shape of the pores can be varied by controlling the freezing of the dispersions. In isotropic freezing, ice crystals are nucleated randomly in the dispersion and grow isotropically. Thus, they grow out with spherical symmetry and deform when they impinge.[20] However, when the dispersions are subjected to directional freezing, this results in the formation of porous structures with highly anisotropic pores.[21–24]

Here, we investigate colloidal assembly of dilute colloidal dispersions by directional ice templating, at colloid concentrations that are far below that for percolation. Similar to our previous studies of isotropic ice templating (Chapter 2), here too we observe that the colloidal assemblies that form exhibit a progression from isolated particles to linear chains to two particle wide "tapes" to 2D sheet structures and finally to three dimensional aggregates. We also investigate the probability distribution (P_n) of clusters containing n particles, and find that P_n (for n>2) is a strong function of the dispersion concentration. Specifically, P_n exhibits a power law behaviour, $P_n \sim n^{-\eta}$, where η varies from 2.27 (for particle concentrations $\sim 10^9$ particles/mL) to 3.19 (for low particle concentrations, $\sim 10^7$ particles/mL). We rationalize these results based on lattice simulations.

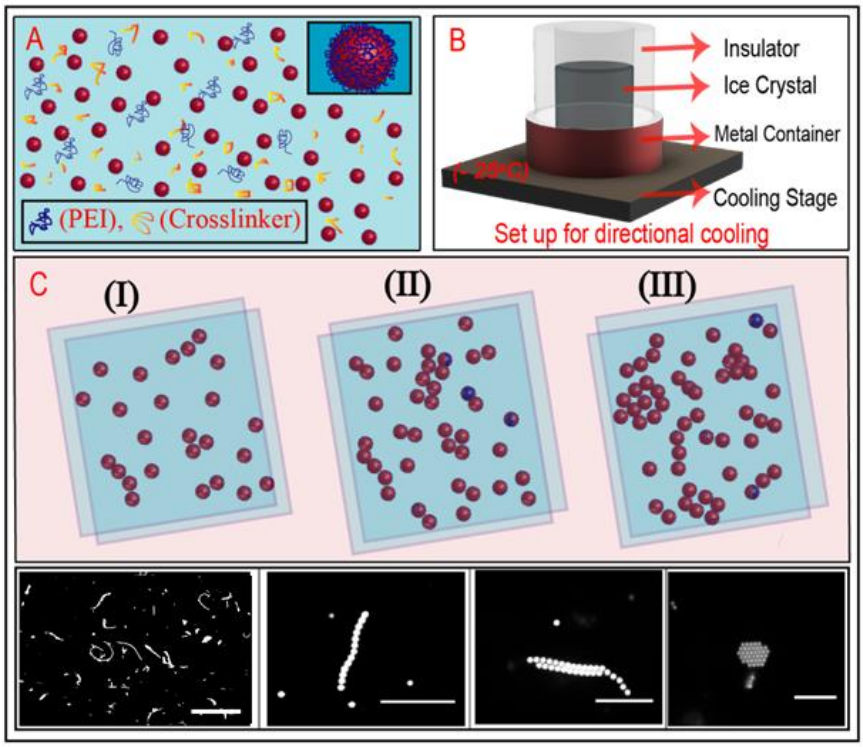

Figure 3-1: Schematic of the directional ice templating process. (A) Dispersed PEI coated PS particles and cross-linker. (B) Directional cooling set up. The temperature at the lower plate is -25^0C. Aqueous colloidal dispersions are taken in a tube that is placed in contact with the lower plate. The lateral sides of the tube are insulated so that the temperature front propagates directionally. (C) Due to the temperature gradient in the set-up, the freezing front propagates from the bottom surface and ice crystals grow directionally. As the ice crystals grow and impinge, colloidal particles ae trapped between the ice crystals. (Lower panel) fluorescence microscopy images of particle assemblies formed during directional ice templating. Scale bar for the 1st image from left side is 30 μm. The scale bar for the magnified images of individual aggregates on the right is 10μm.

3.2 MATERIALS AND METHODS

3.2.1 MATERIALS USED

Poly(ethylene imine), PEI (supplier specified, M_W~75000 kDa) and polyethylene-glycol di-epoxide (PEG-di-epoxide, supplier specified M_n = 500 g/mol) were obtained from Sigma-Aldrich and were used as received. Fluorescent (Rh-B) dyed polystyrene beads (PS), diameter 1.08 μm with polydispersity 4% were obtained from Microparticles GmbH, Germany and were used as received. The PS particles were supplied as aqueous dispersions with a concentration

of 2.5 w.v %. Deionized (DI) water from a Millipore set-up with pH=7 and resistivity=18MΩ.cm was used in all experiments.

3.2.2 SAMPLE PREPARATION

1 μL of PS latex suspension (containing~4.8×10^7particles) was taken in 200 μL DI water and sonicated for a minute to disperse the particles well. 10 μL of PEI solution (stock solution of 100 mg/mL) was diluted in 200 μL of DI water. The PS latex dispersion was added to the PEI solution with continuous vortexing. Vortexing was continued for 5 minutes to allow uniform adsorption of PEI on the PS (PEI@PS). After that we centrifuged the sample at 4000 rpm for 8 minutes and removed about 75 % of the supernatant with care, so there is only minimal loss of PS particles. We diluted this dispersion with ~200 μL DI water, followed by sonication for a minute and vortexing for 2 minutes to ensure that the particles are well dispersed. 4 μL of PEG crosslinker was diluted in 96 μL of DI water, vortexed for two minutes and then added to the PEI@PS dispersion with continuous vortexing. We continue to vortex for another two minutes to ensure that the sample remains well dispersed. After that we transfer this dispersion to the directional cooling stage (Figure 3-1B). We fix the stage temperature at -25^{o}C and allow the dispersion to freeze. Within 30-35 minutes the entire sample freezes to form ice. The frozen sample is then maintained at -18^{o}C and cross-linking is allowed to proceed for more than 12 hrs. Finally, we thaw the sample at room temperature for 30 minutes and load it into a cavity glass slide. The sample is sealed with a cover slip using nail polish. The sample is held in the cavity slide and the colloidal clusters are allowed to sediment on the cover slip over an hour. These clusters are then imaged using fluorescence microscopy. We used the same protocol to prepare samples at different concentrations, ranging from ~10^7 to ~10^9 per mL.

3.2.3 DESCRIPTION OF DIRECTIONAL ICE-TEMPLATING

We have designed and constructed a directional cooling chamber schematically represented in Figure 3-1B. The lower surface is maintained at -25^{o}C while the upper surface is at ambient temperature. To ensure that the temperature gradient is unidirectional, we use a 2.5 mm thick Teflon insulator between the sides of the sample tube and the outer metal. Thus, heat conduction is only along the axis of the container and heat transfer from the sides is minimized. We term this the directional cooling (DC) chamber. We pre-cool 500 μL of PEI coated colloidal suspension mixed with excess cross-linker to 0^{o}C. Excess crosslinker is used to ensure that once a particle aggregate forms, it is irreversibly bonded. We hold this system isothermal for

15 minutes and then transfer to the DC chamber. We cut the lower part of the sample tube so that the dispersion is in direct contact with the metal bottom plate. We ensure that the sample is well sealed so that there is no leakage and that heat conduction is predominantly unidirectional (in the vertical direction). We estimate the average propagation rate for ice growth as ~O (1 μm/s), based on the time for complete freezing of the sample. We (and others[22]) have observed that colloidal particles, such as the 1 micron colloids used in this experiment, are expelled to the ice crystal boundary. Due to the low-temperature (-25^{o}C) at the bottom surface, ice crystals start growing vertically from the metal surface and expel PEI coated PS particles, unadsorbed PEI and cross-linker to the ice crystal boundary. After freezing is completed, we maintain the frozen system in a refrigerator at -18^{o}C. Crosslinking reaction happens in the frozen state for more than 12 hrs. Finally, we thaw the sample, harvest the particles and clusters and image using fluorescence microscopy.

We use an indirect method to visualize the ice crystal size, shape and orientation. We increase the amount of polymer and crosslinker added and perform directional ice-templating using the aforementioned protocol. Use of a higher quantity of polymer and crosslinker results in the formation of a self-standing macro-porous scaffold.[20,25] The pores in the scaffold represent a negative replica of the ice crystals. Thus, quantifying the number density, shape and orientation of the pores in the scaffold gives us insights into the ice crystals that templated them. For scaffolds prepared using directional ice templating, we observe the formation of elongated pores oriented along the axis of the sample, viz. along the direction of propagation of the freezing front. The width of these pores are ~30μm (Figure 3-2). An SEM image of the porous scaffolds prepared using directional ice templating are shown in Figure 3-2A. We also present scaffolds prepared using isotropic freezing and present a SEM image for the resultant scaffold in Figure 3-2B.

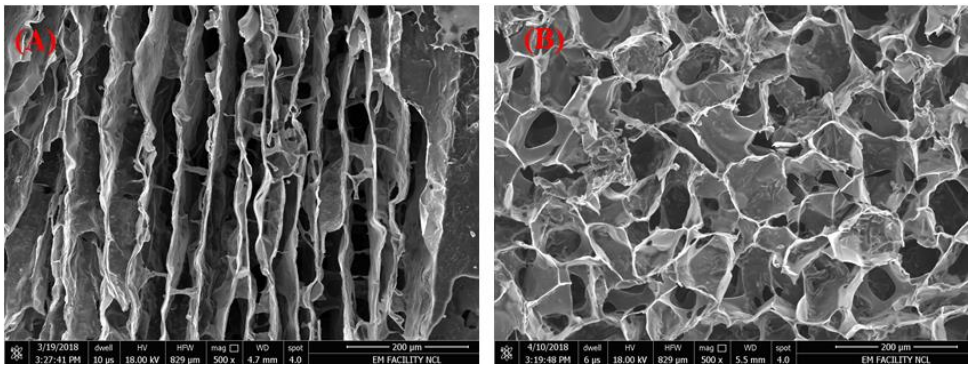

Figure 3-2: SEM image of scaffold made with excess amount of polymer using (A) directional ice-templating and (B) isotropic ice templating. The voids represent a negative replica of the ice crystal templates.

3.2.4 IMAGING AND TOOLS FOR DATA ANALYSIS

Laser scanning fluorescence microscope (Carl Zeiss Axio observer Z1) was used to perform imaging and we used a 63x objective (NA = 1.4 and WD = 0.19 mm). We capture more than 200 images at each concentration. To analyse the images, we use ImageJ. At first, we subtract a constant value (= 50, for the background) and then convert the images into 1bit (binary) and use the in-built Analyze Particles function to obtain the area and perimeters of particle clusters.

(Weblink for ImageJ-https://imagej.nih.gov/ij/download.html).

3.3 SIMULATION DETAILS

3.3.1 DETAILS OF DIRECTIONAL COOLING

Lattice simulations are used to delineate the physics behind colloidal assembly seen in the experiments. The orthorhombic simulation box is constituted as a 3-D lattice, where the edge length of the grid cube is equivalent to the colloidal particle diameter (1μm). The inherent assumption of this lattice simulation, where the smallest size probed is equal to 1μm, is that the formation of ice crystals does not affect particle clustering until their sizes are comparable. If the ice crystal size is smaller than 1μm, it does not play any role and anything smaller than 1μm is considered as invisible. To model directional cooling, ice nucleation is initiated at the bottom surface (XY--plane), hence periodic boundary conditions exist only in X and Y--directions. The simulation can be divided into four steps; (i) Initial seed structure generation, (ii) Ice crystal growth, (iii) Attraction mesh generation, and (iv) Colloidal particle movement.

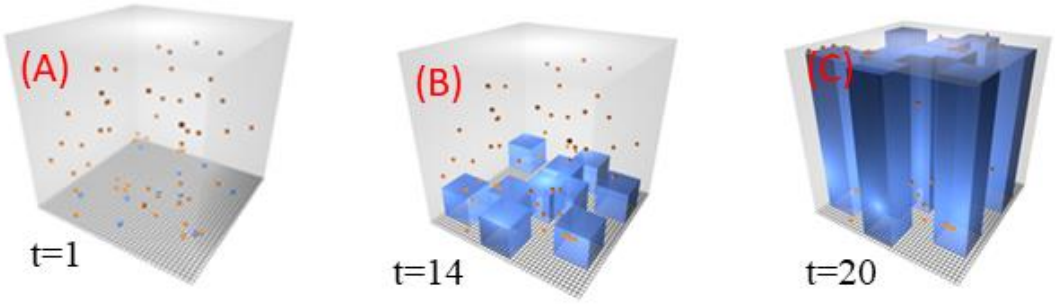

Figure 3-3: Schematic of simulation. The initial seed structure is generated by randomly placing ice seed nuclei on the bottom XY--plane and colloidal particles in the 3-D space above

it. The ice is allowed to grow uniformly in X, Y and Z directions until the entire box is filled with ice. In the process of crystal growth the colloidal particles are swept by the ice growth front, leading to cluster formation. The final structure obtained in the simulation is used for cluster analysis. (A-C) Ice crystal growth as time progress. The ice seed and particle concentration is kept low in the illustration for ease of visualization.

(i) The ice nuclei are randomly distributed on the XY--plane with the condition that two nuclei cannot occupy the same lattice point. After assigning the ice nucleation sites, lattice sites are selected randomly for the colloidal particles. Note that these sites are a pseudo representation of the time step when the colloidal particles get trapped on the ice growth front. The simulation does not describe the dynamics of this entrapment, and we argue that it plays no role in case of small molecules like water. The size of the box, number of ice seeds, and particles vary depending on the particle concentration and are shown in Table 3-1.This setup acts as the initial seed for the simulation.

(ii) Directional cooling is implemented by allowing the cubic crystal to grow uniformly in X, Y, and Y--directions. The isotropic growth continues until the ice edge length is 50, as seen in the experiments. The ice seed concentration is kept such that incompressibility limit for ice crystals is achieved at this step, viz. all the lattice points are occupied either by ice or particles. Since the mean ice crystal size is fixed we change the nucleation density of ice seeds to fill the simulation box completely when the maximum size of the ice crystal is achieved. After this step, the ice crystal is allowed to grow only in Z--direction, until the height of the ice crystal reaches the box length. Another growth mechanism was tested, where the growth of the cube is anisotropic, and ice crystal growth is faster in Z--direction compared to X and Y--direction. The growth rate is dependent on the box size and is in the ratio of 1:1:(box_{edge}/50), where box_{edge} is the length of the simulation box in the Z--direction. The ice seed concentration used is same as for the other flavour of crystal growth simulation. Note that the growth rate is dependent on the box length, and changing the box size will lead to change in initial seed concentration to avoid box--size effects. Both flavours of crystal growth simulation yield similar results. The anisotropic growth is the better representation of directional cooling, however, due to the additional complexity of box size effects, we focus on the isotropic growth simulation.

(iii) An attraction mesh for the simulation box is generated and updated every step (ice-growth and particle move). To generate the attraction mesh, each lattice site is assigned an attraction

quantity, ε. If lattice site is occupied by ice crystal or particle then ε=0, else ε=1. To account for particle-particle attraction, we do the following. For every unoccupied lattice (ε=1), number of adjacent particles are counted n_j, and a new ε is assigned, where $\varepsilon_{new}=\varepsilon_{old}+n_j$. For example, an unoccupied lattice next to two particles will have ε=3. This allows us to mimic particle-particle depletion attraction and ensures a cluster once formed, does not break.

(iv) At every step (lattice) growth of ice crystal, a check is performed to check for overlap of colloidal particles. If a particle is found to be overlapping the ice crystal and is not stuck (as defined formally later in this paragraph), a particle move is initiated. For a particle overlapping ice and that is not stuck on the lattice, the distance to all other lattice points is calculated (d_{ij}). ε_j/d_{ij} is calculated for all lattice sites corresponding to i^{th} lattice. The lattice with maximum ε_j/d_{ij} is selected and the particle moves from i^{th} to j^{th} site. This can lead to degenerate results. To address this, we assign priority based on larger ε_j followed by lower d_{ij}. If multiple possible sites still exist (though, practically this is only rarely observed), a random site among the possible favourable moves is chosen. There is one more restriction imposed in the simulation, where the particle never moves and is considered to be stuck. If $\varepsilon_j/d_{ij} < 1/L_{ice}$, where L_{ice} is the length of ice crystal in X or Y--direction at that instantaneous step, then the particle is considered stuck and does not move for the rest of the simulation. This phenomenon is seen when two ice growth fronts approach each other and the particle is trapped between them and is also unable to move in the Z--direction.

Concentration of particles (1/mL)	Particles	Box length	Ice Seeds
9.0E+06	1000	485	162
3.0E+07	1000	335	112
1.0E+08	1000	216	72
1.0E+09	5000	171	53
9.8E+09	5000	80	32

Table 3-1: Details of the simulation set up for directional ice templating.

3.3.2 DETAILS OF ISOTROPIC COOLING

We keep the simulation box same as directional and instead of random ice seeds at the lower surfaces of the box, ice seeds are randomly distributed in the box. The ice crystals grow spherically until all the lattice sites are occupied. We choose ice nucleation density such that

the incompressibility limit is reached when the average ice crystal size is ~50μm, to accord with the experiment. Details of the simulation for isotropic cooling are shown in Table 3-2.

Concentration of particles (1/mL)	Particles	Box length	Ice Seeds
1.00E+07	1000	384	6658
1.00E+08	950	178	1062
1.00E+09	995	83	138

Table 3-2: Details of the simulation set up for isotropic ice templating.

3.3.3 DEFINITION OF VOIDS

Isotropic freezing: Lattice points surrounded by ice crystals are identified as a void. Voids can be both inner voids (void 1 in left panel, Figure 3-4) or outer voids (void 2 in left panel, Figure 3-4).

Directional freezing: As the ice crystals grow vertically from the lower surface, the freezing front height grows with time. We define voids only in the region of the sample below the top surface of the ice crystals at each time step. Similar to isotropic cooling we define a void as lattice points surrounded by ice crystals (right panel, Figure 3-4).

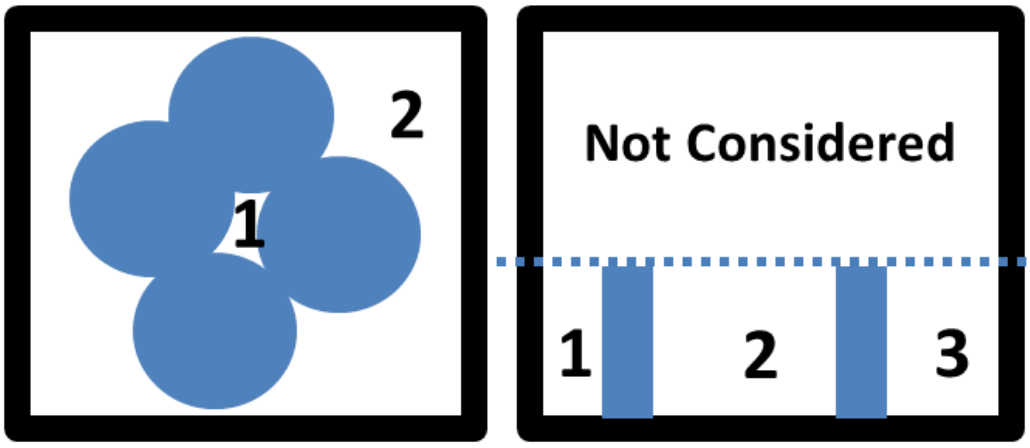

Figure 3-4: Schematic representation of voids for (left) isotropic and (right) directional freezing simulations.

3.4 RESULTS AND DISCUSSIONS

3.4.1 EXPERIMENTAL

Directional ice templating is performed for samples with different concentrations of PS colloids (10^7 to 10^9 particles/mL), far below from the percolation limit (details in subsection 3.2.3).

We harvest the particle clusters after completion of ice templating and observe the formation of linear chains, two particle-wide tapes and sheets (Figure 3-1, lower panel). Since the PS colloids used in these experiments are monodisperse in size, we observe crystalline organization locally in the planar assemblies. At all concentrations, we observe that some 3D clusters form along with planar assemblies (Figure 3-1, lower panel). It takes ~35 minutes to freeze the entire sample in the experiment, yielding an average ice front growth velocity ~O(1 μm/s), assuming uniform growth of the ice crystals. At this velocity, literature suggests that solutes are rejected at the ice crystal growth front.[22]

At low colloid concentration (~10^7 / mL), most particles do not form clusters and remain as isolated particles or as dimers. At these concentrations, there are very few short linear chains, tapes or planar aggregates. With increase in particle concentration from 10^7 to ~10^9 /mL, we observe the formation of long linear structures (comprising over 25 colloids) as well as more extended two-particle wide tapes and large planar structures. We note that, at lower concentration (~10^7 /mL), nearly 80% of the particles exist as monomers or dimers. This reduces, approximately logarithmically with concentration, decreasing to 45% at a concentration of ~10^9 / mL (Figure 3-5). This trend is qualitatively similar to the case of ice templating by isotropic freezing.

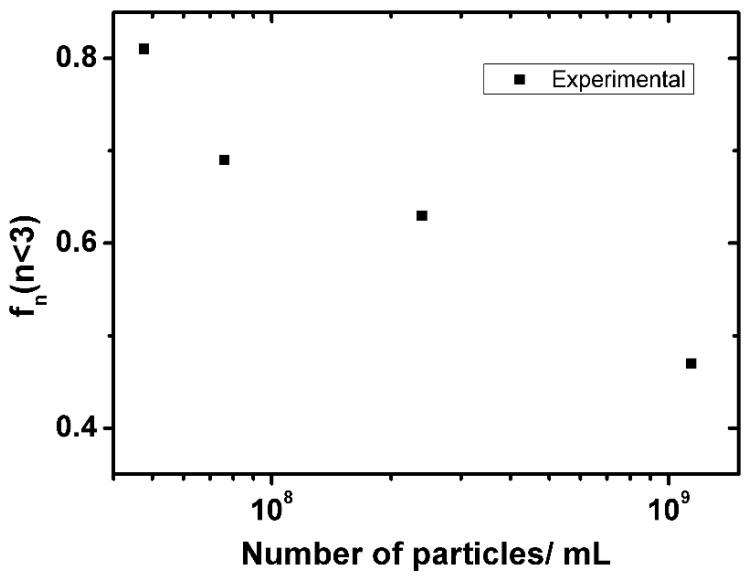

Figure 3-5: Fraction of particles that exist as monomers or dimers. With the increasing particle concentrations the numbers of existing monomers and dimers decrease approximately logarithmically.

We define clusters as particle aggregates comprising n > 2 particles. We analyse the probability distribution (P_n) of particles as a function of cluster size for different concentrations of colloidal particles. We observed that for the lowest concentration (4.8×10^7 /mL), the cluster sizes observed are relatively small (n<20) and this increases for higher concentration (Figure 3-6). At higher concentration (~10^9 / mL) we observed some clusters with n~50 particles and a few 3D clusters. We note that all the concentrations reported here are far below that required for particles to assemble into a sample-spanning percolated structure. We observe that $P_n \sim n^{-\eta}$, where η is strongly dependent on the particle concentration. This is in contrast to the case of isotropic ice templating where η = 2, independent of particle concentration. Specifically, in the case of directional templating, the exponent η varies from 3.19 for lower particle concentrations (~10^7 particles /mL) to 2.27 for higher particle concentration (~10^9 particles /mL).

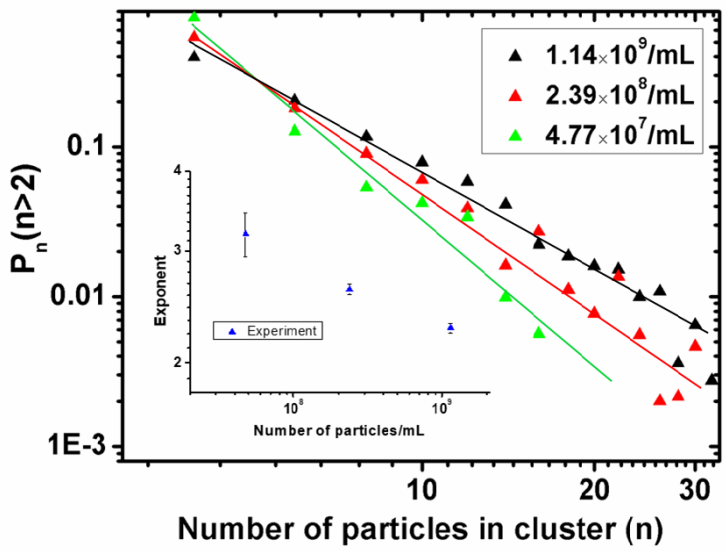

Figure 3-6: Probability distribution for cluster formation by particles during directional ice templating. In the inset, we show the power law exponent obtained from a fit to the probability distribution. The error bars are based on the errors in fitting the data.

We analyse how the shape of the particle clusters change with particle concentration. We define connectivity for a cluster as the ratio of the area of the cluster to the square of the cluster perimeter, viz C= (Area)/(Perimeter)^2, a dimensionless number. For a cluster with the same number of particles, an increased value of C indicates a transition in shape from a linear structure to a more isotropic shape. We estimate the average connectivity at a particular concentration and plot as a function of cluster size for different concentrations. We observe that the average value of C is higher at higher particle concentration (Figure 3-7), which

indicates the formation of isotropic planar clusters at higher concentration. We note that for larger clusters (viz. n > 10), there is an increase of average C with concentration.

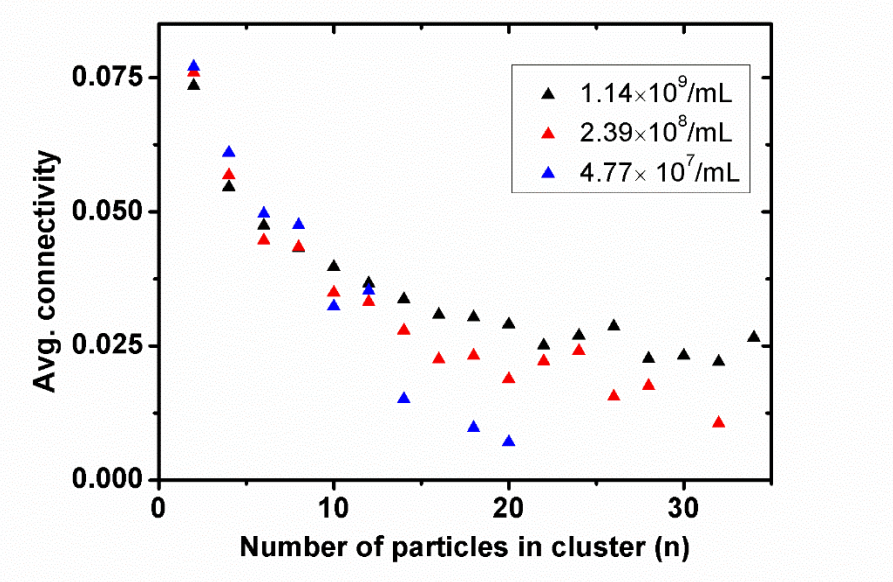

Figure 3-7: Variation in the average connectivity with cluster size.

3.4.2 SIMULATIONS

Our collaborators use a lattice simulation model that represents the ice templating process in a simplified manner. In the simulations, particles are excluded by the ice crystals and there is an attractive inter particle interaction that ensures that once particles form a cluster, they never debond.

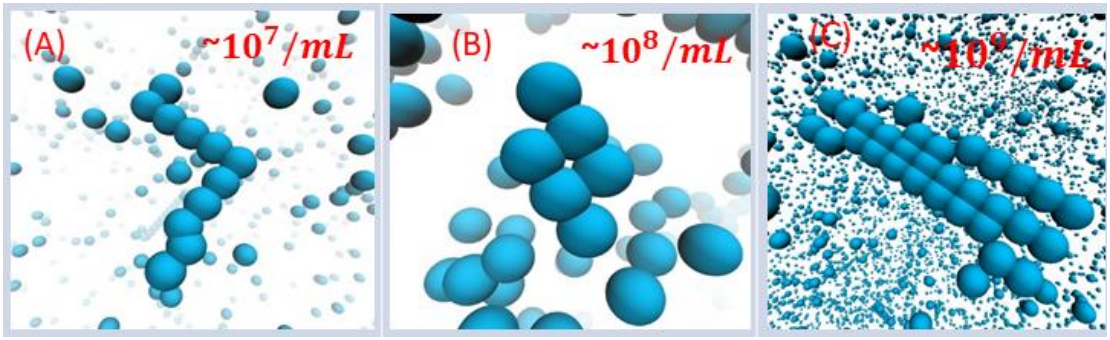

Figure 3-8: Representative snapshots of the final particle configurations from directional ice templating simulations at particle concentrations of (A) $\sim 10^7$/mL (B) $\sim 10^8$/mL (C) 10^9/mL.

Snapshots of colloidal aggregation observed in the final stages of the simulations, when particles are trapped by the ice crystals, are presented in Figure 3-8. For ease of visualization, the ice crystals are not shown in the images. At low particle concentration ($\sim 10^7$/mL) most

particles exist in isolation or as dimers. With increasing particle concentration, larger clusters form and we observe a few 3D clusters as well. These qualitative observations are in good accord with our experimental results. The number fraction of monomer and dimers decreases approximately logarithmically with the particle concentration, again in qualitative and quantitative accord with experimental results (Figure 3-9, compare with the experimental result Figure 3-5).

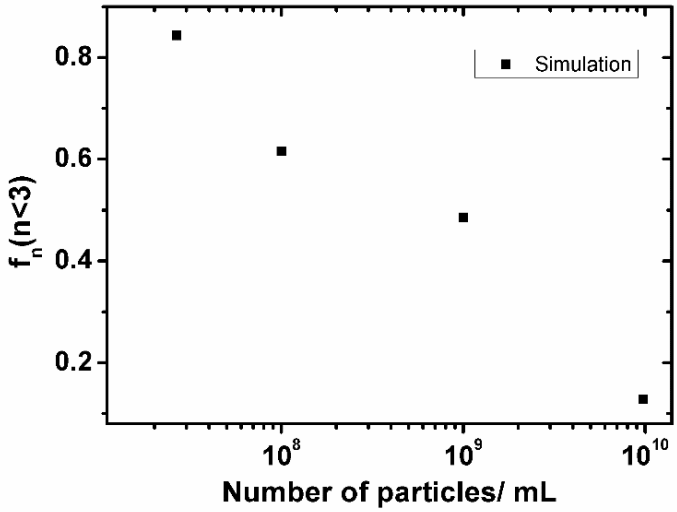

Figure 3-9: Fraction of particles existing as monomers or dimers in simulations of directional ice-templating.

We obtain the probability distribution (P_n) of particles assembled in clusters of size n from simulations at different particle concentrations. In the simulations too, the cluster size distribution follows a power law as $P_n \sim n^{-\eta}$, where η is strongly dependent on the particle concentration (Figure 3-10, compare with the experimental result in Figure 3-6). The exponent η varies from 3.68 for particle concentrations $\sim 10^6$ particles /mL to 2.16 for particle concentrations of 10^{10} particles /mL.

In several aggregation processes, a power law distribution for cluster sizes has been observed. In the diffusion-limited aggregation process, it has been observed that the time-dependent cluster size distribution[26] exhibits a power law form.[12] It has been reported[27] that for fluids with short-range attractive and long-range repulsive interactions, the cluster size distribution follows $P_n \sim n^{-2.2}$. With increasing concentration, monodisperse colloidal hard spheres form crystalline clusters with a size distribution[28] of the form $P_n \sim n^{-1.7}$. It has been reported[29] that Lennard-Jones fluids below the percolation limit obey $P_n \sim n^{-2.1\pm0.1}$. van Dogen and Ernst[30] used

Smoluchowski's equation to estimate the cluster size distribution as $P_n(t) \sim s^{-2} f\left(\frac{n}{s}\right)$. Therefore, while a power law distribution for the cluster size is not unusual, the power law exponent is determined by the aggregation process.

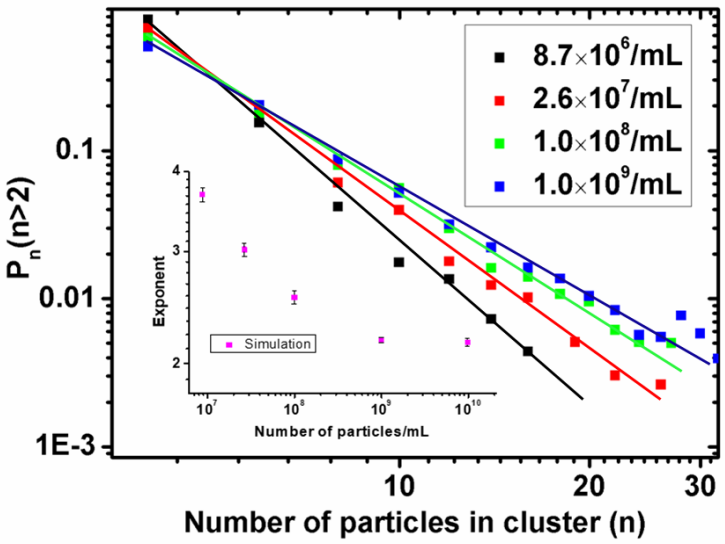

Figure 3-10: The probability distribution (P_n) obtained from simulations of directional ice templating. We fit the distribution with a power law and extract the exponent (plotted in the inset). Error bars represent the error in fitting P_n.

We analyse the average connectivity of assembled structures obtained from the simulations. Similar to the experimental results (Figure 3-7), we observe that the average connectivity of the clusters increases with concentration (Figure 3-11). The results indicate there is a transition from linear chains at lower concentrations to planar structures with increase in concentration. We don't have clear understanding of the quantitative deviation of connectivity from the experimental results (compare Figure 3-11&Figure 3-7). However, there is qualitative agreement in the trends observed in experiments with the simulation results.

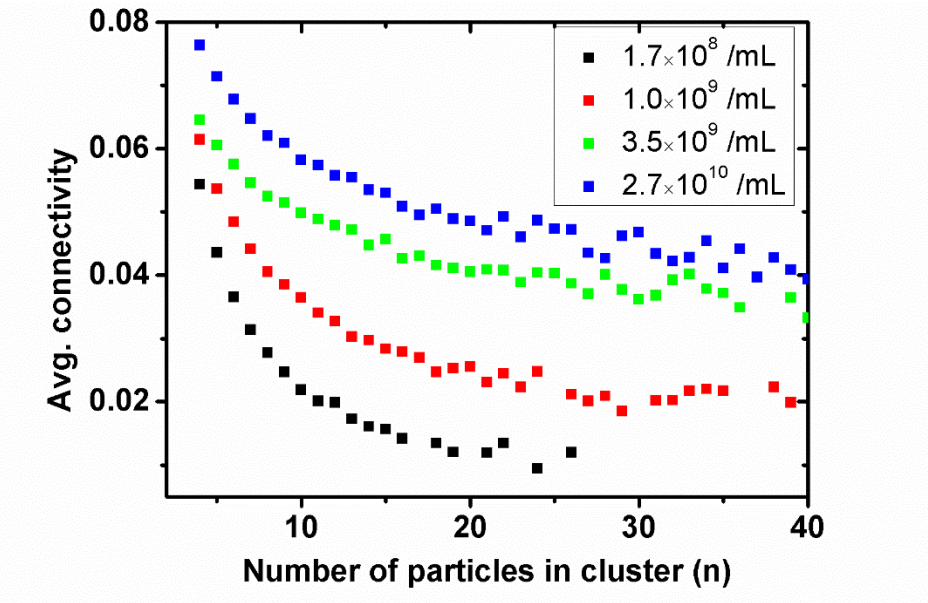

Figure 3-11: Variation in the average connectivity with particle concentration.

3.5 HOW DOES DIRECTIONAL ICE-TEMPATING GIVE RISE TO THE OBSERVED CLUSTER SIZE DISTRIBUTION?

Isotropic freezing and directional ice templating differ in the geometry of ice crystal growth: while randomly nucleated ice crystals grow isotropically in the bulk for isotropic freezing, directional ice templating is characterized by vertical growth of ice crystals. In general, the nucleation density increases and the average ice crystal size decreases with increase in cooling rate.[31] As the ice crystals grow and eventually impinge, colloidal particles are expelled from the ice crystal and assemble at the boundaries of ice crystals.

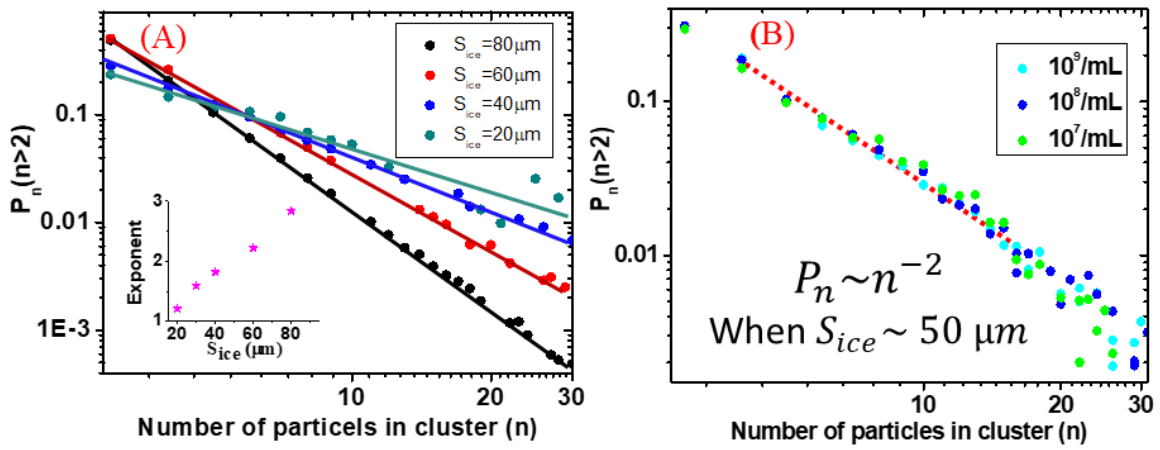

Figure 3-12: Cluster size distribution from simulations of isotropic freezing yields a concentration independent power law with an exponent of -2.

In simulations of isotropic freezing under conditions representative of the experiments, we observe that the cluster size distribution is concentration independent, and follows $P_n \sim n^{-2}$, consistent with our experimental findings (Chapter-2). For isotropic templating, we investigate the effect of ice crystal size on cluster size distribution by varying the ice crystal size from 20 µm to 80 µm for a concentration of 10^8 particles/mL (Figure 3-12A). The cluster size distribution is given by a power law and we show the variation in the power law exponent with ice crystal size in the inset of Figure 3-12A. It is clear that probability distribution of particles in clusters is a function of ice crystal size. Previously, we observed that probability distribution of particles in clusters are independent with a wide range of colloidal suspensions from 3.39×10^6 to 2.96×10^8 particles/mL (Chapter-2). Here, our collaborator performed simulations with mean ice crystal size ~50 µm, and obtained the same distributions as experiments $P_n \sim n^{-2}$ (Figure 3-12B) and this perfectly matches with previous results for isotropic templating. The cluster size distribution when mean ice crystal size is either smaller (~20 µm) or greater (~80 µm) than 50 µm are also independent with dispersion concentrations.

We note that the size and shape of the ice crystals in isotropic and directional freezing are different. The nucleation densities of ice crystals in our simulations is set to match that observed in our experiments. We select the nucleation density such that for isotropic freezing, the mean diameter of the ice crystal at impingement is ~50 µm and for directional ice templating, the width of a distorted rectangular ice crystal is ~30 µm. In Figure 3-13A we show the variation of the number of voids in the simulation box with ice crystal growth. As ice crystals are

nucleated and grow, the number of voids increases. For isotropic freezing, the number of voids reaches a maximum when the average size of the ice crystals is ~34.5 µm. Subsequently, as the ice crystals impinge, voids close up and the number of voids decreases. At the end of the simulation, when the box is filled with ice crystals, there are no voids. For directional cooling, ice seeds are randomly placed at the lower surface of the box and grow uniformly in X, Y and Z-direction. Here, we observe that the number of voids reaches a maximum value when the ice crystal thickness is 15 µm. Similar to the case of isotropic freezing, the number of voids subsequently decreases and approaches zero when the simulation box is filled with ice. In the simulations, we use the average size of the ice crystals as a proxy for the freezing time. The time for complete freezing is obtained as the time for the number of voids in the simulation box to go to zero. Getting completely filled lattices exactly at the maximum size of ice crystal is not always possible due to the stochasticity of the simulations. When the simulation is run 500 times, we find that when the simulation box is filled, the ice crystal size ranges from 41 µm to 50 µm for isotropic freezing and 25 µm to 30 µm for directional freezing. Thus, we assume freezing is complete for directional growth when the ice crystal size is 27 µm and 45 µm for isotropic freezing. In Figure 3-13B we present data for the fraction of the simulation box that is filled with voids, as a function of normalized freezing time, obtained by normalizing the ice crystal size with the size when the number (27 µm for directional 45 µm for isotropic) of voids go to zero.

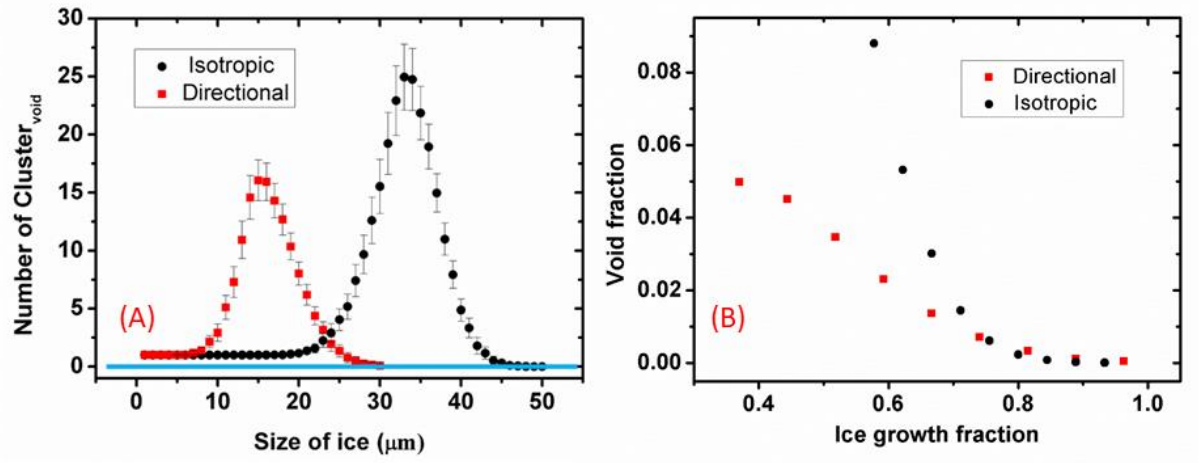

Figure 3-13: (A) The number of voids in the simulation box as a function of ice crystal size as freezing proceeds. The number of voids increases as the ice crystals grow and reaches a maximum at ~15 µm for directional and ~34.5 µm for isotropic freezing. The error bars represent the standard deviation from multiple simulation runs. (B) Variation of void fraction

with respect to the simulation box as a function of ice crystal growth fraction (here both box sizes for isotropic and directional are same).

The key difference between the cluster sizes distributions obtained in the case of isotropic versus directional freezing is that the power law exponent that characterizes this distribution is concentration dependent for directional ice templating. This behaviour is observed over a wide range of concentrations (all sufficiently dilute that we do not form percolated monolithic structures) and is seen in experiments and in toy simulations where the only physics incorporated is exclusion of particles from the growing ice and hard sphere particle interactions until they contact to aggregate irreversibly. We rationalize these differences as follows.

In isotropic freezing, ice nuclei form in the bulk and grow isotropically until impingement. At impingement, this results in an average ice crystal size of ~ 50 μm. In contrast, in directional freezing, ice crystals are nucleated at the cold bottom surface and grow vertically as sheets, to a first approximation, characterized by a sheet thickness of ~ 30 μm. Thus, as nucleation happens in the bulk in isotropic freezing, as opposed to at the lower surface in the directional case, the number density of ice crystals is higher for isotropic freezing (average, per simulation box). Also, importantly, there is a difference in the geometry of the ice crystals in the two experiments, and therefore in the geometry of the shape of the voids as they close up on each other. Directional freezing results in the formation of parallel sheets of ice and particle clusters are trapped as these walls approach each other, in contrast to case of impingement of isotropically growing ice crystals for isotropic freezing. Previous work clearly indicates that under these experimental conditions, colloidal particles are expelled by the growing ice front and are localized in the dispersion (or “voids”) until the ice crystals impinge to close up the voids and trap the particles.

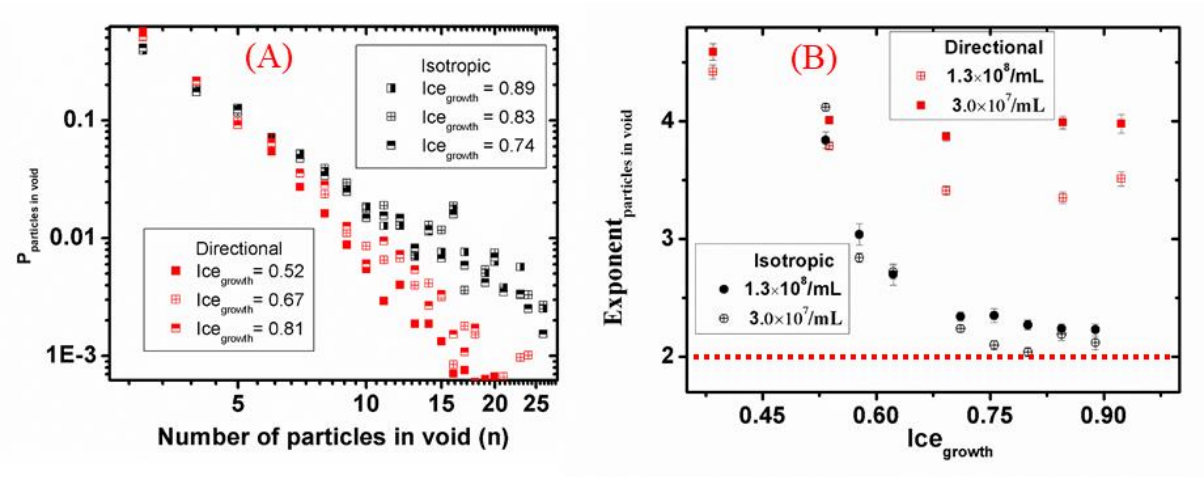

Figure 3-14: (A) Fractional probability of particles in void at different time. (Red colour) represents the data for directional templating and (black colour) represents isotropic ice templating. In both the processes, particle concentrations = 1.3×10^8/mL. (B) Exponent derived from the distribution of particles in voids. For isotropic templating, the exponent is close to 2 for all concentrations after an ice crystal growth fraction = 0.75. For directional templating, exponents depend on the particle concentrations. For high concentration (viz. 1.3×10^8/mL) the exponent is ~ 3.5 and for a concentration of 3.0×10^7/mL, the exponent is ~4.0, after the ice growth fraction exceeds 0.50.

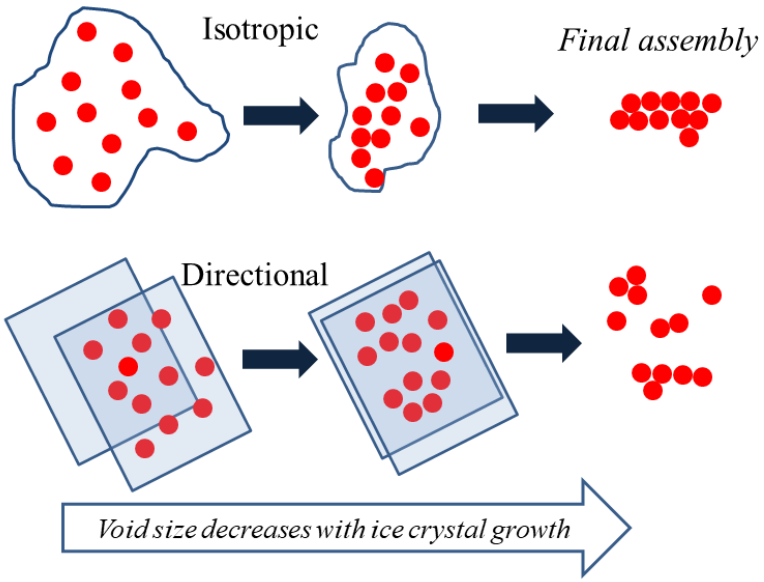

Figure 3-15: Schematics of particles in a void. In isotropic cooling particles in void eventually forms a cluster at final stage (1st row), but for directional cooling, particles in a void split into multiple smaller cluster at the final stage (2nd row).

Simulations provide us information on the number of particles in a void as the ice crystals grow. In Figure 3-14A, we plot the number distribution of particles in voids (for concentration 1.3×10^8/mL particles) for directional and isotropic freezing, and observe the evolution of this distribution as the ice crystals grow. We parametrize the extent of ice growth by normalizing the average ice crystal size by the size of the crystal at impingement, obtained when the voids tends to close up (Figure 3-13A). We observe that as the ice crystals start growing, there is an increase in the number of voids. The number of voids goes through a maximum and then deceases until the voids close up, so that there are no voids at impingement. Initially, when the voids start forming, the vast majority of voids contain only a small number of particles and there are very few voids that contain a large number of particles. This is true for both isotropic and directional freezing and results in power laws with large values of the exponent, η (Figure 3-14B). However, as the voids start closing up, the voids that form contain larger number of particles, resulting in a decrease in η. For directional freezing, as the parallel walls of ice approach, the particles are confined in planar voids of small thickness and large lateral extent. When the ice crystals impinge, voids close up abruptly trapping particles into clusters. Thus, in this experiment, the dispersion concentration determines the probability of particle clustering at impingement. The higher the colloid concentration in dispersion, the higher the chance of larger clusters forming. Thus, η is a function of particle concentration and decreases with increase in concentration. This is consistent with the simulation results. For isotropic freezing too, as ice crystals grow, there is an increase in the number of voids that corresponds to a decrease in η. However, in contrast to the case of directional freezing, η converges to the same value (~2), independent of dispersion concentration (Figure 3-14B). We rationalize this as a consequence of the shape of the voids as they close up. Unlike the case of directional freezing, all the particles in a void form a cluster as the void closes up due to isotropic growth of the ice crystals. This is schematically represented in Figure 3-15. Thus, there is a qualitative difference in the concentration dependence of the power law exponents in isotropic and directional freezing experiments.

3.6 CONCLUSIONS

Directional ice templating of very dilute dispersions results in the formation of particle assemblies (small clusters, linear chains, two particle-wide tapes and 2D sheets). We hypothesize that the geometry in which the ice crystals approach each other as they impinge determines the distribution of particle cluster sizes. The cluster size distribution is obtained as

a power law, with a concentration dependent power law exponent. The cluster size distribution, P_n (n > 2) ~$n^{-\eta}$, where η varies from 2.27 (for particle concentrations ~10^9 particles/ mL) to 3.19 (for particle concentrations ~ 10^7 particles/ mL). This is qualitatively different from the case of isotropic freezing, where a concentration-independent power law is obtained for the cluster size distribution. Experimental results show near quantitative match with simulations that invoke only that particles interact through hard-sphere interactions, that they stick irreversibly on contact and that they are expelled from growing ice crystals.

3.7 REFERENCES

1. Perry, R. W., Holmes-Cerfon, M. C., Brenner, M. P. & Manoharan, V. N. Two-Dimensional Clusters of Colloidal Spheres: Ground States, Excited States, and Structural Rearrangements. *Phys. Rev. Lett.* **114**, 228301 (2015).

2. Lin, M. Y. et al. Universality in colloid aggregation. *Nature* **339**, 360–362 (1989).

3. Manoharan, V. N., Elsesser, M. T. & Pine, D. J. Dense packing and symmetry in small clusters of microspheres. *Science.* **301**, 483–487 (2003).

4. Zerrouki, D., Baudry, J., Pine, D., Chaikin, P. & Bibette, J. Chiral colloidal clusters. *Nature* **455**, 380–382 (2008).

5. Ahn, J. S., Hammond, P. T., Rubner, M. F. & Lee, I. Self-assembled particle monolayers on polyelectrolyte multilayers: Particle size effects on formation, structure, and optical properties. *Colloids Surfaces A Physicochem. Eng. Asp.* **259**, 45–53 (2005).

6. Meakin, P. Formation of fractal clusters and networks by irreversible diffusion-limited aggregation. *Phys. Rev. Lett.* **51**, 1119–1122 (1983).

7. Smay, J. E., Gratson, G. M., Shepherd, R. F., Cesarano, J. & Lewis, J. A. Directed colloidal assembly of 3D periodic structures. *Adv. Mater.* **14**, 1279–1283 (2002).

8. Ozin, G. A. & Yang, S. M. The race for the photonic chip: Colloidal crystal assembly in silicon wafers. *Adv. Funtional Mater.* **11**, 95–104 (2001).

9. Gong, J. & Wu, N. Electric-Field Assisted Assembly of Colloidal Particles into Ordered Nonclose-Packed Arrays. *Langmuir.* **33**, 5769–5776 (2017).

10. Retsch, M. et al. Fabrication of large-area, transferable colloidal monolayers utilizing

self-assembly at the air/water interface. *Macromol. Chem. Phys.* **210**, 230–241 (2009).

11. Dai, Z., Li, Y., Duan, G., Jia, L. & Cai, W. Phase diagram, design of monolayer binary colloidal crystals, and their fabrication based on ethanol-assisted self-assembly at the air/water interface. *ACS Nano* **6**, 6706–6716 (2012).

12. Broide, M. L. & Cohen, R. J. Experimental evidence of dynamic scaling in colloidal aggregation. *Phys. Rev. Lett.* **64**, (1990).

13. Kolb, M., Botet, R. & Jullien, R. Scaling of kinetically growing clusters. *Phys. Rev. Lett.* **51**, 1123–1126 (1983).

14. Vicsek, T. & Family, F. Dynamic scaling for aggregation of clusters. *Phys. Rev. Lett.* **52**, 1669–1672 (1984).

15. Weitz, D. A. & Lin, M. Y. Dynamic Scaling of Cluster-Mass Distributions in Kinetic Colloid Aggregation. *Phys. Rev. Lett.* **57**, 2037–2040 (1986).

16. Deville, S. Freeze-casting of porous ceramics: A review of current achievements and issues. *Adv. Eng. Mater.* **10**, 155–169 (2008).

17. Gutiérrez, M. C., Ferrer, M. L. & Del Monte, F. Ice-templated materials: Sophisticated structures exhibiting enhanced functionalities obtained after unidirectional freezing and ice-segregation- induced self-assembly. *Chem. Mater.* **20**, 634–648 (2008).

18. Deville, S., Saiz, E. & Tomsia, A. P. Ice-templated porous alumina structures. *Acta Mater.* **55**, 1965–1974 (2007).

19. Nishihara, H., Mukai, S. R., Yamashita, D. & Tamon, H. Ordered macroporous silica by ice templating. *Chem. Mater.* **17**, 683–689 (2005).

20. Rajamanickam, R. et al. Soft colloidal scaffolds capable of elastic recovery after large compressive strains. *Chem. Mater.* **26**, 5161–5168 (2014).

21. Francis, N. L. et al. An ice-templated, linearly aligned chitosan-alginate scaffold for neural tissue engineering. *J. Biomed. Mater. Res. Part A* **101**, 3493–3503 (2013).

22. Deville, S. et al. Metastable and unstable cellular solidification of colloidal suspensions. *Nat. Mater.* **8**, 966–972 (2009).

23. Pot, M. W. et al. Versatile wedge-based system for the construction of unidirectional

collagen scaffolds by directional freezing: Practical and theoretical considerations. ACS *Appl. Mater. Interfaces* **7**, 8495–8505 (2015).

24. Zhang, H., Long, J. & Cooper, A. I. Aligned porous materials by directional freezing of solutions in liquid CO2. *J. Am. Chem. Soc.* **127**, 13482–13483 (2005).

25. Chatterjee, S., Sen Gupta, S. & Kumaraswamy, G. Omniphilic Polymeric Sponges by Ice Templating. *Chem. Mater.* **28**, 1823–1831 (2016).

26. Vicsek, T. & Family, F. Dynamic scaling for aggregation of clusters. *Phys. Rev. Lett.* **52**, 1669–1672 (1984).

27. Toledano, J. C. F., Sciortino, F. & Zaccarelli, E. Colloidal systems with competing interactions: From an arrested repulsive cluster phase to a gel. *Soft Matter* **5**, 2390–2398 (2009).

28. Valeriani, C. et al. From compact to fractal crystalline clusters in concentrated systems of monodisperse hard spheres. *Soft Matter* **8**, 4960–4970 (2012).

29. Heyes, D. M. & Melrose, J. R. Percolation cluster statistics of lennard-jones fluids. *Mol. Phys.* **66**, 1057–1074 (1989).

30. Van Dongen, P. G. J. & Ernst, M. H. Dynamic scaling in the kinetics of klustering. *Phys. Rev. Lett.* **54**, 1396–1399 (1985).

31. Kono, S., Kon, M., Araki, T. & Sagara, Y. Effects of relationships among freezing rate, ice crystal size and color on surface color of frozen salmon fillet. *J. Food Eng.* **214**, 158–165 (2017).

Chapter-4

Passive and Active Dynamics of Colloidal Chains

The simulations presented in this Chapter are performed by our collaborators, Dr. Raj Kumar Manna and Dr. Abhrajit Laskar, supervised by Prof. PB Sunil Kumar (IIT-Madras) and Prof. Ronojoy Adhikari (Institute of Mathematical Sciences). Simulation results are presented for completeness.

4.1 INTRODUCTION

Active systems are characterized by an energy flux through them - therefore, they are out of equilibrium.[1] All living organisms are active in this sense - for example, motility within living cells relies on molecular motors that use chemical reactions to power mechanical motion and effect directed transport.[2–4] Synthetic systems that mimic active biological systems hold promise for applications ranging from micro-robots and micromixing to targeted drug delivery.[5–12] Several schemes to realize active colloidal systems have been demonstrated.[13–18] One class of active colloids relies on the imposition of external fields: electric,[19–21] magnetic[7],[22-23] or light[17,24] to deliver energy to the colloidal system. In another class, chemical transformations are carried out on the colloidal surface to convert chemical energy to mechanical motion.[6,25–28] To effect self-propulsion of individual colloids in dilute systems, it is necessary to break symmetry. This symmetry breaking can arise from interactions with external fields, for example, through electro hydrodynamic phenomena that result in colloidal rotation about an axis normal to the imposed electric field.[20] Symmetry breaking can also arise

from hydrodynamic interactions of colloids with boundaries.[29] In colloidal systems that convert chemical to mechanical energy, symmetry breaking typically arises from the preparation of chemically anisotropic colloids, such as Janus colloids.[5,11,27-28,30]

One can also induce symmetry breaking by interactions between colloids in concentrated systems. For example, recent work has demonstrated the formation of self-assembled swarms, bundles and strings through interactions between active colloidal moieties.[19–24,31–34] In these reports, asymmetry at the level of an individual colloidal particle renders them active. The strength and directionality of interactions between these active colloids governs emergent assembly in concentrated colloidal dispersions. Another way to induce symmetry breaking is to bond together colloidal particles, each of which is isotropic, to form chains. Recent simulations have demonstrated that semi-flexible chains comprising active beads can exhibit autonomous motion,[35–39] reminiscent of flagellar beating. Two aspects were important for observing active effects in these simulations: (i) the semi-flexible nature of the chain allows thermal noise to continually break symmetry and (ii) covalent bonding of individual active beads along the chain allows for spatial proximity so that there is strong hydrodynamic coupling between them. Thus, while each of the beads is isotropic, symmetry breaking happens due to Brownian fluctuations in chain conformations. In such systems, out-of-equilibrium dynamics results from bead-bead interactions due to active flows. However, an experimental realization of this system has not been reported. One advantage of such a system is the ease of preparation of isotropic colloids relative to Janus entities. These synthetic systems also hold promise as models for studying the mechanisms that govern biological flagellar dynamics.[40–44] Combining these mechanistic insights with the ease of fabrication of such active systems might provide a way to address the challenge of enhancing transport phenomena at small length scales.

Here, we report the facile preparation of active colloidal chains that exhibit over 60% enhancement in diffusivity over their passive counterparts. The colloids that are enchained to form necklaces are uniformly coated with platinum nanoparticles that catalyze the decomposition of hydrogen peroxide - unlike self-motile Janus colloids. Our experiments match well with simulations performed by our collaborators that show that the "active" enhancement in diffusivity arises from interactions between enchained colloids due to phoretic hydrodynamic flows.

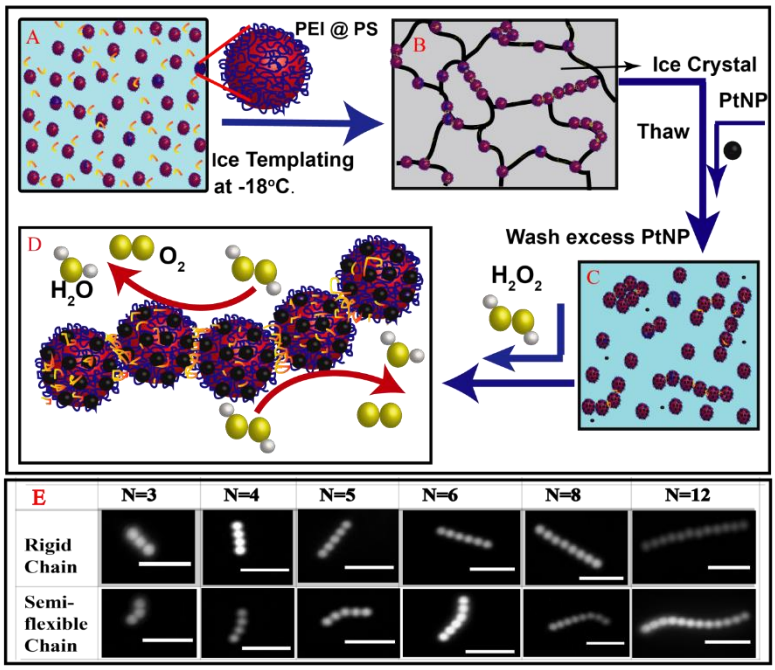

Figure 4-1: Ice templating route to synthesis of active colloid chains. (A) Polyethyleneimine (PEI) coated 1 μm-sized polystyrene particles (PS) and cross-linker (PEG di-epoxy) are mixed in aqueous suspension. (B) When the suspension is cooled to $-18^{o}C$, PEI-coated PS and cross-linker accumulate along the grain boundaries of crystalline ice. The PEI forms a crosslinked mesh, so that the colloids are linked into chains. (C) The suspension containing cross-linked colloid chains is thawed, PtNPs are added and mixed by slow shaking for one minute. The suspension is left undisturbed for 2 hours to allow PtNPs to adsorb and the chains to sediment. The suspension is decanted and re-diluted with DI water, the process being repeated twice, to remove excess PtNPs. (D) 100 μL of 30% H_2O_2 is added to 100 μL of chain suspension, with slow shaking for one minute, to render the chains active. (E) Representative images from fluorescent microscopy of rigid and semi-flexible colloidal chains (N = 3 to 12). The scale bar in all the images is 5 μm.

4.2 MATERIALS AND METHODS

4.2.1 MATERIALS

Polyethyleneimine (PEI) (50% w.v solution; $M_w = 750$ kg/mol, specified by the supplier) and polyethyleneglycol diepoxide (PEG-diepoxide, molecular weight = 500 gm/mol, specified by the supplier), chloroplatinic acid hexahydrate and horseradish peroxidase (HRP) were obtained from Sigma-Aldrich and were used as received. A 2.5 % w.v dispersion of fluorescent

(Rhodamine-B labelled) polystyrene (PS) beads with a size of 1.08 μm and 4 % polydispersity were used as received from Microparticles GmbH, Germany. Sulphonate groups present on the surface rendered the PS particles negatively charged. Hydrogen peroxide (30 % aqueous solution), 4-aminoanipyrine (4-AAP) 98 % and phenol, 98 % were used as received from Avra Synthesis Pvt. Ltd.

4.2.2 PREPARATION OF COLLOIDAL CHAINS

The synthesis of active colloidal chains is schematically depicted in Figure 4-1. 1 μL of polystyrene (PS) latex particles was added to 200 μL DI water. After sonication for two minutes to disperse the particles, this was added to 5 μL of PEI stock solution (comprising 100 mg PEI in 1mL DI water) and the mixture was vortexed for 5 minutes. This dispersion was centrifuged and the supernatant was removed to separate unadsorbed PEI. This was diluted with DI water and sonicated for two minutes to redisperse the PEI coated PS colloids. The zeta potential of the PS particle changes from -30mV to +57mV after treatment with PEI, confirming coating of the PS surface. To this was added 1 μL PEG-diepoxide diluted in 1mL DI water and the mixture was then vortexed and subsequently sonicated for 1 minute. This mixture was then stored in a refrigerator maintained at -18^0C. The water is transformed into ice on freezing, and the colloids, polymer and cross-linker are concentrated at the boundaries between ice crystals. PEI is crosslinked by PEG- diepoxide in the frozen state. We observe that allowing the crosslinking to proceed for 12 hours results in the formation of a rigid chain. Decreasing the crosslinking time to 8 hours yields semi-flexible chains and highly flexible chains are obtained when we crosslink for 4-5 hours. After crosslinking, we thaw the frozen sample at room temperature.

4.2.3 CHARACTERIZATION OF PtNPs

PTNPs were provided by Dr. Jhumur Seth and Dr. BLV Prasad (CSIR-National Chemical Laboratory).

PtNPs were synthesized according to a reported protocol.[45] Platinum nanoparticles were characterized using TEM, (Figure 4-2a). The size distribution of platinum nanoparticles, obtained by analyzing TEM images is shown in the inset (Figure 4-2a). The synthesized PtNPs are characterized by a number average size of 1.5 nm. Zeta potential measurements reveal that platinum nanoparticles are negatively charged, with a zeta potential of -60 mV. For the

measured average PtNPs size = 1.5 nm, we estimate the final concentration of PtNPs as 2.4×10^{10} per μL.

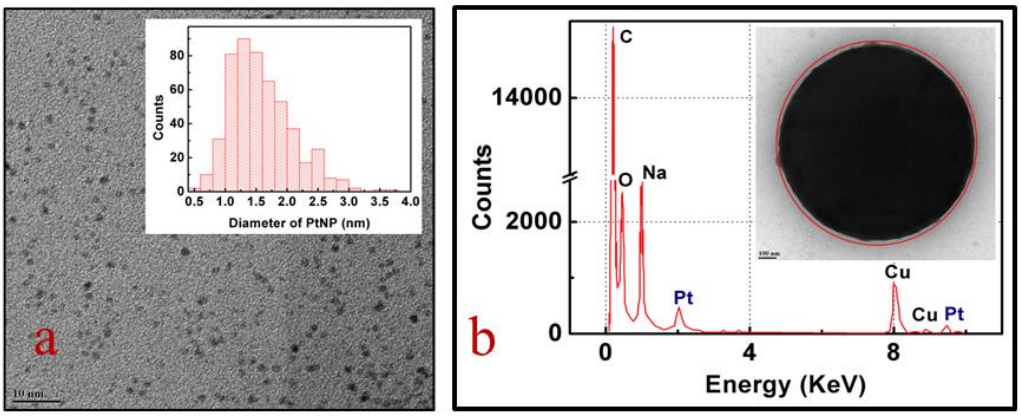

Figure 4-2: (a) TEM image of PtNPs, and (inset) size distribution of the PtNPs. (b) We perform elemental mapping on the region marked by the red circle. The particle marked by the red circle is a PtNPs coated PS particle. We can clearly see evidence for the presence of platinum. The Na comes from the Na-citrate used to electrostatically stabilized the PtNPs.

4.2.4 ADSORPTION OF PtNPs ON PS

In control experiments on single colloidal particles coated with PEI, we observe that the zeta potential of the PEI coated PS colloids decreases from +57mV to + 10mV after adsorption of PtNPs. Elemental mapping in Figure 4-2b confirms the presence of platinum on the surface of extensively washed PEI-coated PS colloids, confirming adsorption of PtNPs on the colloid surface. We estimate the coverage of PEI-coated PS particles by PtNPs as follows. We treat a known concentration of PEI-covered PS particles ($\sim10^8$ particles in 0.5 mL) with an excess of PtNPs from a solution with known concentration ($\sim2.4\times10^{10}$per μL). After allowing 90 minutes for PtNPs adsorption, we separate out the PS particles by centrifugation, leaving the unadsorbed platinum nanoparticles in the supernatant solution. The concentration of PtNPs in the supernatant is assayed and the coverage of PtNPs on PEI-coated PS is obtained as a difference. We use a modification of a reported protocol[46] to assay the concentration of PtNPs in solution. Briefly, we add 100 μL of PtNPs containing supernatant solution to 900 μL of a solution comprising 10 μL of 0.2 mM H_2O_2, 2 μL HRP (1 mg/2 mL), 444 μL phenol (25 mM) and 444 μL 4-AAP (0.4 mM). PtNPs and HRP compete to decompose H_2O_2 and steady state is attained after 30 minutes when the peroxide is completely consumed. We measure the UV-Vis absorbance at 510 nm at steady state and relate this to the concentration of PtNPs, using a

calibration curve prepared using PtNP solutions of known concentration. Using this method, we estimate a PtNP coverage of 5.9×10^3 PtNPs adsorbed per PS colloid.

4.2.5 EXPERIMENTS ARE CARRIED OUT AT CONSTANT H_2O_2 CONCENTRATION

PtNPs coated PS chains are active in the presence of H_2O_2 , and the level of activity is related to the concentration of H_2O_2. We observe the diffusivity of active colloidal chains in the presence of peroxide at a concentration = 15 % w.v, and observe the chains in the microscope over a period of several minutes. We determine the concentration of H_2O_2 over the time scale of our measurements as follows. We prepare a "reaction mixture" containing 100 μL H_2O_2 (30 % w/v) and 100 μL of PtNPs (at a concentration of ~2.4×10^{10}/μL, note that the concentration of PtNPs in this reaction mixture is significantly higher than in our microscopy experiments where we observe dilute solutions of PtNPs coated PS colloidal chains). As the reaction proceeds, viz. PtNPs decompose H_2O_2, we obtain 2 μL aliquots of the reaction mixture every 3 minutes. This is added to a solution containing 494 μL of phenol (2.5mM), 494 μL of 4-AAP (0.4mM) solution, 10 μL of HRP (1 mg/mL).We allow 30 minutes so that all the peroxide is decomposed and a steady state is achieved. We then dilute the solution 60-fold and measure the UV-Vis absorbance at 510 nm. As the concentrations of PtNPs and HRP are fixed, the intensity of absorbance is a function of the concentration of H_2O_2. We plot the UV- Vis absorbance so obtained as a function of reaction time (Figure 4-3) and show that, even at these high PtNPs concentrations, there is no experimentally significant change over 30 minutes. Thus, the peroxide concentration (or, equivalently, the activity) is unchanged over the time scale of microscopic observation.

4.2.6 METHOD OF INJECTION OF H_2O_2:

We add 100 μL of PtNPs coated colloidal chains dispersion in 100 μL of 30 % w.v. H_2O_2 and wait for a minute to mix the sample properly. After that we load the sample in a cavity slide and seal it properly so that there is no leakage.

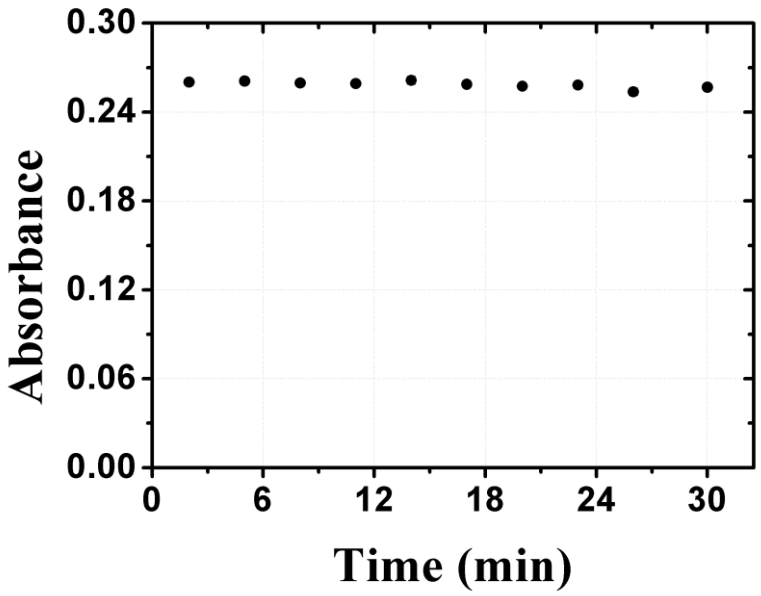

Figure 4-3: UV-Vis absorbance at 510 nm as a function of reaction time, as described in. There is no change in the UV-Vis absorbance, viz. no change in hydrogen peroxide concentration over a time scale of 30 minutes.

4.2.7 VIDEO RECORDING AND DATA ANALYIS

Laser Scanning Fluorescence Microscopy (Carl Zeiss Axio Observer Z1) was used with a 63X objective (NA=1.4 and working distance = 0.19 mm). Samples were taken in a cavity slide. Great care was taken to seal the slides to eliminate convective effects. Fluorescent PS beads were excited with laser light (wavelength = 543 nm). We recorded images at 20fps for more than 40 seconds. Image analysis was performed using ImageJ software and Matlab. To find the center of mass of the colloidal chain, we used ImageJ. We subtract a constant background and then threshold the images. We used the inbuilt Particle Analysis function in ImageJ to obtain the center of mass of the chain. A sequence of images was then used to obtain the MSD for the chain center of mass. We calculate the mean square displacement in 2-dimensions as, MSD(t)= $< (x(t) - x(0))^2 + (y(t) - y(0))^2 >$, where x(t) and y(t) are the center of mass coordinates at time t, obtained from ImageJ. The MSD is linear in time with a slope = 4D, where D is diffusion coefficient (slope = 4D since we track the colloidal chains in 2 dimensions). As a check on the ImageJ analysis, we used the particle tracking function in Matlab to obtain the center of mass for each colloidal monomer and calculated the chain center of mass based on these coordinates. Analysis using ImageJ was consistent with that using Matlab. We used the

Matlab to find the center of mass positions of the colloidal beads in a chain to estimate chain flexibility.

4.2.8 ELIMINATION OF CONVECTIVE FLOWS

We loaded colloidal chain suspensions in a cavity slide and carefully placed a cover slip on top, ensuring that there are no trapped air bubbles. The cover slip was then sealed using nail polish to prevent solvent evaporation. Careful sealing of the cover slip to the slide is critical to eliminate solvent evaporation and convective flows. To confirm that convective flows are eliminated, we present data on the trajectories of two particles observed simultaneously, in the same field of view (Figure 4-4a). In the inset we plot the velocity-velocity correlation between the two particles. It is clear that the motions of the two particles are uncorrelated. We also plotted the MSD for x and y motions, MSD_x and MSD_y in Figure 4-4b for arbitrarily defined x and y axes, as indicated in Figure 4-4a. We observe that MSD_x and MSD_y are identical, to within experimental error. We calculate $D_x = 0.16\ \mu m^2/s = D_{yx} = 0.16\ \mu m^2/s = D/2$, where $D = (D_x + D_y) = 0.32 \mu m^2/s$. This matches well with the theoretical value of Brownian diffusivity in three dimensions, $D=(D_x + D_y + D_z) = {k_B T}/{6\pi\eta R} = 0.47\ \mu m^2/s$ (in water at 25^0C where R is the radius of the colloid). Thus, chain motion measured in two orthogonal directions yield experimentally indistinguishable values of mean-squared displacement (MSD) and, where multiple particles are observed in the same field of view, we observe that particle motions are uncorrelated, confirming the absence of convective flows.

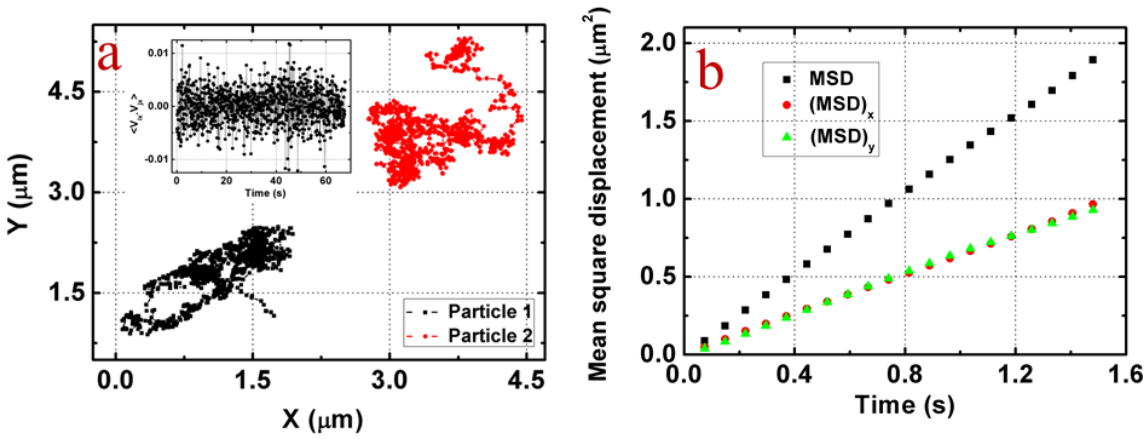

Figure 4-4: Shows the trajectory of two particles in 2-dimensions over a period of 60s. In the inset we plot the velocity-velocity correlation, $\langle V_{ix}.V_{jy}\rangle$ of these two particles (b) MSD as a function of time for x-motion and for y-motion for a single Brownian particle.

4.2.9 DIFFUSION OF SINGLE PARTICLE (PASSIVE AND ACTIVE)

We plot ηD (where η is the viscosity of the solvent and D is the corresponding diffusion coefficient) for a colloidal particle without the platinum nanoparticle coating in both water and 15% w/v aqueous hydrogen peroxide and with the platinum coating in water (Figure 4-5). Each of these combinations is passive. We also present data for the active case, where we observe PtNPs-coated single colloidal particle is dispersed in 15% w/v hydrogen peroxide. All measurements are done in the dilute regime where individual colloids are well separated. The values of ηD in all these experiments are identical within experimental error.

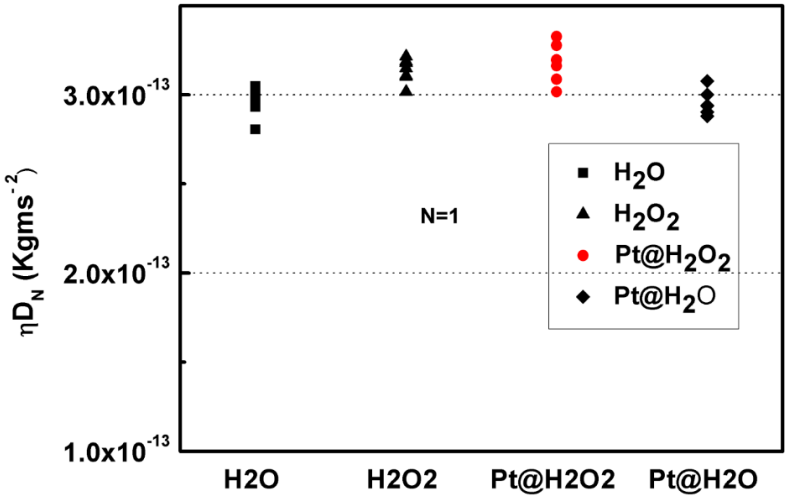

Figure 4-5: Single particle diffusion for four different passive cases, as described in the text: (PS in H_2O, PS in H_2O_2, active PS (PtNP@PS) in H_2O_2 and PS in H_2O with PtNPs.

4.2.10 ACTIVE COLLOIDAL CHAINS

An aqueous dispersion of colloidal chains, comprising PS colloids in a crosslinked PEI mesh, is treated with an excess of platinum nanoparticles (PtNPs). PtNPs are negatively charged and adsorb on the surface of the colloidal chains. Elemental mapping (Figure 4-2) confirms the presence of platinum on the surface of extensively washed PEI-coated PS colloids, confirming adsorption of PtNPs on the colloid surface. We verify that the colloids are isotropically coated with PtNP catalyst as follows. In control experiments, we measure the diffusion of single PS colloids coated with PEI and with PtNPs adsorbed on their surface. The diffusivity of such colloids in the presence of hydrogen peroxide is experimentally indistinguishable from that in water, after accounting for differences in solvent viscosity (Figure 4-5). This suggests that there

is no significant asymmetry in the coverage of PtNP over the PS colloid surface. We estimate PtNPs coverage of 5.9×10^{3} PtNP adsorbed per PS colloid (Subsection - 4.2.4 above).

A dispersion of PtNPs coated colloidal chains is added to an equal volume of 30% (w.v) hydrogen peroxide. The PtNP on the particle surface catalyse decomposition of the hydrogen peroxide, rendering the chains active. There is no change in concentration of hydrogen peroxide during the experimental duration when the chains are visualized (subsection 4.2.5, Figure 4-3).

4.3 CHARACTERIZATION OF CHAINS

4.3.1 FLEXIBILITY CALCULATION

We define the chain flexibility (ξ) as $<(R_N(t) - < R_N >)^2> = L^2\xi^2$, where $R_N(t) = r_N(t) - r_1(t)$ is the end to end distance of the chain at time *t*, and L= (N-1)b is the contour length of the chain. As an example, we plot $R_N(t)$ for the case of a rigid 4-mer chain ($\xi = 4\times10^{-4}$) and for a semi-flexible chain ($\xi = 5.4\times10^{-3}$). For rigid chains, we note that $\frac{R_N^e}{R^c}$ (R_N^e is the end to end distance of the colloidal chain and R^C is the contour length of the chain) can occasionally exceed 1 – this is a consequence of the flexibility of the crosslinked mesh that bonds the colloids (Figure 4-6). Thus, the bond length occasionally exceeds its time averaged value, b.

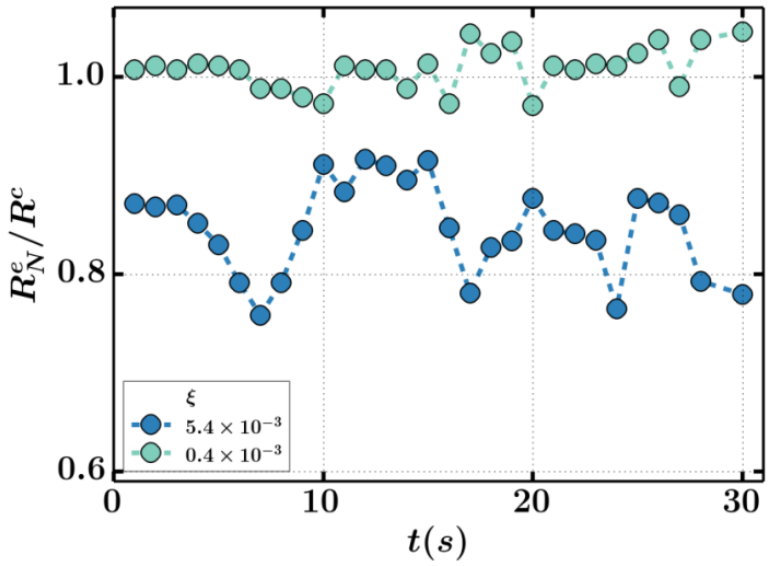

Figure 4-6: Time variation of end-to-end distance of a semi-flexible chain and a rigid chain. Here, N = 4 and the ξ values are as indicated in the legend.

4.3.2 SPRING CONSTANT (k) AND BENDING RIGIDITY (κ)

We obtain the distribution in center to center distance between bonded colloids by examining over 200 fluorescent microscopy images of chains. This is performed for chains with different flexibility (ξ). We fit this distribution to a Gaussian and obtain the spring constant, k, that characterizes colloidal bonding from: $P(r) \sim \exp(-\frac{k(r-r_c)^2}{k_B T})$, where r_c is the mean of fluctuations. We estimate the fluctuation by taking the difference from average centre to centre distance to centre to centre distance at any time. As ξ increases from 1.3×10^{-3} to 2.1×10^{-3} to 4.2×10^{-3} there is a decrease in k from 1319.5 $k_B T(\mu m)^{-2}$ to 318.5 $k_B T(\mu m)^{-2}$ to 229.2 $k_B T(\mu m)^{-2}$. Similarly, we obtain the distribution of bond angles (as indicated in Figure 4-7, inset) for chains with different flexibility, ξ. We fit this distribution, $P(\theta) \sim \exp(-\frac{\kappa \theta^2}{k_B T})$, where θ is the angle between two consecutive bond vectors. As ξ increases from 1.2×10^{-3} to 1.92×10^{-3} to 3.22×10^{-3} there is a decrease in κ from 0.0144 $k_B T(\theta)^{-2}$ to 0.0035 $k_B T(\theta)^{-2}$ to 0.0014$k_B T(\theta)^{-2}$.

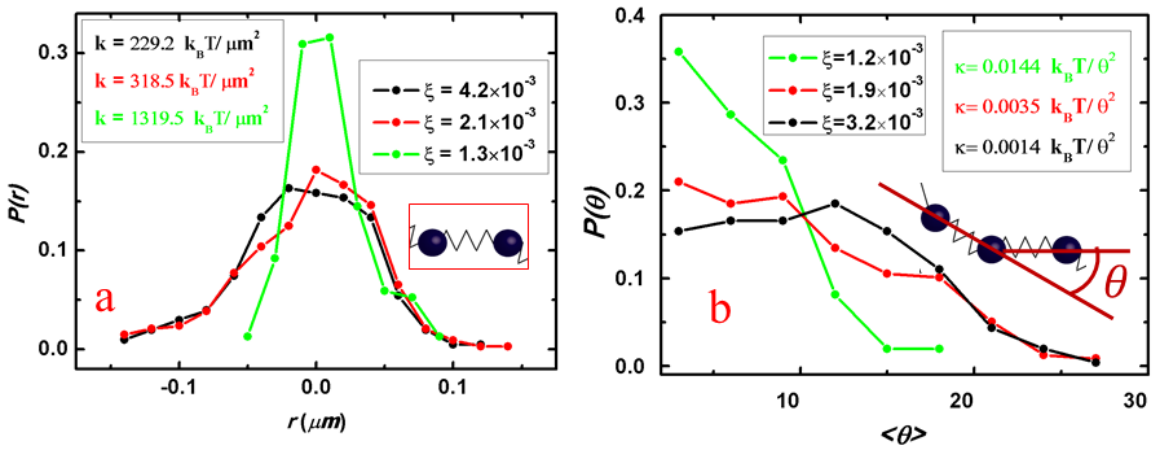

Figure 4-7: (a) Inter-particle distances are narrowly distributed for rigid chain whereas the distribution of relatively flexible chains are wider. (b) Similarly, the distribution of angle between two bond vectors is narrow for rigid chain and wider for relatively flexible chains.

4.3.3 HYDRODYNAMIC RADIUS

We calculate the hydrodynamic radius (Figure 4-8) as $R_h^{-1} = \frac{1}{N^2} \sum_{i\neq j}^{N} \frac{1}{r_{ij}}$ where r_{ij} is the distance between the i^{th} and j^{th} beads. We cannot distinguish between R_h for active and passive chains to within experimental error (data for N = 4 and 6 are presented in (Figure 4-8).

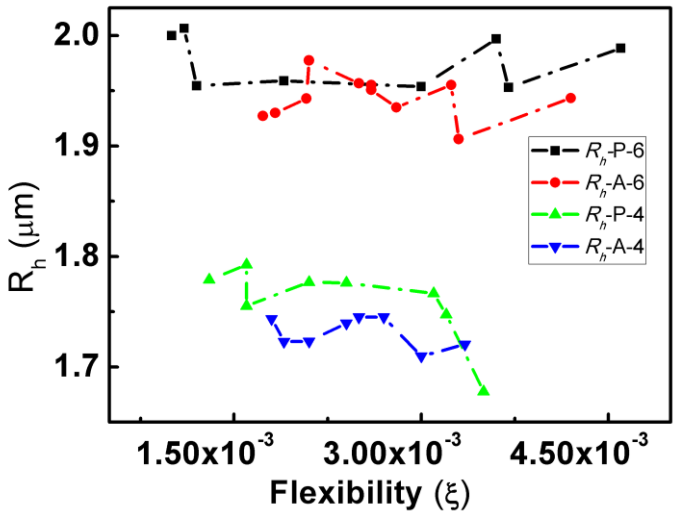

Figure 4-8: Hydrodynamic radius for active ($R_h - A$) and passive ($R_h - P$) chain (with N=4 and 6) as a function of chain flexibility.

4.4 SIMULATION DETAILS

Our collaborators performed Brownian microhydrodynamic simulations using a well-established mathematical model.[35,38] The model describes the Brownian motion of beads interacting through conservative forces, that enforce connectivity and stiffness, and dissipative forces, from Stokes drag and activity. The motion of the N beads are described by the following coupled stochastic differential equations

$$dr_i = \left(\mu_{ij}.F_j + \pi_{ij}.S_j \right)dt + (\sqrt{2\mathbb{D}})_{ij} \cdot W_j \qquad (5)$$

with repeated indices being summed over.

Here $F_j = -\nabla_j U$ are the conservative forces derived from the interaction potential U ($R_1, \ldots r_N$) (that includes the bending elasticity) and μ_{ij} are mobility tensors connecting the velocity of particle *i* due to the sum of all non-hydrodynamic forces on particle j, S_j is the active stresslet on the j-th bead and π_{ij} are propulsion tensors connecting the velocity of particle i to the stresslet on particle j. The thermal forces are described by Wiener processes dWj where $\sqrt{\mathbb{D}}$ is a square-root of the diffusion matrix $\mathbb{D}$ whose matrix elements, by the Einstein relation, are $\mathbb{D}_{ij} = K_B T \mu_{ij}$. The functional forms of the potential, the mobility and the propulsion matrices are provided in the (Eq-6 & Eq-7). It is noted that though each bead has isotropic activity, the presence of neighbouring beads breaks this symmetry and induces anisotropic

effects whose leading term is the stresslet. The sign of the stresslet is set as extensile. This is purely phenomenological and is based on a comparison of simulation results with experiments. The flow-fields around an active colloidal chain are displayed in Figure 4-12.

The active colloidal chain is modelled as a series of N beads of radius a, that can generate spontaneous flows in the surrounding fluid. It is modelled as the generation of spontaneous flow by the beads through extensile stresslets (to leading order), that are oriented along the local tangent to the chain. A set of update equations were derived by considering an instantaneous force balance between dissipative, thermal and conservative forces. Together, these equations represent a set of coupled stochastic equations of motion for N beads of the model chain. In Eq. 5, r_i is the position of the i-th bead. The mobility matrix μ_{ij} and the propulsion matrix π_{ij} are defined as

$$8\pi\eta\mu_{ij}(r, r') = \mathcal{F}_i^0\mathcal{F}_j^0 G(r, r') \tag{6}$$

$$8\pi\eta\pi_{ij}(r, r') = \mathcal{F}_i^0\mathcal{F}_j^l\nabla_j G(r, r') \tag{7}$$

$G_{ij}(r, r') = \frac{\delta_{ij}}{\rho} - \frac{\delta_i\delta_j}{\rho^3}$ is the Oseen tensor with $\rho = r - r'$ and $F_j^l = (1 + \frac{a^2}{4l+6}\nabla_j^2)$.

The diffusion matrix $\mathbb{D}$ is defined as $\mathbb{D}_{ij} = K_B T\mu_{ij}$. The body force, F_i is obtained from the gradient of the potential, $U = U^C + U^E + U^S$ which, in sequence, are potentials enforcing connectivity, stiffness and self-avoidance. The connectivity potential is a two body harmonic spring potential $U^C(r_i, r_{i+1}) = \frac{1}{2}k((r - b_0)^2$ where b_0 refers to the equilibrium bond length and $r = |r_i - r_{i+1}|$.

The stiffness potential $U^E = \bar{k}(1 - \cos\phi)$ penalizes any departure of the angle ϕ between consecutive bond vectors from its equilibrium value of zero. The rigidity parameter $\bar{k}$ is related to the bending rigidity k, as $\bar{k} = k/b_0$. Steric effects are incorporated through the Weeks-Chandler-Andersen potential which vanishes if the distance between any two beads $r_{ij} = r_i - r_j$ exceeds, $r_{min} = 2a$. The stresslet tensor of j-th bead, S_j, which is aligned along the local tangent t_j of the chain with its strength S_0 is defined as $S_j = S_0(t_i t_j - \frac{\delta}{3})$.

4.5 RESULTS AND DISCUSSIONS

4.5.1 EXPERIMENTAL RESULTS

Aggregates formed by ice templating are polydisperse in size, and the aggregate size distribution obtained from ice-templating has been described in Chapter 2. We harvest the aggregates by thawing the mixture and work with dilute dispersions so that our investigations are restricted to isolated linear chain-like colloidal assemblies. We vary the stiffness of the chains by varying the crosslinking duration (details in subsection 4.2.2). Preparation of active colloidal chains are described in (Figure 4-1 and details in subsection 4.2.10).

Colloidal chains are electrostatically complexed with platinum nanoparticles (PtNPs), and are rendered active by addition of hydrogen peroxide. PtNPs on the surface of the PS colloids catalyze peroxide decomposition into water and oxygen, and set up diffusophoretic flows.[27,28] The activity is proportional to reaction rate which is, in turn, proportional to the available peroxide concentration. We use a high peroxide concentration and work with dilute chain dispersions so that there is no measurable change in peroxide concentration (Figure 4-3) over a time scale of ~30 minutes, significantly longer than the period over which chain motions are studied. Thus, all our experiments are conducted at constant peroxide concentration or, equivalently, at constant value of activity. Finally, we note that our experiments are at sufficiently dilute chain concentrations so that there is no observable evolution of oxygen bubbles.

We use fluorescence microscopy to resolve the centre, $r_i = 1, ...,$ N, of each bead in the colloidal chain. We ensure that colloidal chains are at least several tens of microns from the top and bottom slide surfaces during the time scale of observation (on the order of several minutes). Over this time scale, sedimentation effects due to gravity are unimportant. Thus, wall effects on chain dynamics can be neglected. The positions, $\{r_i(t)\}$ of the N beads are used to estimate the configurational distributions and chain diffusivity. We investigate chains with N=3… 12, with ξ varying ten-fold, from $\xi = 4\times10^{-4}$ for stiff chains to $\xi = 5\times10^{-3}$ for semi-flexible chains. We use ξ as a measure of flexibility since the persistence length is difficult to estimate reliably in short chains. We measure chain diffusivity in the usual manner by calculating the MSD of the center of mass $r(t) = \frac{1}{N}\sum_i r_i(t)$ and extracting the coefficient of its linear variation with time.

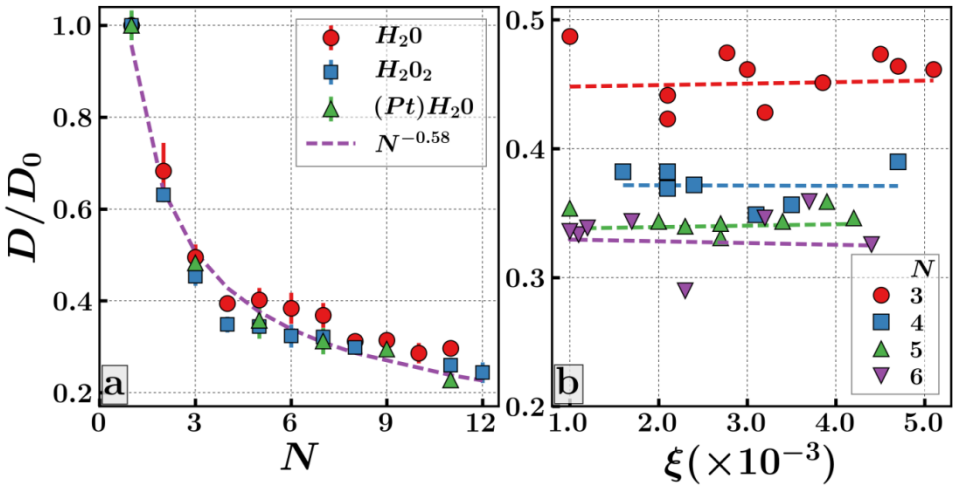

Figure 4-9: Control experiment on passive colloid chains in different solvents. The left panel shows the variation of chain diffusivity D for an N bead chain, normalized by the diffusivity D_0 of a single bead. The dotted line $D \sim N^{\nu}$ with $\nu = -0.58$ is a least-squares fit to the data. Zimm scaling from our simulations predicts $\nu = -0.6$. The right panel shows the variation of the chain diffusivity with flexibility ξ. The slopes of the least-squares lines are close to zero, indicating that the diffusivity does not vary with flexibility.

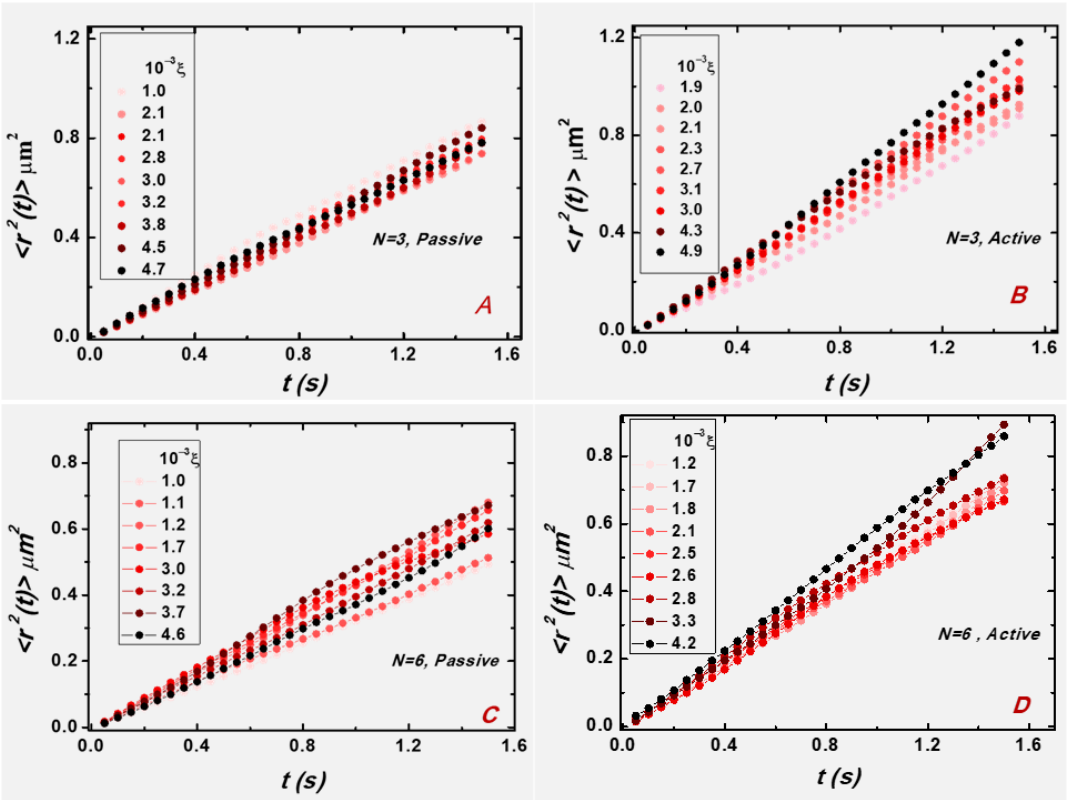

Figure 4-10: Variation of the mean-squared displacement of passive (left panel) and active (right panel) chains with flexibility ξ for N=3 and 6. The mean-squared displacement is comparatively enhanced for active chains, with greater enhancement for more flexible chains.

We begin by presenting control experiments on passive colloid chains, as a baseline for comparison with active chains (Figure 4-9). The left panel shows the normalized diffusivity of colloid chains *without* the platinum nanoparticle coating in both water and 15% w.v. aqueous hydrogen peroxide and *with* the platinum coating in water. Each of these combinations is passive. The diffusivity is fitted well by a power law in N with an exponent ν = -0.58. In the right panel we show that, within experimental resolution, there is no variation of diffusivity with chain flexibility ξ. Our results are consistent with Zimm's treatment[47] of the dynamics of chains that exhibit Gaussian fluctuations. The colloidal chains that we investigate are not flexible. Rather, they can be considered as semi-flexible assemblies that exhibit harmonic fluctuations around the rigid rod limit. As these fluctuations are governed by a Gaussian measure (independent of N), the Zimm pre-averaging strategy can be employed to obtain a power law scaling for the diffusivity. We observe that in the range of parameters considered, passive colloidal chains exhibit Zimm dynamics and their stiffness has no measurable influence on their diffusivity. Zimm scaling for the length dependence of semi-flexible chains has also been reported previously.[48]

We now compare the MSD of passive chains with active chains in 15% w.v aqueous hydrogen peroxide, for chain size N=3 and N=6 but varying flexibility (Figure 4-10). Two features immediately stand out: first, the MSD for flexible active chains is greater than that for passive chains and, second, there is significant variation of the MSD with chain flexibility for active chains, but not for passive. For active chains, there is an increase in MSD with increasing flexibility. While we present data for chains with N = 3 and 6 as an example in Figure 4-10, similar trends are observed for all chain lengths investigated. We now plot normalized diffusivity of the active chains as function of flexibility for chains of different size in Figure 4-11. It is clear that diffusivity increases with flexibility for all chain sizes (compare with Figure 4-9b that shows the flexibility-independent diffusivity of passive chains).

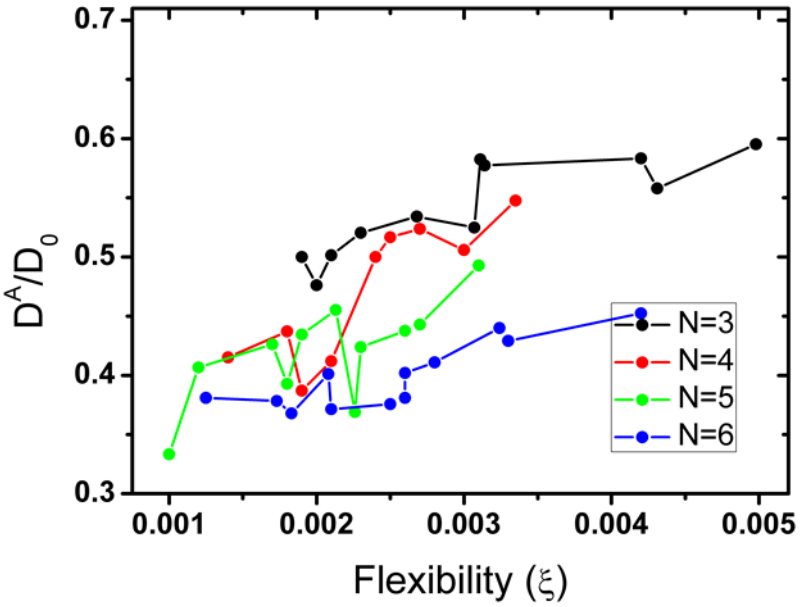

Figure 4-11: Variation of the ratio of diffusivities of active (D^A) normalized by the diffusivity D_0 of a single bead, with flexibility ξ and number of beads N, from experiments.

The uniform coating of platinum nano-particles distinguishes the active colloids in our experiment from Janus particles, in which the catalyst is distributed non-uniformly over the colloid surface. Thus the individual active colloids in this work are chemo-mechanically isotropic in contrast to Janus active colloids.[27,28,49] We observe no enhancement in the diffusivity of active "monomeric" colloidal particles when compared with the corresponding passive particles (Figure 4-5). There is none uniform catalytic reaction due to the enchained colloids and Brownian fluctuation of chain increases the anisotropy which helps to enhance the diffusivity of active chains. Clearly, proximity between enchained colloids provides the source of anisotropy for the active enhancement in diffusivity.

4.5.2 SIMULATION RESULTS

As in the experiments, control simulations of passive chains are conducted by setting $S_j = 0$. The diffusivity is computed for varying flexibility and chain size. The power law exponent (ν = -0.60) for the scaling of diffusivity with N from simulation (Figure 4-14a) is in excellent agreement with experimental data (Figure 4-9a). There is essentially no dependence on chain flexibility of the chain center of mass MSD (Figure 4-13a, compare with Figure 4-10a). It is found that there is approximately one part in a thousand variation of the diffusivity with flexibility, well below the experimental resolution (Figure 4-14b, compare with Figure 4-9b).

The scaling of diffusivity with chain size is consistent with experiment and theory. The diffusivity as obtained from the MSD is in very good agreement with Kirkwood's formula.[50]

$$D_K = \frac{K_B T}{3N^2} \mathrm{Tr} < \sum_{ij} \mu_{ij} > \quad (8)$$

with the expected small overestimation.[51,52] The angle brackets represent averages over *equilibrium* trajectories of the chain and the trace is over the Cartesian indices which are implied by the boldface notation. After validation of the theoretical model, results for active chains are presented next.

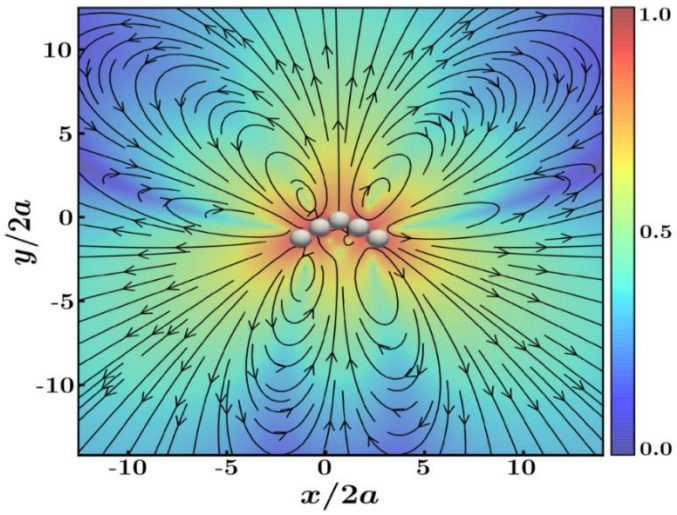

Figure 4-12: Spontaneous fluid flow around an active colloidal chain. In the figure, extensile stresslets, representing the constituent colloids, are oriented along the local tangents of the chain. The background colour is proportional to the logarithm of the magnitude of fluid velocity normalized by its maximum.

Calculation of the diffusivity for a passive chain including hydrodynamic interactions is well-established in the literature of dynamics of polymers in solution. This was first derived by Kirkwood[53] for a linear chain. To the best of our knowledge, there is no equivalent theory for active chains. Therefore, before examining Kirkwood's formula for a linear active chain, the numerical analysis is first benchmarked with control simulations setting the strength of activity $S_0 = 0$. Diffusivity computed from simulations matches well with Kirkwood's formula as demonstrated in (Figure 4-14). These results also agree remarkably well with the experimental data shown in (Figure 4-9).

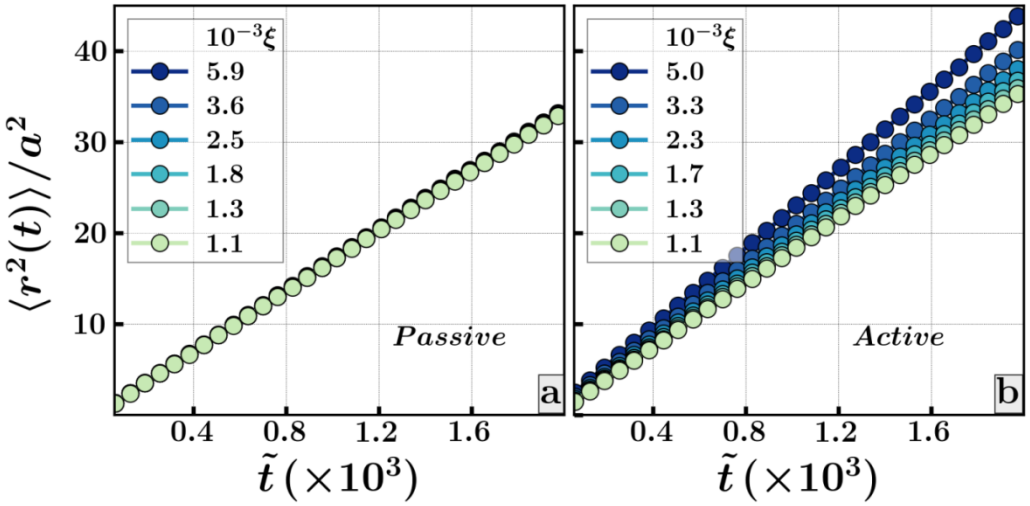

Figure 4-13: Simulation data for MSD of colloidal chains with varying flexibility. Plots on the left represent passive chains while plots on the right represent active chains, N= 5 where $\tilde{t} = \frac{tk_BT\mu_0}{a^2}$ and $\mu_0 = \frac{1}{6\pi\eta a}$.

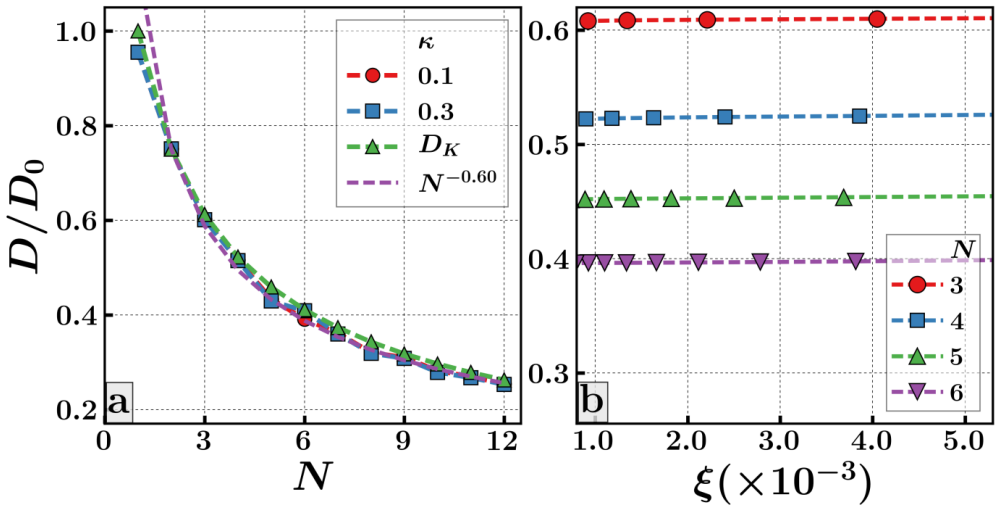

Figure 4-14: Diffusivity of a passive chain. Center of mass diffusivity of the chain, D normalised by the diffusivity of a single monomer, D_0 is displayed in (a) as a function of number of monomers for different bending rigidity. Excellent match of the simulation with Kirkwood's diffusivity D_k validates the numerical analysis. The same quantity is plotted as a function of flexibility for different chain length in (b). It is noted that, as seen in the experiment, the diffusivity does not depend on the flexibility of the chain.

Kirkwood's formula can be extended for active chains by performing the averaging over all non-equilibrium trajectories (Figure 4-15). Noticeably, this extension fails to capture enhanced diffusivity observed both in experiments and in simulations.

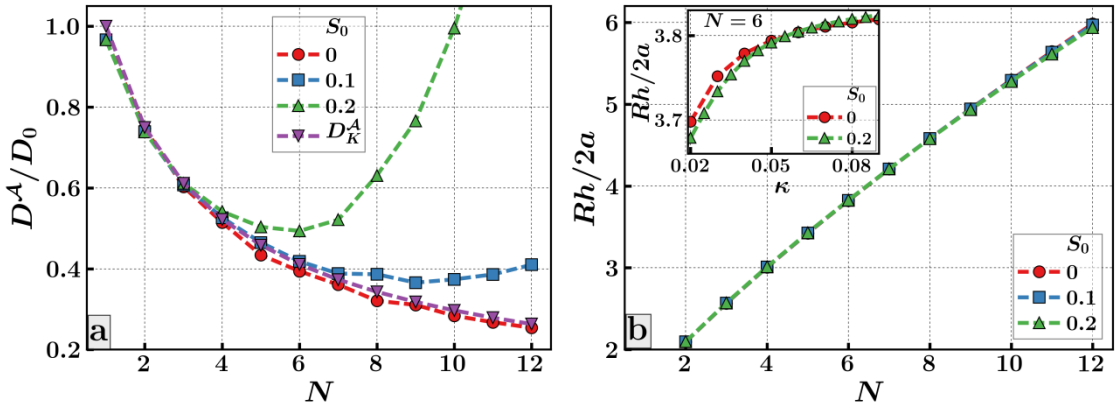

Figure 4-15: Diffusivity of an active chain. Center of mass diffusivity of the active chain is plotted as a function of number of monomers for different activity strength in (a). Clearly, D_K^A, the diffusion constant computed from the modified Kirkwood formula for finite activity, is unable to capture the activity-induced enhancement of diffusion observed in experiments and simulations. In (b) the variation of hydrodynamic radius of the chains as a function of chain length for different levels of activity is shown. The intensity of activity does not lead to a major change in R_h. Our collaborators further display the variation of R_h in the inset of (b) for N=6. For stiffer chains, the chain conformation is predominantly straight. Therefore, the flow extends the chain resulting in a marginal increase in R_h. In contrast, for flexible chains, the non-equilibrium flow draws the beads closer resulting in a marginal decrease in R_h . In these simulations, the value of bending rigidity κ is 0.1.

Next, the effect of flexibility on the diffusivity of a passive chain is presented. The average bond angle between any two consecutive bond vectors (time-averaged over all pairs of consecutive bonds) increases as the flexibility of the chain increases (Figure 4-16a) and becomes obtuse for flexible chains.[54] This increase of the bond angle reduces the hydrodynamic radius (R_h) of the chain. Consequently, a slight enhancement of diffusivity is observed.

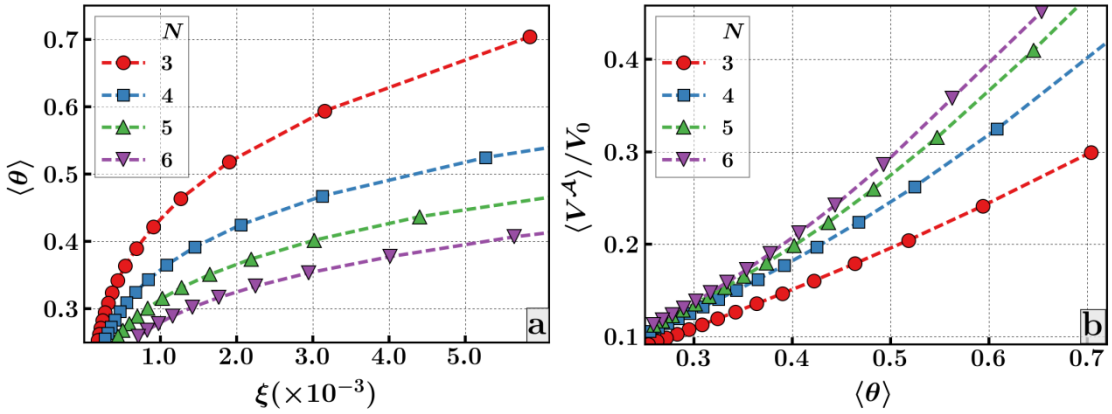

Figure 4-16: Average bond-angle, <θ>, between two consecutive bond vectors increases with the enhancement of chain flexibility for different chain lengths. (b) Center of mass velocity, V^A for active chains of different lengths are plotted as a function of the average bond angle <θ>.

However, this is not the key mechanism for the enhancement of diffusivity of an active chain. Activity contributes to the diffusivity through another mechanism that is not present in the passive chains, nor is considered by Kirkwood. Any non-zero bond angle, due to the Brownian fluctuations creates a local curvature in the chain. This phenomenon breaks the symmetry of the active hydrodynamic flow, results in autonomous motion of the active chain in the direction opposite to the curvature.[35,55] Moreover, the speed of the autonomous movement increases with the increase of the average bond angle (Figure 4-16b). Through this mechanism, the activity enhances the diffusivity of the chain, captured both by experiments (Figure 4-11) and by simulations (Figure 4-17).

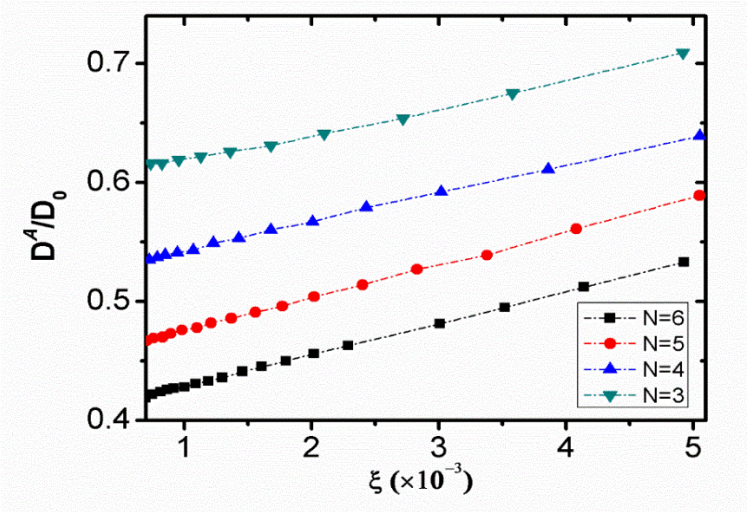

Figure 4-17: Variation of the ratio of diffusivities of active (D^A) normalized by the diffusivity D_0 of a single bead, with flexibility ξ and number of beads N, from Brownian dynamics simulations with active hydrodynamic interactions. The general trend, discernible through the experimental noise and supported by simulation, is that the diffusivity ratio increases with flexibility.

It is not easy to make a direct comparison between the experimental results and simulations since we cannot establish an exact relation between the elasticity in our experimental chain and the elastic Hamiltonian in the simulations. This results in discrepancies between the Kirkwood average and experimental results.[56] However, the trends from the simulation results agree well with those observed in the experiments: the diffusivity increases with flexibility. The most rigid chains $\xi = 1.0\times10^{-3}$ exhibit diffusivities similar to the passive chains. Finally, the enhancement in diffusivity for active chains with higher flexibility ($\xi=5.0\times10^{-3}$) relative to their rigid counterparts is the greatest for the longest chains. To understand the mechanism behind this enhancement, we turn to (Eq. 5). It is clear that the active term breaks detailed balance (Eq. 5) and, therefore, the non-equilibrium stationary state has to be determined from a balance of conservative, dissipative and thermal forces.[35,38-39] To estimate the influence of departure of the chain conformations from equilibrium, the RHS of (Eq. 8) is computed over the non-equilibrium trajectories. The hydrodynamic radius estimated from this non-equilibrium extension of Kirkwood's formula does not differ appreciably from that of passive chains nor does it show a strong dependence on chain flexibility. This is consistent with the estimates of the hydrodynamic radius from experiment (Figure 4-8). The trends observed for the chain diffusivity, then, are clearly not observed in the hydrodynamic radius (and more detailed

comparisons with the Kirkwood formula in Figure 4-15a), which leads us to conclude that active reduction of chain size is not the mechanism underlying the enhanced diffusivity. Rather, the enhanced diffusivity arises primarily due to active hydrodynamic interactions from phoretic flows. For chain lengths much smaller than the persistence length the enhancement of the center of mass diffusion result's from interplay of thermal fluctuations and activity (Figure 4-16). The former generate fluctuations in the chain curvature while the latter drive the chain locally in the direction opposite to this induced curvature. Since the thermal curvature fluctuations are unbiased, the active displacements resulting from such fluctuations are random and, when integrated over several chain relaxation time scales, produce an additional diffusive contribution to the chain motion.

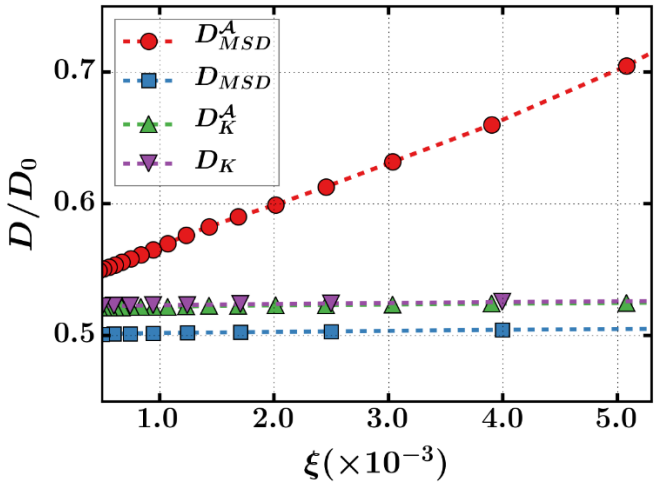

Figure 4-18: Comparison of the diffusivity as obtained from the MSD and from the Kirkwood formula for passive and active chains for N=4. Both these estimates are in very good agreement for passive chains but differ widely for active chains. Activity-induced change of the hydrodynamic radius of the chain cannot account for the enhancement of the diffusivity.

4.6 CONCLUSIONS

In summary, our work demonstrates that large diffusivity enhancements, comparable to those demonstrated for Janus colloids, can be achieved for colloidal systems that are uniformly coated with catalytic nanoparticles. In our work, individual colloids along the chain are chemo-mechanically isotropic. Phoretic flows from catalytic reactions on the surfaces of colloidal monomers result in active hydrodynamic interactions between enchained colloids. Brownian fluctuations in the conformations of the semi-flexible chains break the symmetry of the active fluid flow. The combination of active hydrodynamic flows and Brownian fluctuations results

in an enhancement in chain center-of-mass diffusivity. Thermal forces more readily induce conformational transitions in flexible chains. Therefore, the enhancement in chain diffusivity is larger for more flexible chains. Experimental trends are captured accurately by Brownian microhydrodynamic simulations that incorporate phoretic flows due to activity.

Our results indicate how chain flexibility and activity can be used to tune diffusivity of colloidal objects. Faster than equilibrium dynamics of active chains have implications for their use in drug delivery and mixing. Previously it is demonstrated that the preparation of completely biocompatible ice-templated colloidal aggregates.[57] Biocompatible active colloidal chains powered by enzymatic catalysts[5,28] represent fascinating constructs with potential for directed therapeutic delivery. Hydrodynamically driven active chains grafted on the walls of microfluidic devices could have implications for technologically important problems such as mixing at low Reynolds number. The active colloidal chains presented here are well represented by a mathematical model and therefore, represent an attractive model system for fundamental investigations of active flexible fibers that are ubiquitous motifs in biology, such as bacterial flagellae.

4.7 REFERENCES

1. Fodor, É. *et al.* How Far from Equilibrium Is Active Matter? *Phys. Rev. Lett.* **117**, 038103 (2016).
2. Schliwa, M. & Woehlke, G. Switching on kinesin. *Nature* **411**, 424–425 (2001).
3. Vale, R. D. & Milligan, R. A. The way things move: looking under the hood of molecular motor proteins. *Science* **288**, 88–95 (2000).
4. Sanchez, T., Chen, D. T. N., DeCamp, S. J., Heymann, M. & Dogic, Z. Spontaneous motion in hierarchically assembled active matter. *Nature* **491**, 431–434 (2012).
5. Patra, D., Zhang, H., Sengupta, S. & Sen, A. Dual Stimuli-Responsive, Rechargeable Micropumps *via* "Host–Guest" Interactions. *ACS Nano* **7**, 7674–7679 (2013).
6. Wang, J. & Gao, W. Nano/Microscale Motors: Biomedical Opportunities and Challenges. *ACS Nano* **6**, 5745–5751 (2012).
7. Baraban, L. *et al.* Catalytic Janus Motors on Microfluidic Chip: Deterministic Motion for Targeted Cargo Delivery. *ACS Nano* **6**, 3383–3389 (2012).
8. Ghosh, A. & Fischer, P. Controlled Propulsion of Artificial Magnetic Nanostructured

Propellers. *Nano Lett.* **9**, 2243–2245 (2009).

9. Dey, K. K. *et al.* Micromotors Powered by Enzyme Catalysis. *Nano Lett.* **15**, 8311–8315 (2015).

10. Medina-Sánchez, M., Schwarz, L., Meyer, A. K., Hebenstreit, F. & Schmidt, O. G. Cellular Cargo Delivery: Toward Assisted Fertilization by Sperm-Carrying Micromotors. *Nano Lett.* **16**, 555–561 (2016).

11. Simmchen, J. *et al.* Topographical pathways guide chemical microswimmers. *Nat. Commun.* **7**, 10598 (2016).

12. Palacci, J. *et al.* Light-activated self-propelled colloids. *Philos. Trans. R. Soc. A Math. Phys. Eng. Sci.* **372**, 20130372 (2014).

13. Nitta, T. & Hess, H. Dispersion in Active Transport by Kinesin-Powered Molecular Shuttles. *Nano Lett.* **5**, 1337–1342 (2005).

14. Golestanian, R. Anomalous Diffusion of Symmetric and Asymmetric Active Colloids. *Phys. Rev. Lett.* **102**, 188305 (2009).

15. Zöttl, A. & Stark, H. Hydrodynamics Determines Collective Motion and Phase Behavior of Active Colloids in Quasi-Two-Dimensional Confinement. *Phys. Rev. Lett.* **112**, 118101 (2014).

16. Caspi, A., Granek, R. & Elbaum, M. Enhanced Diffusion in Active Intracellular Transport. *Phys. Rev. Lett.* **85**, 5655–5658 (2000).

17. Polin, M., Tuval, I., Drescher, K., Gollub, J. P. & Goldstein, R. E. Chlamydomonas swims with two "gears" in a eukaryotic version of run-and-tumble locomotion. *Science* **325**, 487–90 (2009).

18. Yeomans, J. M. Playful topology. *Nat. Mater.* **13**, 1004–1005 (2014).

19. Zhang, J. & Granick, S. Natural selection in the colloid world: active chiral spirals. *Faraday Discuss.* **191**, 35–46 (2016).

20. Bricard, A., Caussin, J.-B., Desreumaux, N., Dauchot, O. & Bartolo, D. Emergence of macroscopic directed motion in populations of motile colloids. *Nature* **503**, 95–98 (2013).

21. Yan, J. *et al.* Reconfiguring active particles by electrostatic imbalance. *Nat. Mater.* **15**, 1095–1099 (2016).

22. Snezhko, A. & Aranson, I. S. Magnetic manipulation of self-assembled colloidal asters. *Nat. Mater.* **10**, 698–703 (2011).

23. Dreyfus, R. *et al.* Microscopic artificial swimmers. *Nature* **437**, 862–865 (2005).

24. Stenhammar, J., Wittkowski, R., Marenduzzo, D. & Cates, M. E. Light-induced self-assembly of active rectification devices. *Sci. Adv.* **2**, e1501850 (2016).

25. Howse, J. R. *et al.* Self-Motile Colloidal Particles: From Directed Propulsion to Random Walk. *Phys. Rev. Lett.* **99**, 048102 (2007).

26. Lee, T. C. *et al.* Self-Propelling Nanomotors in the Presence of Strong Brownian Forces. *Nano Lett.* **14**, 2407–2412 (2014).

27. Paxton, W. F. *et al.* Catalytic Nanomotors: Autonomous Movement of Striped Nanorods. *J. Am. Chem. Soc.* **126**, 13424–13431 (2004).

28. Ma, X. *et al.* Enzyme-Powered Hollow Mesoporous Janus Nanomotors. *Nano Lett.* **15**, 7043–7050 (2015).

29. Das, S. *et al.* Boundaries can steer active Janus spheres. *Nat. Commun.* **6**, 8999 (2015).

30. Wang, X., In, M., Blanc, C., Nobili, M. & Stocco, A. Enhanced active motion of Janus colloids at the water surface. *Soft Matter* **11**, 7376–7384 (2015).

31. Ramaswamy, S. The Mechanics and Statistics of Active Matter. *Annu. Rev. Condens. Matter Phys.* **1**, 323–345 (2010).

32. Yan, W. & Brady, J. F. The behavior of active diffusiophoretic suspensions: An accelerated Laplacian dynamics study. *J. Chem. Phys.* **145**, 134902 (2016).

33. Golestanian, R. Collective Behavior of Thermally Active Colloids. *Phys. Rev. Lett.* **108**, 038303 (2012).

34. Wang, W., Duan, W., Ahmed, S., Sen, A. & Mallouk, T. E. From One to Many: Dynamic Assembly and Collective Behavior of Self-Propelled Colloidal Motors. *Acc. Chem. Res.* **48**, 1938–1946 (2015).

35. Jayaraman, G. *et al.* Autonomous Motility of Active Filaments due to Spontaneous Flow-Symmetry Breaking. *Phys. Rev. Lett.* **109**, 158302 (2012).

36. Laskar, A. *et al.* Hydrodynamic instabilities provide a generic route to spontaneous biomimetic oscillations in chemomechanically active filaments. *Sci. Rep.* **3**, 1964 (2013).

37. Laskar, A. & Adhikari, R. Brownian microhydrodynamics of active filaments. *Soft Matter* **11**, 9073–9085 (2015).

38. Manna, R. K., Kumar, P. B. S. & Adhikari, R. Colloidal transport by active filaments. *J. Chem. Phys.* **146**, 024901 (2017).

39. Laskar, A. & Adhikari, R. Filament actuation by an active colloid at low Reynolds number. *New J. Phys.* **19**, 033021 (2017).

40. Ringo, D. L. Flagellar motion and fine structure of the flagellar apparatus in Chlamydomonas. *J. Cell Biol.* **33**, 543–71 (1967).

41. Hilfinger, A., Chattopadhyay, A. K. & Jülicher, F. Nonlinear dynamics of cilia and flagella. *Phys. Rev. E* **79**, 051918 (2009).

42. Higdon, J. J. L. A hydrodynamic analysis of flagellar propulsion. *J. Fluid Mech.* **90**, 685 (1979).

43. Bormuth, V., Varga, V., Howard, J. & Schäffer, E. Protein friction limits diffusive and directed movements of kinesin motors on microtubules. *Science* **325**, 870–3 (2009).

44. Gueron, S., Levit-Gurevich, K., Liron, N. & Blum, J. Energetic considerations of ciliary beating and the advantage of metachronal coordination. *Proc. Natl. Acad. Sci.* **96**, 12240–12245 (1999).

45. Wu, G. W. *et al.* Citrate-Capped Platinum Nanoparticle as a Smart Probe for Ultrasensitive Mercury Sensing. *Anal. Chem.* **86**, 10955–10960 (2014).

46. Majumdar, P., Khan, A. Y. & Bandyopadhyaya, R. Diffusion, adsorption and reaction of glucose in glucose oxidase enzyme immobilized mesoporous silica (SBA-15) particles: Experiments and modeling. *Biochem. Eng. J.* **105**, 489–496 (2016).

47. Zimm, B. H. Dynamics of Polymer Molecules in Dilute Solution: Viscoelasticity, Flow Birefringence and Dielectric Loss. *J. Chem. Phys.* **24**, 269–278 (1956).

48. Petrov, E. P., Ohrt, T., Winkler, R. G. & Schwille, P. Diffusion and Segmental Dynamics of Double-Stranded DNA. *Phys. Rev. Lett.* **97**, 258101 (2006).

49. Jiang, H. R., Yoshinaga, N. & Sano, M. Active Motion of a Janus Particle by Self-Thermophoresis in a Defocused Laser Beam. *Phys. Rev. Lett.* **105**, 268302 (2010).

50. Kirkwood, J. G. & Riseman, J. The Intrinsic Viscosities and Diffusion Constants of Flexible Macromolecules in Solution. *J. Chem. Phys.* **16**, 565–573 (1948).

51. Fixman, M. Inclusion of hydrodynamic interaction in polymer dynamical simulations. *Macromolecules* **14**, 1710–1717 (1981).

52. Liu, B. & Dünweg, B. Translational diffusion of polymer chains with excluded volume and hydrodynamic interactions by Brownian dynamics simulation. *J. Chem. Phys.* **118**, 8061–8072 (2003).

53. Kirkwood, J. G. & Riseman, J. The Intrinsic Viscosities and Diffusion Constants of Flexible Macromolecules in Solution. *J. Chem. Phys.* **16**, 565–573 (1948).

54. Laso, M., Öttinger, H. C. & Suter, U. W. Bond-length and bond-angle distributions in coarse-grained polymer chains. *J. Chem. Phys.* **95**, 2178–2182 (1991).

55. Laskar, A. & Adhikari, R. Brownian microhydrodynamics of active filaments. *Soft Matter* **11**, 9073–9085 (2015).

56. Clisby, N. & Dünweg, B. High-precision estimate of the hydrodynamic radius for self-avoiding walks. *Phys. Rev. E* **94**, 052102 (2016).

57. Rajamanickam, R. *et al.* Soft Colloidal Scaffolds Capable of Elastic Recovery after Large Compressive Strains. *Chem. Mater.* **26**, 5161–5168 (2014).

Chapter-5

Phase Transition of Thermo-responsive Colloidal Chains

5.1 INTRODUCTION

The solution structure of biological as well as synthetic polymers depends on their interactions with the solvents that they are dispersed in.[1–3] In good solvents, there is an effective repulsion between monomers leading to flexible polymers adopting an expanded coil conformation. In poor solvent, structure is determined largely by the effective monomer-monomer attraction. This results in the formation of a dense globule state for flexible polymers. The physics of the coil-globule phase transition has been studied extensively.[4–9] The phase transition of synthetic polymer chains is of great interest due to its implications for biological phenomena such as protein folding, DNA packing, etc. The coil-globule transition is also of fundamental interest. Experimentally, it is extremely challenging to observe the coil-globule transition for single chains. At very dilute concentrations, there is insufficient signal from the polymer chains, while even at relatively modest finite concentrations, polymers tend to phase separate when they collapse into the globular state. Hence, experimental studies of the coil-globule transition remain challenging.

Biopolymers such as proteins and DNA have significant bending rigidity and are classified as semi-flexible polymers. Their collapse transition is mainly driven by the competition between resistance to bending and self-association.[10] The collapse of a semi-flexible polymer might

result in very different equilibrium states and obey different kinetics from that of flexible polymers.[11] Experimental,[12–15] theoretical[16–20] as well as computer simulations[20–24] have studied the collapsed structure of semi-flexible chains. Through all these efforts, researchers have made considerable progress to understand the collapse transition of semi-flexible polymers – however, there still remains much controversy on fundamental topics, such as the type of folding pathways and possible configurations in the diagram of states.

The helical form is ubiquitous in Nature. DNA macromolecules form double-stranded helices and α-helices are routinely observed during folding of proteins into their native state.[25,26] The pervasiveness of helical structures in Nature has been studied using models based largely on geometric concepts[27–30] as well as based on entropy.[31] A mesoscopic continuum theory has been reported that is capable of quantifying the spontaneous assembly of kinked-helices in carbon nanotubes and biological filaments.[32] Rational synthesis of helical nanostructures is also of great interest to materials scientists.[33–36] The assembly of spherical colloids into helical structures with well-controlled handedness has been recently reported.[37] Light controlled self-assembly of semiconductor nanoparticles into helical structures has also been reported.[38]

Here, we present an exciting new model system comprising chains of thermoresponsive colloidal "monomers". The monomers comprise 1 micron sized polystyrene colloids uniformly coated with poly(N-isopropylacrylamide co-allylamine) copolymer micro-gels. These monomers are lined up in an AC electric field and are crosslinked through the amine groups on the microgels to form permanent chains. We demonstrate the preparation of chains with different flexibilities (by varying the time for crosslinking) and show that the chains exhibit reversible collapse transitions on heating. The chain flexibility determines the nature of the collapse transition. Relatively flexible chains exhibit a large increase in the local number density of monomers, while rigid chains show only a modest increase. Chains with intermediate flexibility exhibit the formation of helix-like structures.

5.2 MATERIALS AND METHODS

5.2.1 MATERIALS USED

Polyethylene-glycol di-epoxide (PEG-di-epoxide, supplier specified M_n=500g/mol), allylamine, sodium dodecyl sulfate (SDS) and dialysis bags were obtained from Sigma-Aldrich and were used as received. N-isopropylacrylamide from Acros Organic, N, N′ methylenebisacrylamide (BIS) and potassium peroxydissulphate (KPS) from Merck were used

as received. ITO coated cover slips from Helix Biotech Instruments and indium tin oxide (ITO) coated glass slides from Technistro were used as received.

5.2.2 SYNTHESIS OF PNIPAM MICROGELS

PNIPAM microgels were synthesized by our collaborator, KP Fayis in the group of Dr. Suresh Bhat (CSIR-National Chemical Laboratory). Details are presented here for completeness.

Poly(N-isopropylacrylamide co-allylamine) microgels were prepared via a free radical precipitation polymerization. The polymerization reaction was carried out in a 250 mL three-neck round bottom (RB) flask equipped with a mechanical stirrer, a condenser and an argon inlet. The RB flask was kept in an oil bath throughout the reaction to maintain the reaction temperature at 60^oC. A bottle of deionised water purged with argon gas for 1 h, was used for preparing solutions. In a typical experiment, the purified reactants, monomer N-isopropylacrylamide (1.935g), a cross-linker N,N'- methylene bisacrylamide (BIS) (0.215g, 10% of the total monomer) and surfactant sodium dodecyl sulfate (SDS) (0.03g) were mixed in 115 mL of argon purged deionized water at 40^oC by stirring at 100 rpm for 30 minutes under inert atmosphere. After complete mixing of the reactants, the temperature was increased to 60^oC and co monomer allylamine (0.107g 5% of the total monomer) was added to the mixture. After waiting for thermal equilibration, the initiator KPS (0.025 g in 10 mL of water), was added to the reaction mixture. The reaction mixture changed from transparent to turbid after addition of initiator. The reaction was allowed to proceed for 6 hrs to ensure complete conversion. After 6 hrs, the temperature was reduced to 25^oC and the product (micro-gel) was stirred overnight at 100 rpm. The micro-gel dispersion was purified by dialysis against deionized water for about two weeks to separate unreacted reactants and surfactant from the micro-gel dispersion.

5.2.3 SAMPLE PREPARATION

We dilute 5 µL of PNIPAM micro-gel dispersion (ϕ_{eff}=0.153) in 200 µL of DI water and sonicate for 2 minutes. We dilute 1 µL of PS particle dispersion (containing ~4.8×10^7 PS latex particles) in 200 µL of DI water. Then, we add the dilute PS dispersion to the dilute PNIPAM micro-gel dispersion and sonicate for 5 minutes. The positively charged PNIPAM microgel particles adsorb on the PS particles surfaces through electrostatic complexation. This dispersion was centrifuged at 4000 rpm for 7 minutes and the supernatant was removed to separate unabsorbed PNIPAM microgel particles. Then, we add 150 µL of DI water/glycerol

mixture (volume ratio of water and glycerol is 5:1) to further dilute the dispersion and sonicate for 5 minutes. The density of the fluid is adjusted close to that of the PS latex, viz. ~ 1.05 g/cm^3 We prepare a chamber using parafilm tape on the ITO glass slide (length ~4mm, width ~4m and height ~100µm). We take 20 µL dispersion containing PNIPAM microgel adsorbed PS particles and add 0.5 µL of cross-linker followed by sonication for 2 minutes. This was transferred into the chamber and covered with another ITO coated glass slide on top. We ensure that there is no air bubble trapped in the chamber. We seal this chamber properly so that there is no leakage during chain preparation experiment.

5.2.4 PREPARATION OF LINEAR CHAIN BY AC FIELD

In all experiments, the electric field is imposed using an amplifier (PZD 350 from Trek, USA) and a function generator (AFG1022 from Tektronix) and is monitored using a digital oscilloscope (TSB1102B from Tektronix). We apply AC field (E_{rms}=0.25 V/µm, f = 250 kHz, where E_{rms} is the root mean square of the electric field across the ITO coated glass slides sandwiching the dispersion and f is the frequency. We observe the dispersion using an optical microscope, and observe that all the particles assemble into linear chains along the field direction within 2-3 minutes of imposing the field.[39,40] We keep the electric field on for 12-25 minutes to allow the amine groups on the PNIPAM microgel particles to crosslink and then turn off the field. We observe that this results in the formation of permanent chains dispersed in the solvent. Since the density of the solvent is closely matched with the PS particles, the chains do not settle over long periods of time (2 hrs). We change the crosslinking time to vary the flexibility of the chains. For very rigid chains we allow the crosslinking reaction to proceed for 25 minutes while semi-flexible chains form after crosslinking for 15-20 minutes. Schematic of PNIPAM coated particles with cross-linker and linear chains of particles form on application of an AC electric field in are shown schematically in Figure 5-1.

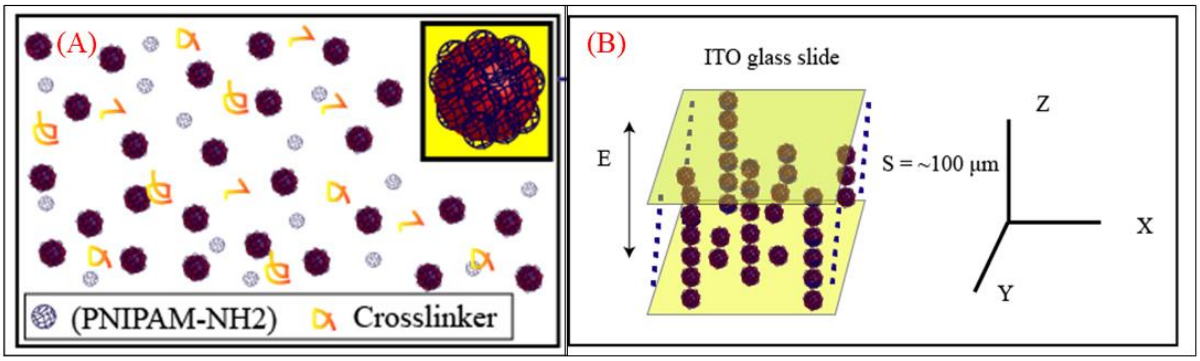

Figure 5-1: (A) schematic of PNIPAM coated particles with cross-linker. (B) Linear chains of particles form on application of an AC electric field.

5.2.5 IMAGING

We use a confocal laser scanning microscope (CLSM) from Carl Zeiss (model-LSM710). For experiments to calculate the temperature dependent pair correlation function of the thermoresponsive (PNIPAM coated PS) "monomeric beads", we use the confocal mode of the microscope with a 63X objective. To estimate the bonding strength between two monomers in a chain of bonded beads, and to estimate the bending rigidity between two bond vectors, we use the optical mode of microscope with a 63X objective. For all other experiments, we use a 20X objective.

5.3 RESULTS AND DISCUSSIONS

The microgel particles were characterized by dynamic light scattering (DLS) at very dilute suspension concentrations (volume fraction $\approx 10^{-3}$) in order to determine the temperature dependence of their size. We assume that the micro gels are sufficiently dilute that there are no two-body interactions at this concentration (including electrostatic interactions). The zeta potential of the micro-gel particles is +42mV. We performed DLS measurements at a fixed scattering angle, $2\theta = 90^{o}$, where 2θ is the scattering angle and is related to the scattering vector $q = 4\pi n \sin\theta/\lambda$, where λ (= 633 nm) is the wavelength of laser light in vacuum and n is the refractive index of the solvent. In Figure 5-2A we have plotted the $g^2(\tau) - 1$ vs time from the DLS data. We analysed the intensity-intensity autocorrelation function using a second-order cumulant method[41] and obtained the hydrodynamic diameter (D_h) using the Stokes-Einstein equation ($D_o = k_B T/3\pi\eta D_h$, where D_o is the diffusivity from DLS, k_B is the Boltzmann constant, T is the temperature of the solvent and η is the viscosity of the solvent). The hydrodynamic

diameter (D_h) of the micro-gel particles decreases with increasing temperature (Figure 5-2B) confirming the thermo-responsive nature of the PNIPAM micro-gels.

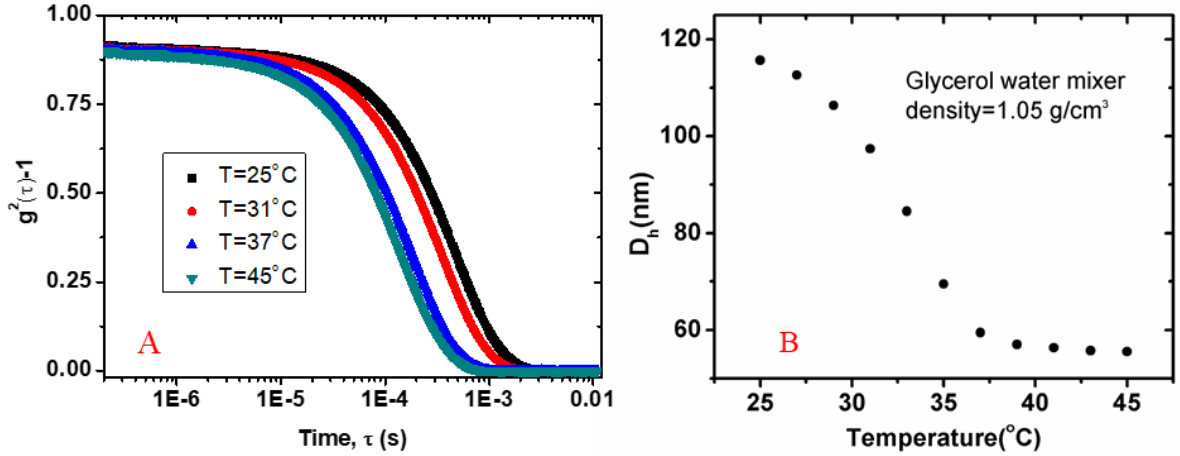

Figure 5-2: (A) $g^2(\tau) - 1$ vs time plot of DLS data. (B)Temperature dependence of the average hydrodynamic diameter (D_h). On heating, the microgel particles exhibit a transition from a swollen state to dehydrated state. Each point represents the equilibrium size of the micro-gel at that temperature. We wait for at least 25 minutes at each temperature for the sample to equilibrate before measuring D_h.

To characterize the temperature dependent behaviour of the PNIPAM coated PS latex, we measure the particle pair correlation function, g(r), using CLSM. Suspensions were kept between a glass slide and a cover slip separated by a spacer of 120 µm thickness. We performed our experiment in bulk suspensions, by focusing at a plane at least 10 µm below the cover slip. We collected a series of images in the x-y plane at different temperatures, after allowing sufficient time for equilibration of the sample (Figure 5-3). We perform experiments in 2D since confocal scanning in the z direction takes a long time during which the colloids diffuse. Thus, confocal scanning microscopy is too slow to allow us to track the motion of 1µm Brownian colloids in 3D. We calculate g(r) in 2D and estimate the equivalent 3D g(r) for the bulk suspension.[42–44] Image processing is carried out using a well-established particle tracking algorithm implemented using Interactive Data Language (IDL).[45] From this analysis, we determine the x-y co-ordinates of the particles and calculate g(r) at different temperatures (Figure 5-4).

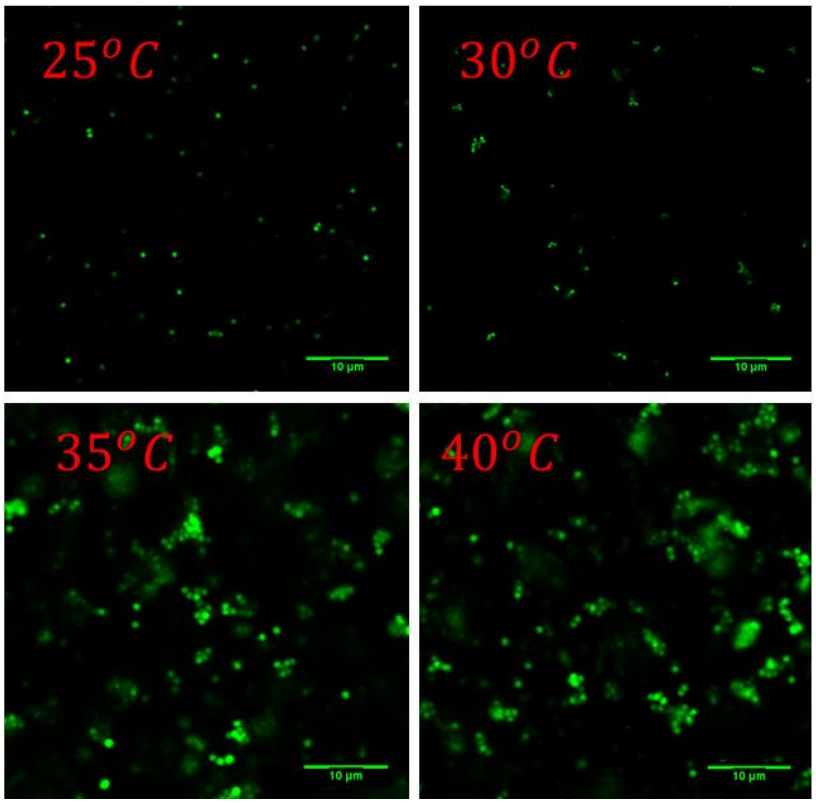

Figure 5-3: Confocal micrographs of PNIPAM coated particles as a function of temperature. At temperatures below the LCST (for example, at 25^oC) particles are well dispersed. As the temperature increases above the LCST, PNIPAM microgels go from a hydrated to dehydrated state and start aggregating. With increase in aggregate size, the Brownian motion gets sluggish – thus, this process results in the formation of multiple small clusters instead of a giant cluster.

We study the range of attraction for the PNIPAM coated PS particles at various temperatures, at a concentration of 4.8×10^8/mL. We measure g(r) at various temperatures and derive the effective potential as –ln[g(r)] (Figure 5-4B). At 25^oC, there is no peak in g(r) and the colloids exhibit hard sphere interactions, viz. repulsive interactions only at contact. At 30^oC and above, we observe a maximum in g(r) at ~ 1.5 µm. The peak in g(r) indicates that the effective interparticle interactions are attractive, viz. U(r) is negative and exhibits a minimum near 1.5 µm. Therefore, the volume phase transition of the PNIPAM microgels that results from a temperature-induced collapse transition on heating results in an effective attractive interaction between the microgel coated PS colloids.

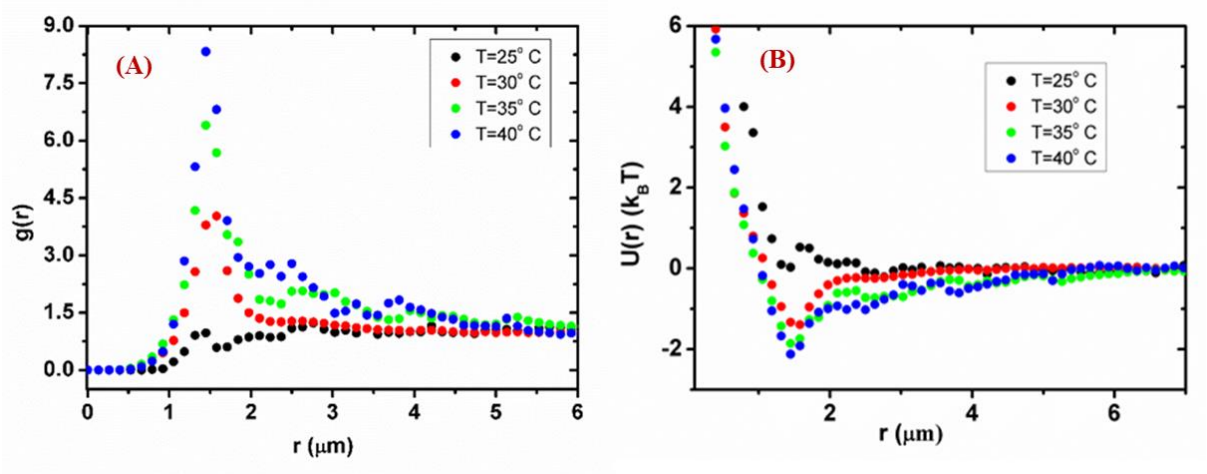

Figure 5-4: (A) Pair correlation g(r) of particles with different temperature. Poly(N-isopropylacrylamide co-allylamine) coated PS particles exhibit attractive interactions at and above 30°C. We estimate the g (r) from a series of images taken at thermal equilibrium at each temperature (over 3500 particles are counted to estimate the pair correlation). (B) It is clearly visible that the height of the g(r) peak increases with temperature. The effective potential derived from g(r) at different temperatures are plotted as a function of distances (r).

We control the flexibility of chain by varying the crosslinking time (see details in Section 5.2.4). We estimate the flexibility as $<(R_N(t) - < R_N >)^2> = L^2\xi^2$, where $R_N(t) = r_N(t) - r_1(t)$ is the end to end distance of the chain at time *t*, and L= (N-1)b is the contour length of the chain (see details in section 4.3.1). We now present the distribution in center to center distance between bonded colloids for chains with different flexibility (Figure 5-5A). We fit this distribution to a Gaussian, $P(r) \sim \exp(-\frac{k(r-r_c)^2}{k_B T})$ and obtain the spring constant, k, that characterizes the bonding between the colloids. As the value of ξ increases from 0.3×10^{-3} to 2.1×10^{-3} to 4.0×10^{-3} we find that k decreases from 114.9 $k_B T(\mu m)^{-2}$ to 76.34 $k_B T(\mu m)^{-2}$ to 56.0 $k_B T(\mu m)^{-2}$ respectively. Next, we obtain bond angle distributions (as indicated in the schematic Figure 5-5B, inset) for chains with different flexibility, ξ. Again, we fit this distribution to a Gaussian form, $P(\theta) \sim \exp(-\frac{\kappa\,\theta^{\,2}}{k_B T})$ and obtain the bending rigidity, κ. As ξ increases from 0.5×10^{-3} to $2.1\times10^{-3}$to 3.4×10^{-2} there is a decrease in bending rigidity (κ) from 9.1×10^{-3} $k_B T(\theta)^{-2}$ to $3.8\times10^{-3} k_B T(\theta)^{-2}$ to 0.8×10^{-3} $k_B T(\theta)^{-2}$.

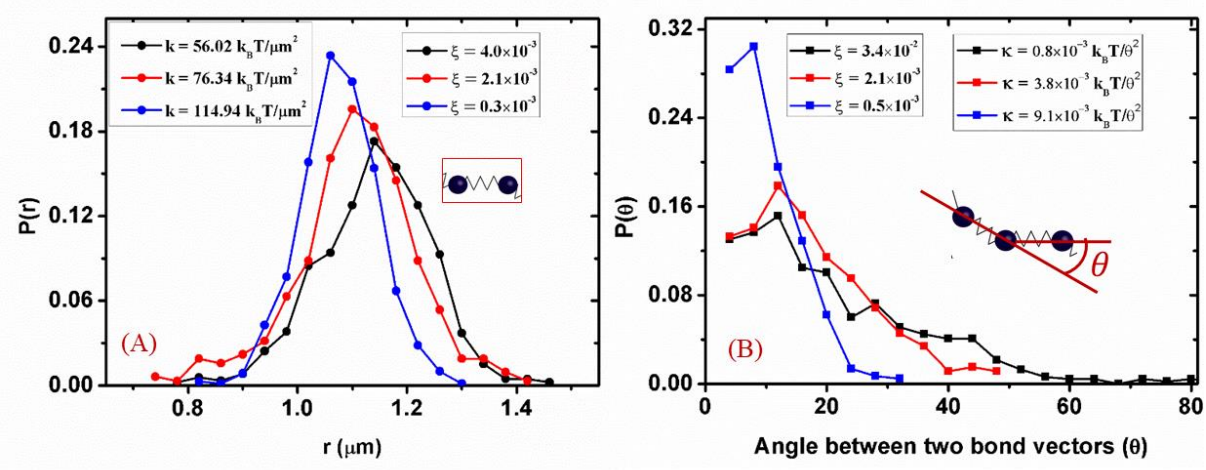

Figure 5-5: (A) Inter-particle distances are narrowly distributed for rigid chain whereas the distribution for relatively flexible chains is wider. (B) Similarly, the distribution of angles between two bond vectors about the mean value is narrow for rigid chains and wider for relatively flexible chains.

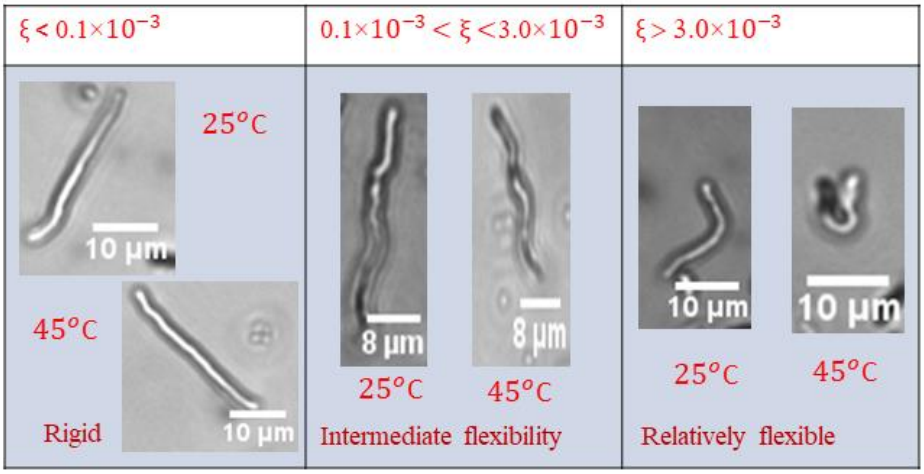

Figure 5-6: Photographs of colloidal chains at 25°C and at 45°C. Temperature dependent transitions of a very rigid chain ($\xi<10^{-4}$, left panel), chain with intermediate flexibility (flexibility parameter in the range of 10^{-4} to 3.0×10^{-3}, middle panel) and relatively flexible chain ($\xi > 3.0\times10^{-3}$, right panel). Chains with intermediate flexibility on heating above 30°C, organize to form structures that appear to be helical. We establish the high temperature structure of these chains later in the Chapter. There is a significant decrease in the chain end-to-end distance for the relatively flexible chains.

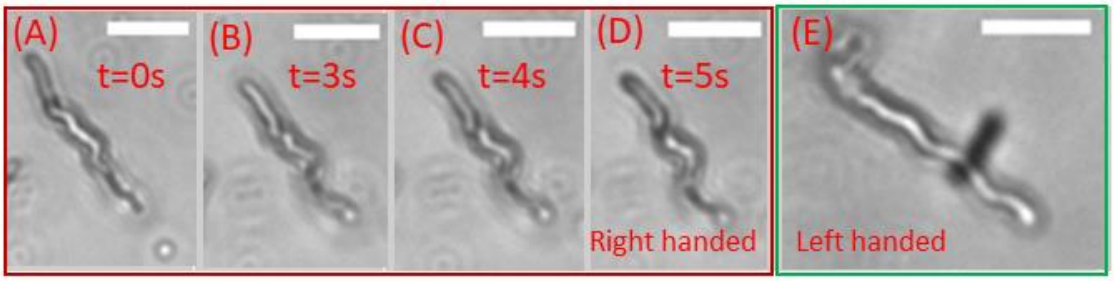

Figure 5-7: Structural change of chain at above $30^{o}C$. (A-D) We define arbitrary time t=0s and presented the structural changes of a chain with intermediate flexibility as time progresses. (D) Appears to be helix-like. Specifically, it is a right handed helix-like structure. (E) We present a left handed helix-like structure as well. All the scale bars are 10 µm.

We characterize the temperature-dependent structure of the linear chains of length ranging from 15 mers to 40 mers, at equilibrium (Figure 5-6 & Figure 5-7). We hold the system isothermal at least for 10 minutes so that the colloidal chain is in thermal equilibrium. We record 2D images at 4 frames per second for more than 7 minutes using the "optical mode" of the CLSM. In this mode, we obtain 2D projections of the chains. At thermal equilibrium, the 2D projections of the chains appear helical in nature. Three dimensional imaging of the structure is necessary to confirm that the structures observed are indeed helical. Therefore, we call these helix-like structures.

For rigid chains, heating does not result in a qualitative transition in the shape of the chain. We observe only a decrease in the chain end to end distance (Figure 5-6, left). For the most flexible chains, we observe the formation of irregular compact configurations (Figure 5-6, right). Of particular interest are the chains of intermediate flexibility ($10^{-4} < \xi < 3.0\times10^{-3}$). On heating, these chains exhibit a decrease in end to end distance and form helix-like structure (Figure 6, middle). This is clearly visible when the chain is observed as a function of time as it forms the helix-like structure. We present a series of images of the formation of helix-like structure as time progresses (Figure 5-7 A to D). We also estimate the handedness of 130 chains in helix-like conformation and observe that about half (55%) are right-handed (Figure 5-7D). To within experimental error, we observe right or left handed helix-like structures with equal probability. The pitch of the helix-like structure varies from 4 to 10 microns. We do not observe any systematic variations of pitch length with temperature.

We measure the end to end distance in 2D, $R^{e} = \sqrt{(x_0 - x_{end})^2 + (y_0 - y_{end})^2}$, where (x_0, y_0) and (x_{end}, y_{end}) are the positions of the end points of the chain in an arbitrary reference

frame. Each data point in Figure 5-8 represents an average over at least 50 different configurations. The error bars are estimated from the standard deviation. We estimate R^e at different temperatures for chains with different flexibility. We plot R^e normalized by the average end to end distance at 25^oC ($R^e_{25^oC}$) in Figure 5-8A and observe that, above 30^oC there is a decrease in the chain size. The end to end distance, R^e is a function of temperature (T) and flexibility (ξ) of the chains. Rigid chains ($\xi < 10^{-5}$) show a relatively small reduction in R^e above 40^oC relative to flexible chains ($\xi > 3.0 \times 10^{-5}$). We observe that flexible chains exhibit over 60% reduction in R^e on heating (Figure 5-8A). We estimate the number density of monomers locally, within the coil of the colloidal chain as $\rho = N/R^{e3}$. We plot ρ as a function of the temperature in Figure 5-8B. Since R^e for relatively flexible chains decreases significantly, there is a rapid increase in the local monomer density on heating. In contrast, there is only a modest increase in ρ for rigid chains when they collapse on heating (Figure 5-8B).

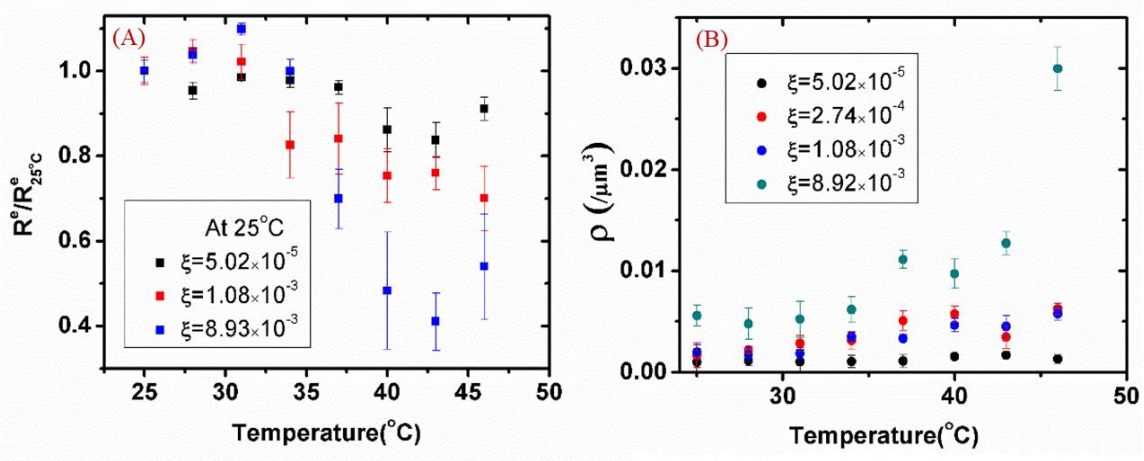

Figure 5-8: (A) Variation of end to end distances of chain (normalized with the average end to end distance at 25^oC) with temperature. (B) Variation of density ($\rho = N/R^{e3}$) of particles with temperature for different flexible chain. It is seen that there is a drastic increase in ρ for flexible chains at above 35^oC, whereas there is almost no change in monomer density (ρ) for the most rigid chains.

It is well known that the conformation of polymer chains depends on the quality of the solvents.[1–3] Flexible polymers in a good solvent exhibit swollen-coil conformations since individual monomers effectively repel each other and the monomers are preferentially surrounded by solvent molecules. On the other hand, flexible polymers in poor solvent expel solvent molecules such that there is effective monomer-monomer attraction. Thus, in poor solvent, a compact globule structure is formed, that minimizes contact between solvent and

monomers. The coil-globule transition of flexible polymers is a classical problem in polymer physics and has been well studied in the literature.[7,46,47] Collapse of semi-flexible polymers in poor solvents has also been reported.[8] In case of linear colloidal assemblies, Vutukuri et al. demonstrated that semi-flexible charged chains adopt a straight configuration by changing the long range electrostatic interaction between monomers.[39] We experimentally demonstrate the effect of solvent quality of thermo-responsive "polymeric" colloidal chains. We systematically vary the flexibility of the colloidal chain to prepare rigid and semi-flexible systems, and visualize the temperature-dependent change of their R^e and ρ under microscopy (Figure 5-8B). We have shown that, while going form good solvent to poor solvent by increasing temperature, there is a ~10% decrease in the normalized R^e for rigid chains whereas relatively flexible chains exhibit up to 60% decrease in size. This transition is reversible since the chains re-swell on cooling. We reiterate that we hold the samples isothermal for over 10 minutes before making a measurement. Under these conditions, we do not observe any hysteresis in the change in chain size during a heat/cool cycle. The local number density of monomers (ρ) in a chain varies with changing solvent quality since there is a change in size (R^e). For relatively flexible chains, we observe a dramatic change in ρ on heating above 35^oC.

We now focus on the helix-like structure that forms in chains of intermediate flexibility on heating. Video observation of the structure formation of these chain held isothermal at temperatures above 30^oC indicate that the structure varies with time (Figure 5-7). Helix-like structures that form over a part of a chain unravel with time, while other parts of the chain subsequently fold to form a helix-like structure. Thus, the formation of helix-like structures in the chains is a dynamic process. We analyse 2D images frame by frame and estimate fraction of total the chain length are organized into helix-like structures. We only analyse images where the chains are horizontal, and in the focal plane of the objective. We use Matlab to extract the image intensity along the chain and observe that chains that we have determined to be helix-like structure (from video analysis) exhibit periodic intensity variations along their length. These arise from parts of the chain going out of focus as parts of the structure go out of the focal plane. It is possible that chains that have sinusoidal conformations and that are not helix-like structure would also exhibit such periodic intensity variations – however, we do not see any evidence for the formation of such conformations in our experiments. We arbitrarily define a chain segment to be helix-like if it exhibits at least one cycle of high/low/high or low/high/low intensity variation.

Chain with flexibility parameter in the range of 0.1×10^{-3} to 3.0×10^{-3} organize into helix-like structures on heating. The degree of chain helicity is a function of temperature. At 25°C, when the chains are well solvated, they do not organize into helix-like structures. We hold the system isothermal at different temperatures and record images of the chain at intervals of 0.25 s. We analyse this series of images to obtain the time dependent fraction of the chain that forms helix-like structures. At any particular temperature, we average over more than 2500 monomers to estimate the fraction of monomers that participate in helix-like structure. At 35°C ~ 20% monomers are organized into a helix-like structures and this increases to ~35% at a temperature of 45°C. At 50°C & 55°C, we observe that ~ 30% of the monomers organize into helix-like structure (Figure 5-9A), a slight decrease from the maximum. The fraction of monomers participating to form helix-like structure in an image varies from 0 to 1, so instead of finding the standard error, we present the distribution of fraction of images (time average) as a function of fraction of monomers forming helix-like structure (Figure 5-9B), at different temperatures. At 35°C, ~60% of the images do not contain chains with a helix-like structure, and at 45°C, this fraction reduces to ~50%. At lower temperature, below 25°C, we observe no helix-like structure formation at any time.

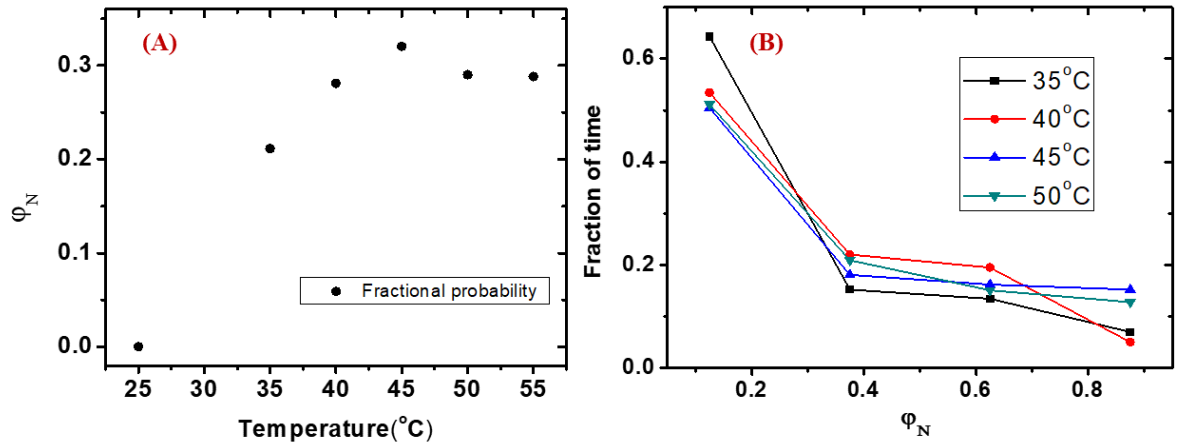

Figure 5-9: (A) φ_N represents the fraction of monomers that participate in helix-like conformations. Here, we consider only those chains where ξ is between 0.1×10^{-3} to 3.0×10^{-3}. φ_N increases from 0 (at $25^o C$) to ~ 0.35 with increasing temperature. (B) The fraction of monomers participating to form helix-like structure in an image varies from 0 to 1. We present the distribution of chains forming helix-like structures, at different temperatures.

In our experiment the colloidal chains are rendered thermo-responsive due to the presence of PNIPAM micro-gel particles on their surface. Therefore, they are well solvated at low

temperature, below 25°C and collapse on heating to temperatures above 30°C. The structural changes of the chains in poor solvent are a function of their flexibility. For chains that are rigid, there is no qualitative change in conformation on heating. Thus, the attractive monomer-monomer potential that develops on heating is insufficient to overcome the chain rigidity and change the conformation (or local monomer number density) drastically (Figure 5-6, left column). For chains with intermediate flexibility (ξ from 0.1×10^{-3} to 3.0×10^{-3}), heating results in the development of helix-like structure above $30^{o}\mathrm{C}$. Helix-like structures are observed to form only when the chain flexibility is within this range. Only in this range does the competition between bending rigidity and monomer-monomer attractive force lead to formation of helix-like structures. Helices are a common motif for compact structures in biological filaments, carbon nanotubes or other string like objects.[28,31,32] Above $45^{o}\mathrm{C}$, the hydrodynamic diameter (D_h**)** of the micro-gel does not change (Figure 5-2) since it is completely dehydrated. Thus, there is no further increase in the effective attractive potential (U(r)) above $45^{o}\mathrm{C}$. Therefore, the fraction of monomers that participate in helix-like structure formation remains almost constant above $45^{o}\mathrm{C}$.

5.4 CONCLUSIONS

We present temperature dependent transitions in the structure of thermo-responsive colloidal chains. Poly(N-isopropylacrylamide co-allylamine) micro-gel coated PS colloids are enchained to form linear chains of thermo-responsive monomers. Above the LCST of PNIPAM, these chains behave like they are in a bad solvent and exhibit strong monomer-monomer attractive interactions. There is a decrease in the size of the chains, as measured by the end-to-end distance. Rigid chains show a modest decrease in size but exhibit no qualitative change in their shape. Relatively flexible chains form compact structures as they collapse, resulting a large increase in the local monomer number density within the chain. Chains with intermediate flexibility show the formation of helix-like structures on heating. We propose that this arises from a balance between the bending rigidity of the chain and attractive interactions between monomers along the chain.

5.5 REFERENCES

1. Fredrickson, G. H. *The theory of polymer dynamics*. *Current Opinion in Solid State and Materials Science* (Clarendon Press, 1996).

2. de Gennes, P. G. *Scaling Concepts in Polymer Physics*.(Cornell university press, 1980).

3. Michael Rubinstein & Ralph H. Colby. *Polymer Physics*. (Oxford Uiversity Press, 2003).

4. Yu, J., Wang, Z. & Chu, B. Kinetic study of coil-to-globule transition. *Macromolecules* **25**, 1618–1620 (1992).

5. Dawson, K. A., Timoshenko, E. G. & Kuznetsov, Y. A. Kinetics of conformational transitions of a single polymer chain. *Phys. A Stat. Mech. its Appl.* **236**, 58–74 (1997).

6. de Gennes, P. G. Kinetics of collapse for a flexible coil. *J. Phys. Lettres* **46**, 639–642 (1985).

7. Halperin, A. & Goldbart, P. M. Early stages of homopolymer collapse. *Phys. Rev. E* **61**, 565–573 (2000).

8. Montesi, A., Pasquali, M. & MacKintosh, F. C. Collapse of a semiflexible polymer in poor solvent. *Phys. Rev. E* **69**, 021916 (2004).

9. Chang, R. & Yethiraj, A. Solvent effects on the collapse dynamics of polymers. *J. Chem. Phys.* **114**, 7688–7699 (2001).

10. Wu, J., Cheng, C., Liu, G., Zhang, P. & Chen, T. The folding pathways and thermodynamics of semiflexible polymers. *J. Chem. Phys.* **148**, 184901 (2018).

11. Go, N. *Theoritical studies of protein folding*. *Ann. Rev. Biophys. Bioeng.1983* **12**, (1983).

12. Bloomfield, V. A. DNA condensation. *Curr. Opin. Struct. Biol.* **6**, 334–341 (1996).

13. Yoshikawa, K. & Matsuzawa, Y. Nucleation and growth in single DNA molecules. *J. Am. Chem. Soc.* **118**, 929–930 (1996).

14. Maurstad, G. & Stokke, B. T. Toroids of stiff polyelectrolytes. *Curr. Opin. Colloid Interface Sci.* **10**, 16–21 (2005).

15. Vilfan, I. D., Conwell, C. C., Sarkar, T. & Hud, N. V. Time study of DNA condensate morphology: Implications regarding the nucleation, growth, and equilibrium populations of toroids and rods. *Biochemistry* **45**, 8174–8183 (2006).

16. Post, C. B. & Zimm, B. H undefined. Theory of DNA condensation: collapse versus aggregation. *Biopolymers: Original Research on Biomolecules. **21***, 2123-2137(1982).

17. Stukan, M. R., Ivanov, V. A., Grosberg, A. Y., Paul, W. & Binder, K. Chain length dependence of the state diagram of a single stiff-chain macromolecule: Theory and Monte Carlo simulation. *J. Chem. Phys.* **118**, 3392–3400 (2003).

18. Cooke, I. R. & Williams, D. R. M. Condensed states of a semiflexible homopolymer: Ordered globules and toroids. *Phys. A Stat. Mech. its Appl.* **339**, 45–52 (2004).

19. Yoshinaga, N. Folding and unfolding kinetics of a single semiflexible polymer. *Phys. Rev. E* **77**, 061805 (2008).

20. Zhang, X., Bao, L., Wu, Y. Y., Zhu, X. L. & Tan, Z. J. Radial distribution function of semiflexible oligomers with stretching flexibility. *J. Chem. Phys.* **147**, 054901 (2017).

21. Lappala, A. & Terentjev, E. M. Maximum compaction density of folded semiflexible polymers. *Macromolecules* **46**, 7125–7131 (2013).

22. Kong, M., Saha Dalal, I., Li, G. & Larson, R. G. Systematic coarse-graining of the dynamics of self-attractive semiflexible polymers. *Macromolecules* **47**, 1494–1502 (2014).

23. Marenz, M. & Janke, W. Knots as a Topological Order Parameter for Semiflexible Polymers. *Phys. Rev. Lett.* **116**, 128301 (2016).

24. Seaton, D. T., Schnabel, S., Landau, D. P. & Bachmann, M. From flexible to stiff: Systematic analysis of structural phases for single semiflexible polymers. *Phys. Rev. Lett.* **110**, (2013).

25. Denton, M. & Marshall, C. Laws of form revisited. *Nature* **410**, 417–417 (2001).

26. Chothia, C. & Finkelstein, A. V. The Classification and Origins of Protein Folding Patterns. *Annu. Rev. Biochem.* **59**, 1007–1035 (1990).

27. Maritan, A., Micheletti, C., Trovato, A. & Banavar, J. R. Optimal shapes of compact strings. *Nature* **406**, 287–290 (2000).

28. Poletto, C., Giacometti, A., Trovato, A., Banavar, J. R. & Maritan, A. Emergence of secondary motifs in tubelike polymers in a solvent. *Phys. Rev. E* **77**, 061804 (2008).

29. Lewis, P. N., Momany, F. A. & Scheraga, H. A. Folding of Polypeptide Chains in Proteins : A Proposed Mechanism for Folding Chemistry : *Proc. Natl. Acad. Sci.***68**,

2293–2297 (1971).

30. Banavar, J. R. & Maritan, A. *Colloquium* : Geometrical approach to protein folding: a tube picture. *Rev. Mod. Phys.* **75**, 23–34 (2003).

31. Snir, Y. & Kamien, R. D. Entropically driven helix formation. *Science* **307**, 1067 (2005).

32. Cohen, A. E. & Mahadevan, L. Kinks, rings, and rackets in filamentous structures. *Proc. Natl. Acad. Sci.* **100**, 12141–6 (2003).

33. Iijima, S. Helical microtubules of graphitic carbon. *Nature* **354**, 56–58 (1991).

34. Yang, S. M., Sokolov, I., Coombs, N., Kresge, C. T. & Ozin, G. A. Formation of Hollow Helicoids in Mesoporous Silica: Supramolecular Origami. *Adv. Mater.* **11**, 1427–1431 (1999).

35. Yang, S. *et al.* On the Origin of Helical Mesostructures. *J. Am. Chem. Soc.* **32**, 10460-10466. (2006).

36. Wu, Y. *et al.* Composite mesostructures by nano-confinement. *Nat. Mater.* **3**, 816–822 (2004).

37. Yin, Y. & Xia, Y. Self-assembly of spherical colloids into helical chains with well-controlled handedness. *J. Am. Chem. Soc.* **125**, 2048–2049 (2003).

38. Srivastava, S. *et al.* Light-controlled self-assembly of semiconductor nanoparticles into twisted ribbons. *Science* **327**, 1355–9 (2010).

39. Vutukuri, H. R. *et al.* Colloidal Analogues of Charged and Uncharged Polymer Chains with Tunable Stiffness. *Angew. Chemie Int. Ed.* **51**, 11249–11253 (2012).

40. Yethiraj, A. Tunable colloids: control of colloidal phase transitions with tunable interactions. *Soft Matter* **3**, 1099 (2007).

41. Frisken, B. J. Revisiting the method of cumulants for the analysis of dynamic light-scattering data. *Appl. Opt.* **40**, 4087- 4091 (2001).

42. Paloli, D., Mohanty, P. S., Crassous, J. J., Zaccarelli, E. & Schurtenberger, P. Fluid–solid transitions in soft-repulsive colloids. *Soft Matter* **9**, 3000- 3004 (2013).

43. Royall, C. P., Louis, A. A. & Tanaka, H. Measuring colloidal interactions with confocal microscopy. *Macromol. J. Chem. Phys.* **127**, 044507 (2007).

44. Campbell, A. I., Anderson, V. J., Van Duijneveldt, J. S. & Bartlett, P. Dynamical arrest in attractive colloids: The effect of long-range repulsion. *Phys. Rev. Lett.* **94**, 1–4 (2005).

45. Crocker, J. C. & Grier, D. G. Methods of Digital Video Microscopy for Colloidal Studies. *J. Colloid Interface Sci.* **179**, 298–310 (1996).

46. Lettres, P. D. G.-J. de P. & 1985, U. Kinetics of collapse for a flexible coil. *Journal de Physique Lettres* **46**, 639-642 (1985).

47. Ostrovsky, B. & Bar-Yam, Y. Irreversible Polymer Collapse in 2 and 3 Dimensions. *Europhys. Lett.* **25**, 409–414 (1994).

Chapter-6

Summary and Future Scope

In the preceding Chapters, we have described the preparation of colloidal assemblies, with a focus on assembling colloids into linear chains. We have examined the structure of such chains, their dynamics and phase transitions. We have described ice templating of dilute colloidal dispersions as a novel technique to assemble colloids. Freezing the dispersion in isotropic and directional fashion have been examined and the distribution of colloidal assemblies formed through the ice-templating is characterized in great detail. We have also prepared colloidal chains by crosslinking coated colloids, organized in an AC electric field. A novel aspect of this work is to render the colloidal chains active, viz. out of equilibrium, by adsorbing catalytic platinum nanoparticles on their surface and by conducting reactions catalysed by the nanoparticles. Another novel aspect is to render the colloidal chains thermo-responsive by adhering poly N-isopropyl acrylamide microgel particles on the colloidal surface. Here, we briefly summarize the key advances reported in this thesis.

6.1 COLLOIDAL ASSEMBLY:

- We have investigated isotropic and directional ice templating of dilute aqueous dispersions of polymer coated colloids and cross-linker, at concentrations far below that required to form percolated monoliths. Freezing the aqueous dispersions forces particles into close

proximity to form clusters. These assemblies are held together when the polymer that coats the particles is crosslinked. We observe that, with increase in particle concentration from about 10^6 to 10^9 particles/ml, there is a transition from isolated single particles to increasingly larger clusters.

- We have also prepared linear chains of colloidal particles by assembling polymer coated particles by applying an AC field. The combination of long-range charge repulsion and dipolar interactions induced by the external AC field assembles particles into linear chains. We allow the colloidal monomers that line up to bond by crosslinking polymer microgels adsorbed on the particle surfaces. Thus, particles remain enchained even after removing the external field. We control the flexibility of the colloidal chain by varying the field strength and time allowed for cross-linking.

6.2 KEY RESULTS

- During ice templation, exclusion of colloidal particles by the growing freezing front leads to particle accumulation at ice crystal boundaries. There are three types of assembled structures that were formed for both the isotropic and directional ice templating: linear chains, two particle-wide tapes and extended sheets. There was also a small fraction of three dimensional structures at the highest dispersion concentrations investigated. Remarkably, the fractional probability for formation of a cluster of n particles, P_n ($n > 2$, up to n ~ 30 particles) scales as n^{-2}, independent of particle concentration for isotropic ice templating (over a 100-fold variation in concentration 10^6 to 10^8 /mL). In contrast to the isotropic freezing experiments, for directional freezing, P_n strongly depends on the concentration of particles. The distribution function (P_n) obeys a power law $P_n \sim n^{-\eta}$, where η varies from 2.27 (for particle concentration $\sim 10^9$ particles/mL) to 3.19 (for 10^7 particles/mL).
- We calculated the spring constant (k) that characterizes particle-particle bonding in chains of colloids, from the center to center distance distribution between two neighbouring bonded particles. Similarly, the bending rigidity (κ) was calculated from the bond angle distribution. We define the chain flexibility (ξ) as $\langle (R_N(t) - R_N)^2 \rangle = L^2\xi^2$, where $R_N(t) = r_N(t) - r_1(t)$ and L= (N-1)b, where b is the size of monomer and N is the number of monomers in the linear chain. With increasing crosslinking time, the chain flexibility decreases, and this is observed to correlate with an increase in k and κ.

- Centre of mass diffusion of passive colloidal chains scales in the manner of Zimm's treatment ($D_N \sim N^{-0.58}$), consistent with Gaussian fluctuations exhibited by semi-flexible linear assemblies. The diffusion coefficient of passive Brownian chains does not depend on the chain flexibility.
- Colloidal chains where the monomers are uniformly coated with platinum nanoparticles show active dynamics in the presence of peroxide. The catalytic platinum nanoparticles decompose peroxide to induce phoretic flows. Activity arises from hydrodynamic interactions between enchained colloidal beads due to these flows. This resulted in diffusivity enhancements of up to 60% for individual chains in dilute solution. Chains with increasing flexibility exhibited higher diffusivities. The enhancement in diffusivity can be attributed to the interplay between chain conformational fluctuations and activity.
- Grafting thermo-responsive PNIPAM micro-gel nanoparticles on the surface of micron-sized colloidal particles allow us to create thermo-responsive colloidal polymeric chains. Above the LCST of PNIPAM, these chains behave like they are in a bad solvent and exhibit strong monomer-monomer attractive interactions. There is a decrease in the size of the chains, as measured by the end-to-end distance. Rigid chains show a modest decrease in size but exhibit no qualitative change in their shape. Relatively flexible chains form compact structures as they collapse, resulting a large increase in the local monomer number density within the chain. Chains with intermediate flexibility show the formation of helix-like structures on collapse.

6.3 FUTURE SCOPE

In this thesis, we have established a colloidal model system for polymers. We have studied their dynamics and investigated the phase transition of thermos-responsive colloidal chains in detail. Having established a route to this exciting new model system for flexibly connected colloids, we list a few problems that could be addressed using these colloidal chains.

- Colloidal particles suspended in a bath of bacteria represent passive particles in an active bath. This situation, when colloids are suspended in an active bath,[2,3] is rather different from equilibrium Brownian motion.[1] The dynamics of colloidal beads in a bath of swimming E.coli bacteria has been investigated experimentally and numerically.[4] The dynamics are quite interesting for non-spherical colloids. In case of a polymer in active bath, numerically and theoretically it has been shown that the diffusion is faster and the

polymers undergoes swelling.[5–7] However, there is no experimental realization of this to date. Microscopic experiments using our colloidal polymeric chains in an active bath will afford detailed investigation of this phenomenon. By systematically varying the flexibility of the colloidal polymers, their dynamics and conformation changes in an active bath can be investigated. We believe that this model system has the potential to provide deep understanding of the nature of polymers in an active bath.

- Diffusion over a periodic or complex energy landscape is a common problem that appears in many fields of physics. For instance, under thermal agitation, the motion of atoms adsorbed on crystal surfaces is determined by the interactions of electrons with the substrate atoms. The connection between surface diffusion and interaction potential is extremely important for understanding the crystal growth and surface migration.[8,9] The diffusion of spherical colloidal particles over a periodic energy landscape is already reported.[10] The diffusion of connected colloidal polymers over a periodic or complex energy landscape is yet to be investigated.

- Our system allows control over monomer-monomer interactions in thermo-responsive colloidal chains. The interaction between monomers of a thermo-responsive colloidal polymer and a periodic energy landscape can be controlled by adsorbing PNIPAM on the patterned surface. We anticipate that at lower temperatures, thermo-responsive polymers will experience a repulsive interaction with the surfaces and diffuse over them. At higher temperatures, monomers will experience strong attractive interaction with the surface. Adsorption of thermo-responsive colloidal chains on patterned surfaces might provide insights into secondary crystallization of molecular polymers.

- Ordered assembly of micron size particles at air–water interface to form a lattice-like structure has been demonstrated.[11] The motion of the trapped particles at the air-water interface are purely two-dimensional.[11] Sometimes, particles at interfaces are also observed to form loosely bounded crystalline structures.[12] In these, perturbing the lattice-like monolayer results in the formation of fractal aggregates.[12] We believe that the model thermo-responsive particles developed in this work have potential to help understand the aggregation process at the air-water interface. In these systems, we can precisely control

the attractive interaction between monomers by simply changing the temperature. This interaction is reversible, allowing us to repeat the experiment with the same system.

- Network gels are encountered in everyday life, such as the edible dessert, Jello. Gelation often results from the formation of crosslinks between polymer chains. These crosslinks are induced either by micro-crystallization (upon cooling) or by covalent bond formation.[13] Using video microscopic technique, gelation or network formation in colloidal chains can be studied. Here, systematic variation of the colloidal chain flexibility and control of the interaction between particles provide interesting experimental levers.

One should not consider colloidal chains only as colloidal analogues for molecular polymers. We contend that such colloidal chains are a form of matter in their own right with complex and interesting collective behavior that might not be observed for molecular polymeric molecules.

6.4 REFERENCES

1. Mazenko, G. F. *Nonequilibrium Statistical Mechanics*. *Nonequilibrium Statistical Mechanics* (Oxford University Press, 2008).

2. Argun, A. *et al.* Non-Boltzmann stationary distributions and non-equilibrium relations in active baths. *Phys. Rev. E* **94**, 062150 (2016).

3. Krishnamurthy, S., Ghosh, S., Chatterji, D., Ganapathy, R. & Sood, A. K. A micrometre-sized heat engine operating between bacterial reservoirs. *Nat. Phys.* **12**, 1134–1138 (2016).

4. Maggi, C. *et al.* Generalized energy equipartition in harmonic oscillators driven by active baths. *Phys. Rev. Lett.* **113**, 238303 (2014).

5. Harder, J., Valeriani, C. & Cacciuto, A. Activity-induced collapse and reexpansion of rigid polymers. *Phys. Rev. E* **90**, 062312 (2014).

6. Vandebroek, H. & Vanderzande, C. Dynamics of a polymer in an active and viscoelastic bath. *Phys. Rev. E* **92**, 060601 (2015).

7. Eisenstecken, T., Gompper, G. & Winkler, R. G. Internal dynamics of semiflexible polymers with active noise. *J. Chem. Phys.* **146**, 154903 (2017).

8. Ayrault, G. & Ehrlich, G. Surface self-diffusion on an fee crystal: An atomic view. *J. Chem. Phys.* **60**, 281–294 (1974).

9. Zhang, Z. & Lagally, M. G. Atomistic processes in the early stages of thin-film growth. *Science.* **276**, 377–383 (1997).

10. Ma, X. G., Lai, P. Y. & Tong, P. Colloidal diffusion over a periodic energy landscape. *Soft Matter* **9**, 8826–8836 (2013).

11. Pieranski, P. Two-dimensional interfacial colloidal crystals. *Phys. Rev. Lett.* **45**, 569–572 (1980).

12. Ghezzi, F., Earnshaw, J. C., Finnis, M. & McCluney, M. Pattern formation in colloidal monolayers at the air-water interface. *J. Colloid Interface Sci.* **238**, 433–446 (2001).

13. de Gennes, P. G. *Scaling Concepts in Polymer Physics*. (Cornell University Press, 1980).

List of Publications

1. Guruswamy Kumaraswamy, **Bipul Biswas**, and Chandan Kumar Choudhury. "Colloidal assembly by ice templating." ***Faraday Discuss.*** **186 (2016): 61-76** ***(Selected as Cover page).***
2. **Bipul Biswas**, Mayank Misra, Anil Singh Bisht, Sanat K. Kumar and Guruswamy Kumaraswamy. "Assembly of colloids by directional ice templating: Their size distribution" ***(Manuscript in preparation).***
3. **Bipul Biswas,** Raj Kumar Manna, Abhrajit Laskar, PB Sunil Kumar, Ronojoy Adhikari, and Guruswamy Kumaraswamy. "Linking Catalyst-Coated Isotropic Colloids into "Active" Flexible Chains Enhances Their Diffusivity." ***ACS Nano*** **11(2017): 10025-10031**
4. **Bipul Biswas**, Fayis KP, SK Bhat, Apratim Chatterji, and Guruswamy Kumaraswamy "Temperature driven phase transition of thermo-responsive colloidal chains." (***Manuscript in preparation***).
5. Saurabh Usgaonkar, Subrajeet Deshmukh, **Bipul Biswas**, Neeta Karjule, Prashant Yadav, Jayaraj Nithyanandhan, and Guruswamy Kumaraswamy. "Light-Triggered, Spatially Localized Chemistry by Photoinduced Electron Transfer." ***Angewandte Chemie International Edition*** **(2019): 2715-2719**
6. Farsa Ram, **Bipul Biswas**, Arun Torris, Guruswamy Kumaraswamy and Kadhiravan Shanmuganatha "Highly Compressible and Anisotropic Piezoelectric Energy Harvesters based on Cellulose Nanocrystals" (***Manuscript in preparation***).